

AHMET ILKER TOPUZ

Quantitative and qualitative investigations
for muon scattering tomography
via GEANT4 simulations:
A computational study



AHMET ILKER TOPUZ

Quantitative and qualitative investigations
for muon scattering tomography
via GEANT4 simulations:
A computational study



UNIVERSITY OF TARTU

Press

1632

Institute of Physics, Faculty of Science and Technology, University of Tartu, Estonia.

Dissertation has been accepted for the commencement of the degree of Doctor of Philosophy (PhD) in Physics on 10/05/2023 by the Council of the Institute of Physics, University of Tartu.

Supervisors

Dr. Madis Kiisk

Institute of Physics, University of Tartu, W. Ostwaldi 1, 50411, Tartu, Estonia

Dr. Andrea Giammanco

Centre for Cosmology, Particle Physics and Phenomenology, Université catholique de Louvain, Chemin du Cyclotron 2, B-1348 Louvain-la-Neuve, Belgium

Opponent

Prof. Germano Bonomi

Department of Mechanical and Industrial Engineering, University of Brescia, Italy; Istituto Nazionale di Fisica Nucleare (INFN), Pavia, Italy

The public defense will take place on 29/06/2023.

The publication of this dissertation was financed by the Institute of Physics, University of Tartu.

ISSN 1406-0647 (print)

ISBN 978-9916-27-223-7 (print)

ISSN 2806-2523 (pdf)

ISBN 978-9916-27-224-4 (pdf)

Copyright© 2023 by Ahmet Ilker Topuz

University of Tartu Press

www.tyk.ee

Contents

Acknowledgment	14
Summary	15
Kokkuvõte	20
1 Introduction	24
2 Basic tracking notions in GEANT4	28
2.1 Muon ionization	29
2.2 Elastic scattering	30
2.2.1 Coulomb scattering of muons	30
2.2.2 Multiple scattering of muons	32
2.3 Radiative processes	36
2.3.1 Muon bremsstrahlung	36
2.3.2 Positron - electron pair production by muons	36
2.3.3 Muon photonuclear reactions	37
2.4 Muon decay	37
2.5 Muon absorption	38
2.6 Implementation of muon interactions in GEANT4	38
Part 1: Energy estimation based on deflection angle	39
3 Investigation of deflection angle for muon energy classification in muon scattering tomography via GEANT4 simulations	41
3.1 Introduction	41
3.2 Average deflection angle and standard deviation	41
3.3 Hodoscope schemes and simulation properties	42
3.4 Comparison between hodoscopes without/with stainless steel layers	44
4 On muon energy group structure based on deflection angle for application in muon scattering tomography: A Monte Carlo study through GEANT4 simulations	46
4.1 Introduction	46
4.2 Deflection angle and misclassification probabilities	46
4.3 Simulation features in GEANT4	48
4.4 Simulation results	49

5	Effect of passive metallic layers on muon energy estimation by means of deflection angle for muon scattering tomography: A comparative study based on GEANT4 simulations	54
5.1	Introduction	54
5.2	Average deflection angle and standard deviation	54
5.3	Simulation scheme	55
5.4	Simulation outcomes	56
	Part 2: Material characterization	61
6	Unveiling triangular correlation of angular deviation in muon scattering tomography by means of GEANT4 simulations	63
6.1	Introduction	63
6.2	Triangular correlation	63
6.3	Simulation scheme for vertical position sensitivity	65
6.4	Simulation outcomes	67
7	Applying triangular correlation of angular deviation for multi-block materials via GEANT4 simulations	71
7.1	Introduction	71
7.2	Simulation properties	71
7.3	Simulation outcomes	73
8	Non-destructive interrogation of nuclear waste barrels through muon tomography: A Monte Carlo study based on dual-parameter analysis via GEANT4 simulations	75
8.1	Introduction	75
8.2	Definition of characteristic parameters	75
	8.2.1 Average scattering angle and standard deviation	75
	8.2.2 Relative absorption rate	76
8.3	Hodoscope scheme and simulation properties	76
8.4	Simulation outcomes	78
9	On discrimination of nuclear waste barrels subject to in-drum mixing by muon scattering tomography: A characterization study based on GEANT4 simulations	84
9.1	Introduction	84
9.2	Methodology	84
9.3	Simulation properties	85
9.4	Simulation outcomes	87

10 Energy difference between hodoscope sections in muon tomography: Application for nuclear waste barrels by means of GEANT4 simulations	93
10.1 Introduction	93
10.2 Methodology	93
10.3 Simulation properties	94
10.4 Simulation results	96
10.5 Correction factor for image reconstruction	99
Part 3: Muon source optimization	101
11 Towards energy discretization for muon scattering tomography in GEANT4 simulations: A discrete probabilistic approach	103
11.1 Introduction	103
11.2 Discrete energies and discrete probabilities	103
11.3 Implementation via G4ParticleGun in GEANT4	108
11.4 Characteristic parameters and simulation properties	109
11.5 Simulation results	111
12 Particle generation through restrictive planes in GEANT4 simulations for potential applications of cosmic ray muon tomography	114
12.1 Introduction	114
12.2 Generation via planar restriction	114
12.3 Characteristic parameters and simulation setup	118
12.4 Simulation outcomes	119
13 DOME: Discrete oriented muon emission in GEANT4 simulations	124
13.1 Introduction	124
13.2 Central focus scheme	125
13.2.1 Generation through Gaussian distributions	125
13.2.2 Generation via coordinate transformation	127
13.3 Restrictive planar focus scheme	129
14 Conclusion	130
15 Discussion	133
Appendices	134
References	143

Publications	152
Posters	153
Curriculum vitae	154
Elulookirjeldus	156

List of Figures

1	Definition of the deflection angle denoted by θ according to the hit points in the detector layers.	41
2	Layouts of (a) the current hodoscope without the stainless steel layers (b) the alternative hodoscope with the stainless steel layers.	43
3	Variation of the average deflection angles versus the energy increase (a) in the present hodoscope (b) in the alternative hodoscope with the stainless steel layers.	44
4	Effect of the stainless steel layers on the trend in the coefficient of variation.	45
5	Linear overlap of the deflection angles generated by four muon energy groups composed of 0.5, 1.5, 3, and >3 GeV.	49
6	Overlapping areas for the adjacent energy groups (a) 0.5 and 1.5 GeV, (b) 1.5 and 3 GeV, and (c) 3 and >3 GeV in the four-group structure by using a modified Gaussian PDF.	50
7	Linear overlap of the deflection angles generated by three muon energy groups composed of 0.5, 2.25, and >3 GeV.	52
8	Overlapping areas for the adjacent energy groups (a) 0.5 and 2.25 GeV and (b) 2.25 and >3 GeV in the three-group structure by using a modified Gaussian PDF.	53
9	Comparison of linear overlaps over a three-group energy categorization by using a finite linear approximation for the simulation cases (a) without stainless steel layers and (b) with stainless steel layers.	58
10	Contrast between the hodoscope schemes (a)-(b) without stainless steel layers and (c)-(d) with stainless steel layers over a three-group energy classification by means of positively defined modified Gaussian distributions.	59
11	Delineation of angular deviation due to the target volume in our tomographic scheme: (a) scattering angle denoted by θ and (b) triangular correlation between $\theta = \text{BC}\angle\text{DE}$ and the interior angles denoted by $\text{BC}\angle\text{CD}$ and $\text{CD}\angle\text{DE}$ after splitting.	64
12	Simulation schemes for the position sensitivity by using three different vertical VOI centers with (a) origin at (0, 0), (b) up at (30, 0), and (c) down at (-30, 0) in cm.	66
13	Average $\text{BC}\angle\text{DE}$ via five seed numbers (a) over the energy interval between 0.1 and 8 GeV and (b) over a three-group energy structure in accordance with Eqs. (55) and (56) by including the angular resolution of 1 mrad.	68
14	Average $\text{BC}\angle\text{DE}$ and the corresponding standard deviation as defined in Eq. (42) by using four different number of particles.	69

15	Comparison between the average angular deviations over (a) BC∠DE, (b) BC∠CD, (c) CD∠DE, and (d) sum of BC∠CD and CD∠DE for three different positions.	70
16	Simulation setup for the multi-block material configuration that consists of concrete, stainless steel, and uranium.	72
17	Simulation outcomes for the multi-block material system that consists of concrete, stainless steel, and uranium.	74
18	Illustration of simulation components (a) layout of the nuclear waste barrel within the tomographic system and (b) reproduced geometry in GEANT4.	77
19	Distribution of the scattering angles for the nuclear waste barrels with a step length of 1 mrad over the energy interval between 0.1 and 8 GeV.	79
20	Variation of the average scattering angle with respect to the energy bins with a bin length of 0.5 GeV over the energy interval between 0.1 and 8 GeV by recalling the standard deviations listed in Table 8.	81
21	Relative absorption rates of the nuclear waste barrels over the energy interval between 0.1 and 8 GeV by reminding the standard deviations tabulated in Table 9.	83
22	Scheme of the homogenized nuclear waste barrel in which the concrete and the radioactive waste are mixed.	86
23	Distribution of the scattering angles for the nuclear waste barrels subject to in-drum mixing with a step length of 1 mrad over the energy interval between 0.1 and 8 GeV.	87
24	Variation of the average scattering angle with respect to the energy bins with a bin length of 0.5 GeV over the energy interval between 0.1 and 8 GeV.	88
25	Distribution of the xz-displacement for the nuclear waste barrels subject to in-drum mixing with a step length of 0.1 cm over the energy interval between 0.1 and 8 GeV.	90
26	Variation of displacement with respect to the energy bins with a bin length of 0.5 GeV over the energy interval between 0.1 and 8 GeV.	92
27	Relative absorption rates for the nuclear waste barrels subject to in-drum mixing over the energy interval between 0.1 and 8 GeV.	92
28	Tomographic setup for the collection of energy values.	94
29	Spectral difference between hodoscope sections for nuclear waste barrels over the energy interval between 0.1 and 8 GeV.	98
30	Comparison between discrete energy histograms (a) 80-bin D-CRY compared to CMSCGEN and (b) 36-bin EXP-BESS.	107

31	Scheme of probability grid implemented via G4ParticleGun in GEANT4.	108
32	Contrast between the input dataset before processing with the probability grid and the output values through the activation of our probability grid (a) 80-bin D-CRY and (b) 36-bin EXP-BESS.	109
33	Delineation of scattering angle within the present tomographic configuration.	110
34	Difference between the angular counts by using a step length of 1 mrad (a) 80-bin D-CRY and (b) 36-bin EXP-BESS. . .	112
35	Depiction of particle generation through restrictive planes in GEANT4 (a) generative point - restrictive plane scheme and (b) generative - restrictive planar interplay.	115
36	Simulation previews by using restrictive plane b for copper in GEANT4 (a) point - plane scheme and (b) plane - plane scheme.	117
37	Delineation of the generated particles from the hemispherical source with a momentum direction towards the origin. . . .	125
38	Spherical variables consisting of θ and φ with respect to the Cartesian coordinates (x,y,z).	127
39	Hemispherical muon source in GEANT4 with radius=100 cm.	129

List of Tables

1	Misclassification probabilities for the four-group structure where $E_{\text{Mean},i} = 0.5, 1.5, 3, > 3$	51
2	Misclassification probabilities for the three-group structure where $E_{\text{Mean},i} = 0.5, 2.25, > 3$	53
3	Average deflection angles and standard deviations obtained through a three-group energy structure for the cases without stainless steel layers and with stainless steel layers, respectively.	56
4	Misclassification probabilities for the cases without stainless steel layers and with stainless steel layers, respectively. . . .	60
5	Simulation features.	67
6	Simulation properties.	73
7	Simulation properties.	78
8	Average scattering angles of the nuclear waste barrels and their corresponding standard deviations over the energy interval between 0.1 and 8 GeV.	80
9	Number of the absorbed muons within the nuclear waste barrels by using five seed numbers over the energy interval between 0.1 and 8 GeV.	82
10	Simulation properties.	86
11	Scattering angles of the nuclear waste barrels subject to internal mixing and their corresponding standard deviations over the energy interval between 0.1 and 8 GeV.	89
12	Displacement due to the nuclear waste barrels subject to internal mixing and their corresponding standard deviations over the energy interval between 0.1 and 8 GeV.	91
13	Simulation properties.	96
14	Energy difference between hodoscope sections and their corresponding standard deviations for the nuclear waste barrels over the energy interval between 0.1 and 8 GeV.	97
15	D-CRY discrete probabilities between 0 and 8 GeV.	105
16	Discrete EXP-BESS probabilities between 0 and 8.1 GeV.	106
17	Simulation properties.	111
18	Characteristic parameters obtained via 80-bin D-CRY as well as 36-bin EXP-BESS.	113
19	Simulation features.	118
20	Point - plane scheme, restrictive plane a, thickness=10 cm.	119
21	Point - plane scheme, restrictive plane b, thickness=10 cm.	120
22	Point - plane scheme, restrictive plane c, thickness=10 cm.	120
23	Plane - plane scheme, restrictive plane a, thickness=10 cm.	121
24	Plane - plane scheme, restrictive plane b, thickness=10 cm.	121
25	Plane - plane scheme, restrictive plane c, thickness=10 cm.	122

26	Point - plane scheme, restrictive plane b, thickness=40 cm. .	122
27	Plane - plane scheme, restrictive plane b, thickness=40 cm.	123

Acknowledgment

In the course of this PhD study, I cannot ignore the support of my family. I also appreciate the time and the effort that was tremendously spent by my supervisors, Madis Kiisk and Andrea Giammanco. It is my duty to mention the partial financial support from the SilentBorder project.

Summary

The goal of this PhD thesis is to study the computational aspects of muon tomography, the purpose of which is to characterize the target materials such as nuclear materials in diverse applications. We present our outcomes in a quantitative as well as in a qualitative format when/if necessary. This collection is envisaged to constitute my PhD thesis. First, we attempt to estimate the kinetic energy of the incoming muons by using the deflection angle through the detector layers fabricated from polyvinyl toluene. Secondly, in addition to the derivation of the triangular correlation, we determine the characteristic parameters such as the scattering angle, the muon absorption, and the muon displacement for the bulky nuclear waste barrels as well as the homogenized nuclear waste barrels. Finally, rather than using the vertical muons with either a constant energy or a uniform energy distribution, we try to sophisticate the muon sources by utilizing a restrictive plane and a discretized energy spectrum. This PhD thesis is summarized as follows.

In chapter 1, we briefly outline the literature related to the muon tomography that is referred during our studies.

In chapter 2, the preliminary information about the muon tracking by means of the GEANT4 simulations [1] is summarized in accordance with the physics reference manual of GEANT4 10.7 [2] along with the implementation steps in [3], all the equations as well as all the expressions of which are narrated by respecting the existing notations therewithin.

In chapter 2.6, by employing the GEANT4 code, we show that the deflection angle decays as a function of the kinetic energy, and the numerical values for the current configuration are below the detector accuracy except the initial energy bins owing to the low-Z, low density, and low thickness of the current plastic scintillators. This implies the necessity of additional components that provoke the muon scattering. Therefore, we introduce stainless steel surfaces into the top and bottom sections in order to amplify the deflection angle as well as to reduce the uncertainty, thereby improving the detector performance.

In chapter 4, we address the problem of the muon energy classification for a tomographic system consisting of 0.4-cm plastic scintillators manufactured from polyvinyl toluene and we explore a four-group classification besides a ternary partitioning between 0.25 and 8 GeV. In the first instance, we determine the deflection angles by tracking the hit locations in the detector layers on the sub-divided uniform energy intervals. In the latter step, we express two misclassification probabilities where the first approach assumes a symmetrical linear propagation bounded by one standard deviation in one dimension, whereas the second procedure employs a positively defined modified Gaussian distribution that governs the overlapping area in

two dimensions. In the final stage, we compare qualitatively and quantitatively the adjacent energy groups by using the computed misclassification probabilities. In the absence of any further data manipulation, we explicitly show that the misclassification probabilities increase when the number of energy groups augments. Furthermore, we also conclude that it is feasible to benefit from the mean deflection angle to roughly estimate the muon energies up to four energy groups by taking the misclassification probabilities into consideration, while the classification viability significantly diminishes when the partition number exceeds four on the basis of standard deviation.

In chapter 5, we contrast our current tomographic prototype, which consists of the detector layers manufactured from polyvinyl toluene besides a detector accuracy of 1 mrad, with an alternative hodoscope scheme containing stainless steel layers by aiming to investigate the three-group energy structure. Initially, we determine the average deflection angles together with the corresponding standard deviations for our present setup as well as for the alternative scheme. In the second place, we express a brace of misclassification probabilities founded on the standard deviations where the first procedure assumes a linear finite approximation, whereas the latter approach rests on a positively defined modified Gaussian distribution. Upon our simulation results, we demonstrate that the introduced stainless steel layers in the proposed hodoscope setup do not only serve to augment the average deflection angles, but they also diminish the misclassification probabilities, therewith reducing the classification uncertainty as well as improving detection performance.

In chapter 6, we split the scattering angle into two separate angles by creating a triangular correlation in such a way that the scattering angle is referred to an exterior angle, whereas the separate angles are considered the interior opposite angles that are not neighboring this exterior angle. We first show that a combination of three detector layers out of four fulfills the calculation of the interior opposite angles. Then, by employing the GEANT4 simulations over our tomographic configuration composed of three plastic scintillators in above and below the volume-of-interest (VOI), we demonstrate that the interior opposite angles differ towards the vertical spatial variation, while the exterior angle approximately remains constant, thereby implying a beneficial feature to be used for the image reconstruction purposes.

In chapter 7, we apply this triangular correlation for a multi-block material configuration that consist of concrete, stainless steel, and uranium. By changing the order of this material set, we employ the GEANT4 simulations and we show that the triangular correlation is valid in the multi-block material setups, thereby providing the possibility of supportive information for the coarse prediction of the material order in such configurations.

In chapter 8, we employ the Monte Carlo simulations by using the

GEANT4 code to demonstrate the capability of muon tomography based on the dual-parameter analysis in the examination of the nuclear waste barrels. Our current hodoscope setup consists of three top and three bottom plastic scintillators. By simulating with a narrow planar muon beam of $1 \times 1 \text{ cm}^2$ over the uniform energy interval between 0.1 and 8 GeV, we determine the variation of the average scattering angle together with the standard deviation by utilizing a 0.5-GeV bin length, the counts of the scattering angle by using a 1-mrad step, and the number of the absorption events for the five prevalent nuclear materials starting from cobalt and ending in plutonium. Via the duo-parametric analysis that is founded on the scattering angle as well as the absorption in the present study, we show that the presence of the nuclear materials in the waste barrels is numerically visible in comparison with the concrete-filled waste drum without any nuclear material, and the muon tomography is capable of distinguishing these nuclear materials by coupling the information about the scattering angle and the number of absorption in the cases where one of these two parameters yields strong similarity for certain nuclear materials.

In chapter 9, motivated by the feasibility verification of cosmic ray muon tomography in the discrimination of the nuclear waste/cement mixtures, we employ the GEANT4 simulations by using our tomographic setup consisting of plastic scintillators in order to determine the characteristic parameters such as the scattering angle, the muon absorption, and the muon displacement owing to the nuclear waste barrels exposed to the in-drum mixing over a set of radioactive materials consisting of cobalt, strontium, caesium, uranium, and plutonium in the present study. Upon our simulation results based on a cylindrical stainless steel drum in which the nuclear materials are homogeneously combined with the regular concrete, we show that the presence of uranium and plutonium in the cementitious forms is qualitatively and quantitatively visible from the characteristic parameters, while the remaining radioactive waste/cement mixtures with the nuclear sources such as cobalt, strontium, and caesium do not exhibit a significant difference in comparison with the ordinary concrete slab since the intrinsic properties of the resulting mixtures that shape the characteristic parameters are predominantly governed by the matrix properties unless the associated additives are drastically denser along with the substantially higher Z-values.

In chapter 10, by using the GEANT4 simulations, we first elaborate this energy difference over the nuclear waste barrels that contain cobalt, strontium, caesium, uranium, and plutonium. We show that the deposited energy through these VOIs is not negligible for the initial energy bins. Then, we suggest a correction factor for the image reconstruction codes where the initial kinetic energy of the entering muons is coarsely predicted in accordance with the deflection angle through the hodoscope sections, thereby renormalizing the deflection angle in the bottom hodoscope depending on

the intrinsic properties of the corresponding VOIs. This correction factor encompasses useful information about the target volume traversed by the muons since it is related to the intrinsic features of the VOI. Therefore, it might be utilized in order to complement the scattering information as an input to the image reconstruction.

In chapter 11, by attempting to eliminate the disadvantageous complexity of the existing particle generators, we present a discrete probabilistic scheme adapted for the discrete energy spectra. In our multi-binned approach, we initially compute the discrete probabilities for each discrete energy bin, the number of which is flexible depending on the computational goal, and we solely satisfy the imperative condition that requires the sum of the discrete probabilities to be the unity. Regarding the implementation in the GEANT4 code, we construct a one-dimensional probability grid that consists of sub-cells equaling the number of the energy bin, and each cell represents the discrete probability of each energy bin by fulfilling the unity condition. Through uniformly generating random numbers between 0 and 1, we assign the discrete energy in accordance with the associated generated random number that corresponds to a specific cell in the probability grid. This probabilistic methodology does not only permit us to discretize the continuous energy spectra based on the Monte Carlo generators, but it also gives a unique access to utilize the experimental energy spectra measured at the distinct particle flux values. Ergo, we initially perform our simulations by discretizing the muon energy spectrum acquired via the CRY generator over the energy interval between 0 and 8 GeV along with the measurements from the BESS spectrometer and we determine the average scattering angle, the root-mean-square of the scattering angle, and the number of the muon absorption by using a series of slabs consisting of aluminum, copper, iron, lead, and uranium. Eventually, we express a computational strategy in the GEANT4 simulations that grants us the ability to verify as well as to modify the energy spectrum depending on the nature of the information source in addition to the exceptional tracking speed.

In chapter 12, by attempting to resolve the angular complication during the particle generation for the muon tomography applications in the GEANT4 simulations, we exhibit an unconventional methodology that is hinged on the direction limitation via the vectorial construction from the generation location to the restriction area rather than using a certain angular distribution or interval. In other words, we favor a momentum direction that is determined by a vector constructed between an initial point randomly chosen on a generative point/plane and a latter point arbitrarily selected on a restrictive plane of the same dimensions with the basal cross section of the VOI. On account of setting out such a generation scheme, we optimize the particle loss by keeping an angular disparity that is directly dependent on the VOI geometry as well as the vertical position of the re-

restrictive plane for a tomographic system of a finite size. We demonstrate our strategy for a set of target materials including aluminum, copper, iron, lead, and uranium with a dimension of $40 \times 10 \times 40 \text{ cm}^3$ over three restrictive planes of different positions by using a discrete energy spectrum between 0.1 and 8 GeV and we compute the scattering angle, the number of absorption, and the particle loss. Upon our simulation outcomes, we show that the particle generation by means of restrictive planes is an effective strategy that is flexible towards a variety of computational objectives.

In chapter 13, we exhibit an elementary strategy that might be at disposal in diverse computational applications in the GEANT4 simulations with the purpose of hemispherical particle sources. To further detail, we initially generate random points on a spherical surface for a sphere of a practical radius by employing Gaussian distributions for the three components of the Cartesian coordinates, thereby obtaining a generating surface for the initial positions of the corresponding particles. Since we do not require the half bottom part of the produced spherical surface for our tomographic applications, we take the absolute value of the vertical component in the Cartesian coordinates by leading to a half-spherical shell, which is traditionally called a hemisphere. Last but not least, we direct the generated particles into the target material to be irradiated by favoring a selective momentum direction that is based on the vector construction between the random point on the hemispherical surface and the origin of the target material, hereby optimizing the particle loss through the source biasing. In the end, we incorporate our strategy by using G4ParticleGun in the GEANT4 code. While we plan to exert our strategy in the computational practices for muon scattering tomography, this source scheme might find its straightforward applications in different neighboring fields including but not limited to atmospheric sciences, space engineering, and astrophysics where a 3D particle source is a necessity for the modeling goals.

Kokkuvõte - Müüoni kvantitatiivsed ja kvalitatiivsed uuringud hajuv tomograafia GEANT4 simulatsioonide kaudu: Arvutuslik uuring

Käesolev, kogumiku vormis esitatud doktoritöö on läbi viidud arvutusliku füüsika meetoditega, mille eesmärk on ühelt poolt uurida müüonite käitumist tomograafilises süsteemis ning teiselt poolt kasutada uuritavat tomograafilist süsteemi materjalide karakteriseerimiseks erinevates rakendustes. Esimeses uurimuses hindasime sissetulevate müüonite kineetilise energia määramise meetodit, kasutades polüvinüültoleuenist valmistatud detektorites toimuvat müüonite hajumisnähtust. Teises uurimuses hindame hajumistsentri määramise teostatavust sisenevale ja väljuvale müüontrajektoorile trigonomeetrilisel meetodil. Kolmandas uurimuses määrame homogeniseerimata ja homogeniseeritud tuumajäätmekonteinerites sisalduvate tuumajäätmetele neid karakteriseerivad parameetrid: hajumise nurk, müüonite neeldumistugevus ja müüonite trajektooride nihe tomograafilises süsteemis. Neljandas uurimuses tegeleme modelleerimiskeskonnas GEANT4 kasutatava müüonkiirgusallika arendamisega: diskreetse energia ning planaarse müüonallika asemel lõime erinevaid, keerukamaid müüonallikaid, mis võimaldavad viia simulatsioone GEANT4 loodud tomograafilistes süsteemides läbi efektiivsemalt. Allpool on esitatud doktoritöö kokkuvõte peatükkide kaupa.

Peatükis "Introduction" võtame lühidalt kokku doktoritöös käsitletavate teemadega seotud taustainfo ja kirjandusviited.

Peatükis "Basic tracking notions in GEANT4" on esitatud kirjeldus müüoni-aine interaktsioonide kohta, GEANT4s läbi viidud simulatsioonide füüsikaline taust koos võrrandite ja avaldistega on esitatud GEANT4 juhendi 10.7 põhjal.

Peatükis "Investigation of deflection angle for muon energy classification in muon scattering tomography via GEANT4 simulations" tõestame GEANT4 abil, et müüoni hajumisnurk korreleerub selle kineetilise energiaga ning nähtust saab kasutada müüonite energia hindamiseks. Kuid mudelis loodud detektorsüsteemis toimuv hajumine on väiksem kui reaalistliku, füüsilise, plastisstsintillaatoritest ehitatud hodoskoobiga saavutatav mõõtetäpsus. See tähendab, et hodoskoopi on vaja lisada materjalide kihte, mis võimendaks müüonite hajumist. Seetõttu panime ülemisse ja alumisse hodoskoobi sektsiooni terasest plaadid, et võimendada hajumistugevust ja vähendada statistilist määramatus, parandades seeläbi müüonite energia määramise võimet.

Peatükis "On muon energy group structure based on deflection angle for application in muon scattering tomography: A Monte Carlo study through GEANT4 simulations" käsitleme polüvinüültoleuenist valmistatud

0.4 cm paksustest plaststintillaatoritest koosneva tomograafilise süsteemi müüonite energiarihmadesse jaotamise võimalusi ja võrdleme kolme ning nelja rühma jaotamise võimalusi ja puuduseid müüonspektri energiapiirkonnale 0.25-8 GeV. Kõigepealt arvutame müüonite hajumisnurgad erinevatele energiaintervallidele. Viimases etapis arvutame külgnevatele energiaintervallidele valepositiivsete klassifitseerimistõenäosused. Kolme- ja neljarühmalise jaotuse klassifitseerimistulemused näitavad, et positiivse klassifitseerimise tõenäosus väheneb rühma hulga kasvuga. Lisaks järeldame ka, et keskmise hajumisnurga abil ligikaudselt hinnata müüoni energiat kuni nelja rühmaga jaotuste korral, kuid väheneb oluliselt, kui rühmade arv ületab nelja.

Peatükis "Effect of passive metallic layers on muon energy estimation by means of deflection angle for muon scattering tomography: A comparative study based on GEANT4 simulations" võrdleme meie praegust tomograafilist prototüüpi, mis koosneb polüvinüültoleenist valmistatud 1 mrad mõõtetäpsusega detektorikihtidest hodoskoobiga, alternatiivse hodoskoobiga, millele on lisaks eelnevalt kirjeldatule lisatud roostevabast terasest plaadid. Arvustasime mõlemale hodoskoobitüübile keskmised müüonite hajumisnurgad. Lisaks arvustasime standardhälvetel põhinevate valepositiivsete klassifitseerimise tõenäosused ühtlase ning Gaussi jaotuse korral. Võrdlusmõõtmised näitavad, et roostevabast terasest plaadid mitte ainult ei suurenda keskmisi hajumisnurki, vaid parandavad ka klassifitseerimise tõenäosusi.

Peatükis "Unveiling triangular correlation of angular deviation in muon scattering tomography by means of GEANT4 simulations" jagame tomograafilist süsteemi läbiva müüonikiire trajektoori kolmeks ning lahutame süsteemis tekkiva kogu hajumisnurga kaheks eraldi nurgaks. GEANT4 läbiviidud simulatsioonide abil on võimalik näidata, et nende kahe hajumisnurga suhte abil on võimalik leida objekti asukohta tomograafi mõõtekambris müüonikiirguse trajektooriga. Leitud seos võimaldab parandada tomograafilise rekonstruktsiooni tulemusi.

Peatükis "Applying triangular correlation of angular deviation for multi-block materials via GEANT4 simulations" rakendame eelmises peatükis uuritud seost betoonist, roostevabast terasest ja uraaniplokkudest koosneva mõõtekonfiguratsiooni jaoks. Leidsime, et nimetatud materjalide järjekorda muutes, muutub ka lahutatud hajumisnurkade suhe, mis võimaldab saada lisateavet materjalide järjestuse ja paiknemise kohta tomograafi mõõtekambris.

Peatükis "Non-destructive interrogation of nuclear waste barrels through muon tomography: A Monte Carlo study based on dual-parameter analysis via GEANT4 simulations" uurime tuumajäätmete eristamise võimet, mis põhineb hajumis- ning neeldumisparameetrite analüüsil. Selleks loime GEANT4 mudelisse süsteemi kiiritamiseks kitsa tasapinnalise müüonikiir-

gusallika energiaspektriga vahemikus 0.1-8 GeV, mis on jagatud 0.5 GeV-laiusteks intervallideks. Arvutasime hajumisjaotustele keskmised hajumisnurgad koos standardhälbega ning neeldunud müüonite arvu erinevatele materjalide kombinatsioonidele alates koobaltist ja lõpetades plutooniumiga. Näitasime, et selline mitmik-parameetiline analüüs võimaldab eristada tuumamaterjale.

Peatükis "On discrimination of nuclear waste barrels subject to in-drum mixing by muon scattering tomography: A characterization study based on GEANT4 simulations", uurime tuumajäätmete ja betooni segude eristamisvõimet, kasutades selliseid parameetreid nagu hajumisnurk, müüonite neeldumine ja müüonitrajektoori nihe. Uuritavad radioaktiivsed materjalid - koobalt, strontsium, tseesium, uraan ja plutoonium on asetatud konteineritesse. Uuringus näitasime, et uraani ja plutooniumi olemasolu betoonis on kvantitatiivselt eristatav, samas kui ülejäänud radioaktiivsete jäätmete ja betooni segud tuumamaterjalidega, nagu koobalt, strontsium ja tseesium, ei erine oluliselt tavalisest betoonist.

Peatükis "Energy difference between hodoscope sections in muon tomography: Application for nuclear waste barrels by means of GEANT4 simulations", uurime, kuidas mõjutavad eelmises uuringus kirjeldatud radioaktiivsed konteinerid müüonkiirguse energiaspektrit ning kuidas tomograafi erinevad hodoskoobid peaksid seda arvesse võtma müüonite energiaklassidesse jaotamisel. Selgus, et nii massiivsete kehade korral on müüonite energia muutus oluline ning soovitame tomograafiliste rekonstrueerimismeetodite jaoks parandustegurit. Juhul, kui müüonite kineetilist energiat arvutatakse kahe eri hodoskoobi abil, mida läbib müüonkiirgus on erineva energiaspektriga, soovitame kasutada energiamääramisel normaliseerimist.

Peatükis "Towards energy discretization for muon scattering tomography in GEANT4 simulations: A discrete probabilistic approach" kirjeldame uurimust, mis käsitleb diskreetse energiaspektriga müüongeneraatori arendamist. Uurimuse eesmärgiks on kõrvaldada olemasolevate osakeste generaatorite ebaefektiivsus. Meetod põhineb mitmetasandilisele lähenemisele, arvutatakse iga energiaintervalli müüonite genereerimise tõenäosused, kuid energiaintervallide arv ja laius on sõltuvalt eesmärgist muutuv. Arendatud tõenäosuslik meetodika ei võimalda meil mitte ainult diskretiseerida Monte Carlo generaatoritel põhinevaid pidevaid energiaspektreid, vaid see annab ka ainulaadse võimaluse eksperimentaalsete energiaspektrite kasutamiseks. Kirjeldame ka GEANT4 tarkvaras kasutatavat simuleerimisstrateegiat, mis võimaldab suurt simuleerimiskiirust.

Peatükis "Particle generation through restrictive planes in GEANT4 simulations for potential applications of cosmic ray muon tomography", tutvustame müüonite genereerimise meetodikat, mis sõltub suunapiirangust ja genereerimise asukohast lähtuva vektorkonstruksioonist. Sellise genereerimismetoodika väljatöötamise kaudu optimeerime osakeste kadu ning

simulatsioonideks vajalikku aega. Demonstreerime strateegiat alumiinium, vase, raua, plii ja uraani kuubikute korral mõõtudega $40 \times 10 \times 40 \text{ cm}^3$ kolmel erineval positsioonil diskreetsete energiaspektrite vahemikus 0.1 kuni 8 GeV ning arvutame osakeste kao. Tulemused näitavad arendatud meetodika tõhusust.

Peatükis "DOME: Discrete oriented muon emission in GEANT4 simulations" tutvustame lihtsat strateegiat, kuidas luua efektiivne, poolkerakujuline müüongeneraator. Osakeste generaator töötab eelistatud müüonite kiiritussuunaga, mis põhineb poolkerapinnal juhuslikult müüonite genereerimiseks valitud punktide ja uuritava keha alguspunkti vahelisel vektori vahel.

1 Introduction

The principle behind the muon scattering tomography is to track the propagation of the cosmic ray muons within the target volume through which the incoming muons of a certain energy deviate from their initial trajectories after a series of physical processes predominantly depending on the atomic number, the material density, and the material thickness [4]. Muon tomography is a relatively novel imaging technique [4] that makes use of the free natural flux of muons originating from the interaction of cosmic rays in the atmosphere. One of its classes of applications is the material discrimination (e.g. for the identification of special nuclear materials), exploiting the dependence of muon-nucleus scattering on the atomic number of the material [5]. In the course of propagation, the penetrating muons are subject to the directional deviation due to any scattering medium with which they encounter, and this angular deflection varies depending on the intrinsic properties of the existing media on their trajectories. Therefore, a typical scanner for muon tomography is composed of two hodoscopes, above and underneath the object to be studied (e.g. a container or a nuclear waste barrel), such that the trajectory of the muon can be tracked before and after having crossed the volume-of-interest (VOI). Reminding the fact that the angular deviation due to the target materials actually constitutes the principal parameter to discriminate the VOI, it might be anticipated that the system components such as the detector layers also lead to a very tiny deflection for the propagating muons [6]. Whereas the average deflection angle differs according to the kinetic energy of the incoming muons, a notable number of tomographic setups based on the muon scattering either do not possess any specific instruments to measure the kinetic energies or roughly group the counted muons by using a limited number of indirect methodologies. Among the strategies in order to coarsely classify the detected muons in line with the kinetic energy might be the utilization of the deflection angle owing to the detector layers [7, 8].

During the encounter between the primary cosmic rays and the earth atmosphere, a non-negligible number of muons are generated over a wide energy spectrum. The fundamental basis, on which the muon scattering tomography is founded, is to follow the propagation of the cosmic ray muons within the VOI where the entering muons of a certain energy deflect from their initial directions in the wake of the physical processes primarily hinging on the atomic number, the material density, and the material thickness [4, 9, 10]. Among the detection modules existing in the tomographic setups based on the muon scattering are the plastic scintillators that have substantially found their application by accentuating their favorable aspects like fast rise and decay times, high optical transmission, ease of manufacturing, low cost depending on the number of channels, and large available

size [11]. The hodoscope structure for the scattering-based tomography consists of two sections that are installed atop and beneath the VOI under the investigation [5], and each section is composed of two or more distinct detector layers [12, 13] occasionally made out of plastic scintillators usually with a moderate thickness. Typical muon tomography systems are inherently incapable of directly measuring the kinetic energy of incoming muons, as that would demand the presence of a magnetic field or of Cherenkov detectors or of a very precise time-of-flight measurement, and all those options would make the cost of the apparatus increase by a large factor. However, the capability of assessing, even roughly, the energy of the incoming muons on an event per event basis can significantly enhance the precision of the tomography [7], as the deflection process depends directly on energy. In the course of the muon propagation through the detection system, the hodoscope components slightly contribute to the deviation of the transversing muons up to a certain extent, and this tiny contribution might serve to categorize the detected muons by building a binary relation between the deflection angle and the muon energy [14].

In the muon scattering tomography [4, 9, 10, 15], the scattering angle due to the VOI and its associated statistics act as the principal variables in order to discriminate as well as to reconstruct the corresponding VOIs in the image reconstruction techniques such as Point-of-Closest Approach (POCA) [16–22]. As specified by the conventional tomographic configurations based on the muon scattering [5], the entire detection system regularly includes a bottom hodoscope below the VOI in addition to a top hodoscope above the VOI on the condition of multiple detector layers present at each hodoscope [17, 18, 21].

Identification of the radioactive waste forms in the nuclear waste drums is a legislative process that is administered by the competent local authorities in accordance with the standards defined by International Atomic Energy Agency (IAEA) [23, 24]. By reminding the present generation of the radioactive waste due to the existing radioactive sources in various fields such as energy, medicine, and mining in addition to the old barrels originated in the past practices [25], the formal characterization of the nuclear waste barrels de facto requires particular attention as well as ad hoc treatment. While several different techniques based on gamma-rays and neutrons have been already exercised in order to examine the nuclear waste drums [26], the muon scattering tomography [4, 10], where the target materials, i.e. the VOI, are discriminated by tracking the muon life cycle through the utilization of the cosmic-ray muons, is also marked in a notable number of studies [12, 13, 27–30] as a promising method by highlighting its titles such as non-destructive, non-harmful, and portable. Essentially, the basic postulate of the muon scattering tomography underlines the angular deviation of the propagating muons from the initial trajectory principally depending

on the atomic number, the density, and the thickness of the target material, and this angular deflection is conventionally measured by computing the scattering angle. Along with the muon deviation due to the VOI, the tomographic setups based on the muon scattering also impart the muon absorption within the VOI, which might be utilized as a complementary characteristic parameter for the purpose of the material classification.

The emerging applications of cosmic ray muon tomography [4, 10, 15] lead to a significant rise in the utilization of the cosmic particle generators, e.g. CRY [31], CORSIKA [32], or CMSCGEN [33], where the fundamental parameters such as the energy spectrum and the angular distribution associated with the generated muons are represented in the continuous forms routinely governed by the probability density functions over the corresponding vast intervals. Despite this perceptible increase in the diversity of the muon generators, the common difficulties in the hands-on applications that might be relatively exemplified as perplexing coupling with the Monte Carlo codes, unnecessarily broad and occasionally unmodifiable parametric intervals for the specific applications, extensive execution times, and complications in the particle tracking partly remain steady. Contrary to the continuous mode, the discretized energy spectra, i.e. multi-group energy approximations to put it another way, have been ubiquitously employed in the neighboring fields such as nuclear engineering [34, 35] and medical physics [36, 37] under the umbrella of the non-analogue Monte Carlo simulations [38] on and on. Along with the discretization schemes based on the theoretical assumptions, a number of notable empirical studies founded on the advanced particle detectors such as the BESS spectrometer [39] represent the experimental energy spectra in the discrete format. While MNCP6 [40] includes the necessary algorithms to utilize the discrete energy distributions in the black box format, the general particle source (GPS) in GEANT4 [1] is the existing pre-configured module that provides the opportunity of this discrete approach through a macro file without detailing the algebraic/algorithmic phase.

The wide angular distribution [41] of the incoming cosmic ray muons in connection with either incident angle or azimuthal angle is a challenging trait that leads to a drastic particle loss in the course of parametric computations through the GEANT4 [1] simulations associated with the muon tomography [4, 10, 15] since the tomographic configurations as well as the target geometries also influence the processable number of the detected particles apart from the generation strategies. To further detail, the basic parameters such as the scattering angle, the particle displacement, and the particle absorption owing to the VOI *de facto* dictate the particle penetration through the multiple sections of the tomographic setup in addition to the VOI. Hence, a number of the loss cases notably come into effect unless the calculation conditions are fulfilled, and not only the computation

statistics as well as the numerical outcomes but the initial assumptions like the energy spectrum are also perturbed since the VOI accepts a significantly lower number of particles in the instance of the substantial particle loss. While a number of source biasing techniques [38] are offered by MCNP6 [40, 42] in the black box format under the class of non-analogue Monte Carlo simulations, the GEANT4 simulations are usually constrained to the existing particle generators or the general particle source (GPS) unless G4ParticleGun is favored.

2 Basic tracking notions in GEANT4

The preliminary information about the muon tracking by means of the GEANT4 simulations is briefly summarized.

Particle transport in the GEANT4 simulations [1] is the consequence of the joined actions of the GEANT4 kernel's Stepping Manager class and the involved physical processes. The process called Transportation classifies the previous geometrical volume as well as the next geometrical volume in the course of the tracking progress. The expected length at which an interaction is supposed to take place is governed by counting all processes feasible at each step. As a result, the life cycle of the corresponding particle in a particular volume is determined before traversing another volume for the other potential interactions.

The GEANT4 simulation for the passage of particles through matter is realized step by step [1]. A true step length for the next particle interaction is arbitrarily sampled by utilizing the mean free path of the interaction or by various step limitations established through different GEANT4 components. The new true step length is identified by the smallest step.

The mean free path of a particle in a medium is computed by utilizing the cross section of a specific process and the density of atoms in the GEANT4 simulations. The number of atoms per volume in a simple material is determined as shown in

$$n = \frac{\rho N_A}{A} \quad (1)$$

where N_A is the Avogadro's number, ρ is the density of medium, and A is the molar mass. Furthermore, the number of atoms per volume of the i^{th} element in a compound material is obtained by the following expression:

$$n_i = \frac{w_i \rho N_A}{A_i} \quad (2)$$

where w_i is the proportion by mass of the i^{th} element, and A_i is the molar mass of the i^{th} element. At a given energy, the mean free path of a process denoted by λ that is also called the interaction length can be expressed in terms of the total cross section as written in

$$\lambda(E) = \left(\sum_i \sigma(Z_i, E) n_i \right)^{-1} \quad (3)$$

where $\sigma(Z_i, E)$ is the total cross section per atom of the associated process, and \sum_i sums over all elements constituting the compound material. $\sum_i \sigma(Z_i, E) n_i$ also refers to the macroscopic cross section, and the mean free path is defined as the inverse of the macroscopic cross section.

The mean free path of a particle for a particular process is contingent on the medium and cannot be exactly employed in order to sample the probability of a process in a heterogeneous medium. The number of mean free paths crossed by a particle between two positions denoted by x_1 and x_2 is described as expressed in

$$n_\lambda = \int_{x_1}^{x_2} \frac{dx}{\lambda(x)} \quad (4)$$

that is independent of the crossed medium. By assuming that n_r is an arbitrary parameter indicating the number of mean free paths between an initial point and the location of interaction, it is possible to reveal that n_r has the following distribution function:

$$P(n_r < n_\lambda) = 1 - e^{-n_\lambda} \quad (5)$$

The total number of mean free paths that a particle traverses before arriving the interaction point is sampled at the beginning of the trajectory as follows:

$$n_\lambda = -\log \eta \quad (6)$$

where η is a random number lying on the interval between 0 and 1, and n_λ is updated in accordance with the following formula after each step denoted by Δx :

$$n'_\lambda = n_\lambda - \frac{\Delta x}{\lambda(x)} \quad (7)$$

until the step generated from $s(x) = \lambda(x)n_\lambda$ becomes the shortest step where the specific process is activated.

2.1 Muon ionization

Fairly relativistic charged particles apart from electrons deposit energy in a medium predominantly via ionization and atomic excitation. The mean rate of energy loss (or stopping power) is given by the Bethe-Bloch equation as written in [43]

$$\left\langle -\frac{dE}{dx} \right\rangle = Kz^2 \frac{Z}{A} \frac{1}{\beta^2} \left[\frac{1}{2} \ln \left(\frac{2m_e c^2 \beta^2 \gamma^2 T_{\max}}{I^2} \right) - \beta^2 - \frac{\delta}{2} \right] \quad (8)$$

where E is the total energy in MeV, $K = 4\pi N_A r_e^2 m_e c^2$ in $\text{MeV mol}^{-1} \text{cm}^2$, Z is the atomic number, A is the atomic weight in g/mol, $\beta = v/c$, $\gamma = 1/(1 - \beta^2)^{\frac{1}{2}}$, z is the particle charge, m_e is the electron mass, T_{\max} is the maximum kinetic energy which can be imparted to a free electron in a single collision, I is the mean excitation energy in eV, and δ is the density effect correction to the ionization energy loss. It should be carefully noted that if x

is defined as the thickness of the absorber in cm, then the units of $-dE/dx$ is in MeV/cm; on the other hand, if x is defined as the mass thickness, i.e. the product of density and thickness, then the units of $-dE/dx$ is in MeV g⁻¹ cm². According to [43], Eq. (8) is defined in MeV g⁻¹ cm² based on the listed variables.

The continuous energy loss due to ionization is determined by the aid of G4MuIonisation in GEANT4 [1], and the "discrete" part of the ionization, i.e. the delta rays produced by muons, is simulated. The corresponding models utilized in this class depending on the kinetic energy denoted by T are listed as indicated in [2]:

- G4BetheBlochModel is valid for muons with $0.2 \text{ MeV} < T < 1 \text{ GeV}$;
- G4MuBetheBlochModel is valid for muons with $T > 1 \text{ GeV}$.

For $T > 1 \text{ GeV}$, the G4MuBetheBlochModel covers the corrections [44] for bremsstrahlung on the atomic electrons. A practical analytical expression for the cross section is used, and the calculation results are significantly different from the usual elastic $\mu - e$ scattering in the region of high energy transfers and yield a non-negligible correction to the total average energy loss of high energy muons. The total cross section is written as shown in

$$\sigma(E, \epsilon) = \sigma_{\text{BB}}(E, T) \left[1 + \frac{\alpha}{2\pi} \ln \left(1 + \frac{2\epsilon}{m_e} \right) \ln \left(\frac{4m_e E(E - \epsilon)}{m_\mu^2 (2\epsilon + m_e)} \right) \right] \quad (9)$$

where $\sigma_{\text{BB}}(E, T)$ is the Bethe-Bloch cross section that is defined as

$$\sigma_{\text{BB}}(E, T) = 2\pi r_e^2 m c^2 Z \frac{z_p^2}{\beta^2} \frac{1}{T^2} \left[1 - \beta^2 \frac{T}{T_{\text{max}}} + s \frac{T^2}{2E^2} \right] \quad (10)$$

in which $s = 0$ for the spinless particles and $s = 1$ for the other particles. In Eq. (9), m_μ is the muon mass, E is the muon energy, α is a constant, and $\epsilon = \omega + T_e$ is the energy transfer where T_e is the electron kinetic energy, and ω is the energy of radiative photons.

2.2 Elastic scattering

2.2.1 Coulomb scattering of muons

Single elastic scattering process is considered an alternative to the multiple scattering (MSC) process. The asset behind the single scattering process is hinged on the utilization of the theory-based cross sections in contrast with the GEANT4 MSC model [45] that uses a number of phenomenological approximations along with the Lewis theory [46]. The process called G4CoulombScattering was implemented to simulate the single scattering of muons, but it is also applicable to electrons and ions with some physical

limitations. Since each of elastic collisions is simulated, the number of steps for the charged particles is significantly increasing in comparison with the MSC approach, and its CPU performance is correspondingly weak. However, in the low-density media (e.g. vacuum or low-density gas), the MSC approach may lead to the incorrect results, and the single scattering processes are assumed to be more appropriate. The single scattering model of Wentzel [47] is employed in a number of the MSC models, e.g. the Penelope code [48]. The Wentzel model for describing the elastic scattering of particles with charge ze ($z = -1$ for electron) by the atomic nucleus with the atomic number denoted by Z is based on the simplified scattering potential as described in

$$V(r) = \frac{zZe^2}{r} e^{-\frac{r}{R}} \quad (11)$$

where the exponential factor attempts to reproduce the effect of screening. The parameter R is a screening radius that is expressed in

$$R = 0.885Z^{-\frac{1}{3}}r_B \quad (12)$$

where r_B is the Bohr radius. In the first Born approximation [49], the elastic scattering cross section indicated by σ^W can be obtained as

$$\frac{d\sigma^W(\theta)}{d\Omega} = \frac{(ze^2)^2}{(p\beta c)^2} \frac{Z(Z+1)}{(2S+1-\cos\theta)^2} \quad (13)$$

where β is the velocity ratio of the projectile particle, and p is the momentum. The screening parameter symbolized by S is defined according to Moliere and Bethe [50] as written in

$$S = \left(\frac{\hbar}{2pR}\right)^2 \left(1.13 + 3.76 \left(\frac{\alpha Z}{\beta}\right)^2\right) \quad (14)$$

where α is the fine structure constant, and the factor in brackets is introduced to take into account the second order corrections to the first Born approximation. The total elastic cross section indicated by σ can be expressed by means of the Wentzel cross section as shown in

$$\frac{d\sigma(\theta)}{d\Omega} = \frac{\sigma^W(\theta)}{d\Omega} \left(\frac{Z}{\left(1 + \frac{q^2 R_N^2}{12}\right)^2 + 1} \right) + \frac{1}{Z+1} \quad (15)$$

where R_N is the nuclear radius, and q is the momentum transfer to the nucleus. This term takes the nuclear size effect [51] into consideration, while the second term takes into account scattering off electrons.

2.2.2 Multiple scattering of muons

Elastic scattering of muons is a pivotal component of any transport code that is associated with the passage of the muons through matter. The elastic cross section is high when the particle energy diminishes, so the MSC approach should be implemented in order to have acceptable CPU performance in the GEANT4 simulations. A universal interface called `G4VMultipleScattering` is employed by the muon-induced GEANT4 MSC process, i.e. `G4MuMultipleScattering` [52,53]. For the concrete simulation, the `G4VMscModel` interface, which is an extension of the base `G4VEmModel` interface, is utilized. The following models are available for muons:

- `G4UrbanMscModel` is applicable to all types of particles and is the default model for electrons and positrons below 100 MeV [54];
- `G4WentzelVIModel` is the default model for all charged particles including electrons and positrons above 100 MeV, and it is included in the physics list together with the `G4CoulombScattering` process that is responsible for large angle scattering [53–55].

The MSC simulation algorithms can be categorized as either detailed or condensed. In the detailed algorithms, all the collisions/interactions undergone by the associated particle are simulated. This type of simulation can be regarded as exact, and it provides the same outcomes as the solution of the transport equation. However, it can be only utilized when the number of collisions is not drastically large, which is a condition satisfied merely for the special geometries, e.g. thin foils or low density gas. In the solid or liquid media, the average number of collisions is so high, hence the detailed simulation becomes very inefficient. The high energy simulation codes employ the condensed simulation algorithms where the global effects of the collisions are simulated at the end of a track segment. The net energy loss, displacement, and change of direction of the charged particle are routinely calculated in these codes. The last two quantities are calculated from the MSC theories employed in the codes, and the accuracy of the condensed simulations is restricted by the accuracy of the MSC approximation.

The MSC theories of Molière [56], Goudsmit and Saunderson [57], and Lewis [46] are utilized in most of the particle physics simulation codes. The Lewis theory also determines the moments of the spatial distribution, whereas the theories of Molière and Goudsmit-Saunderson deliver only the angular distribution after a step. The probability distribution of the spatial displacement is not provided by any of these MSC theories. Each of the MSC simulation codes incorporates its own algorithm to determine the angular deflection, the true path length correction, and the spatial displacement of the charged particle after a given step. These algorithms responsible

for most of the uncertainties of the transport codes since they are not exact. Furthermore, due to inaccuracy of MSC, the simulation results might depend on the value of the step length, and generally user has to select the value of the step length carefully. A new class of MSC simulation, which also refers to the mixed simulation algorithms (e.g. see [58]), started to be present in the literature. The mixed algorithm simulates the hard collisions one by one, and a MSC theory is used in order to incorporate the effects of the soft collisions at the end of a given step. Such algorithms might avert the number of steps from becoming too large and might also decrease the dependence on the step length. G4WentzelVIModel [53] includes the GEANT4 original implementation of a similar methodology. The Urban MSC models existing in the GEANT4 simulations appertain to the category of the condensed simulations, and these models employ the model functions to compute the spatial as well as angular distributions after a step. These model functions have been selected in such a way as to yield the same moments of the spatial and angular distributions as described by the Lewis theory [46].

Before expounding the MSC models, it might be necessary to define the acting terms. In the GEANT4 simulations, a particle is transported by steps through the detector geometry. The shortest distance between the endpoints of a step is called the geometrical path length indicated by l_{geo} . In the absence of a magnetic field, this is a straight line. For the non-zero fields, l_{geo} is the length along a curved trajectory. Constraints on l_{geo} are imposed when particle tracks cross the volume boundaries. The path length of an actual particle, however, is usually longer than l_{geo} due to the MSC. This distance is called the true path length denoted by l_{true} . Constraints on l_{true} are imposed by the physical processes acting on the particle.

The properties of the MSC process are determined by the transport mean free paths symbolized by λ_k that are the functions of the energy in a given material.

The k^{th} transport mean free path is defined as

$$\frac{1}{\lambda_k} = 2\pi n_a \int_{-1}^1 [1 - P_k(\cos \chi)] \frac{d\sigma(\chi)}{d\Omega} d\cos \chi \quad (16)$$

where $d\sigma(\chi)/d\Omega$ is the differential cross section of the scattering, $P_k(\cos \chi)$ is the k^{th} order Legendre polynomial, and n_a is the number of atoms per volume.

Most of the mean properties of MSC computed in the simulation codes depend only on the first and second transport mean free paths. The mean value of the l_{geo} (first moment) corresponding to a given l_{true} is determined by the following expression:

$$\langle l_{\text{geo}} \rangle = \lambda_1 \left[1 - e^{-\frac{l_{\text{true}}}{\lambda_1}} \right] \quad (17)$$

Eq. (17) is an exact result for the mean value of l_{geo} if the differential cross section has axial symmetry, and the energy loss can be neglected. The transformation between l_{true} and l_{geo} is called the path length correction. This formula and the other expressions for the first moments of the spatial distribution were taken from either [58] or [59], but they were originally calculated by Goudsmit and Saunderson [57] and Lewis [46]. At the end of l_{true} , the scattering angle is θ . The mean value of $\cos \theta$ is

$$\langle \cos \theta \rangle = e^{-\frac{l_{\text{true}}}{\lambda_1}} \quad (18)$$

The variance of $\cos \theta$ can be written as

$$\delta^2 = \langle \cos^2 \theta \rangle - \langle \cos \theta \rangle^2 = \frac{1 + 2e^{-2\kappa\tau}}{3} - e^{-2\tau} \quad (19)$$

where $\tau = l_{\text{geo}}/\lambda_1$ and $\kappa = \lambda_1/\lambda_2$. The mean lateral displacement is given by a more complicated formula [58], but this quantity can also be calculated relatively easily and accurately. The square of the mean lateral displacement is

$$\langle x^2 + z^2 \rangle = \frac{4\lambda_1^2}{3} \left[\tau - \frac{\kappa + 1}{\kappa} + \frac{\kappa}{\kappa - 1} e^{-\tau} - \frac{1}{\kappa(\kappa - 1)} e^{-\kappa\tau} \right] \quad (20)$$

Here, it is assumed that the initial particle direction is parallel to the the y-axis.

As mentioned earlier, the path length correction refers to the transformation $l_{\text{true}} \rightarrow g$ and its inverse. The $l_{\text{true}} \rightarrow g$ transformation is given by Eq. (17) if the step is small and the energy loss can be neglected. If the step is not small, the energy dependence makes the transformation more complicated. For this case, Eqs. (17) and (18) should be modified as

$$\langle \cos \theta \rangle = e^{-\int_0^{l_{\text{true}}} \frac{du}{\lambda_1(u)}} \quad (21)$$

and

$$\langle l_{\text{geo}} \rangle = \int_0^{l_{\text{true}}} \langle \cos \theta \rangle_u du \quad (22)$$

The quantity $u = \cos \theta$ is sampled according to a model function $g(u)$. The shape of this function has been chosen such that Eqs. (17) and (18) are satisfied. The functional form of $g(u)$ is

$$g(u) = q[pg_1(u) + (1-p)g_2(u)] + (1-q)g_3(u) \quad (23)$$

where $0 \leq p, q \leq 1$, and g_i are in the form of simple functions of $u = \cos \theta$ normalized over the range $u \in [-1, 1]$. $g_i(u)$ have been chosen as

$$g_i(u) = \begin{cases} g_1(u) = C_1 e^{-a(1-u)} & \text{if } -1 \leq u_0 \leq u \leq 1 \\ g_2(u) = C_2 \frac{1}{(b-u)^d} & \text{if } -1 \leq u \leq u_0 \leq 1 \\ g_3(u) = C_3 & \text{if } -1 \leq u \leq 1 \end{cases} \quad (24)$$

where $a > 0$, $b > 0$, $d > 0$, and u_0 are the model parameters, and C_i are the normalization constants. It is worth noting that, for small scattering angles, $g_1(u)$ is nearly Gaussian if $\theta_0^2 \approx 1/a$, while $g_2(u)$ has a Rutherford-like tail for large scattering angle if $b \approx 1$ and d is not far from 2. Regarding the model parameters, a , b , d , u_0 , p , and q are not independent. The requirement that the angular distribution function $g(u)$ and its first derivative be continuous at $u = u_0$ imposes two constraints on the parameters as shown in

$$pg_1(u_0) = (1-p)g_2(u_0) \quad (25)$$

and

$$pag_1(u_0) = (1-p)\frac{d}{b-u_0}g_2(u_0) \quad (26)$$

A third constraint, which implies that $g(u)$ must give the same mean value for u , comes from Eq. (21) as written in

$$q\{p \langle u \rangle_1 + (1-p) \langle u \rangle_2\} = [1 - \alpha l_{\text{true}}]^{-\frac{1}{\alpha \lambda_{10}}} \quad (27)$$

where α can be expressed by using λ_{10} and λ_{11} in which λ_{10} is the value of λ_1 at the beginning of the step, and λ_{11} is the value of the transport mean free path at the end of the step as described in

$$\alpha = \frac{\lambda_{10} - \lambda_{11}}{l_{\text{true}} \lambda_{10}} \quad (28)$$

In Eq. (27), $\langle u \rangle_i$ denotes the mean value of u computed from the distribution $g_i(u)$. The parameter indicated by a was chosen according to a modified Highland-Lynch-Dahl formula for the width of the angular distribution [60, 61] as expressed in

$$a = \frac{0.5}{1 - \cos(\theta_0)} \quad (29)$$

where θ_0 that is the width of the approximate Gaussian projected angle distribution is defined as written in

$$\theta_0 = \frac{13.6 \text{ MeV}}{\beta p} z \sqrt{\frac{l_{\text{true}}}{X_0}} \left[1 + 0.038 \ln \frac{l_{\text{true}}}{X_0} \right] \quad (30)$$

in which p is the momentum, β is the velocity, z is the charge, and l_{true}/X_0 is the true path length in radiation length unit.

2.3 Radiative processes

2.3.1 Muon bremsstrahlung

Muon bremsstrahlung [62–64] is the electromagnetic radiation produced by the acceleration or especially the deceleration of a muon after passing through the electric and magnetic fields of a nucleus. Bremsstrahlung dominates the other muon interaction processes in the region of catastrophic collisions ($\nu \geq 0.1$), i.e. at the “moderate” muon energies above the kinematic limit for the knock-on electron production. At the high energies ($T \geq 1$ TeV), this process contributes about 40% of the average muon energy loss.

The differential cross section for the muon bremsstrahlung in the units of $\text{cm}^2/(\text{g GeV})$ can be written as

$$\frac{d\sigma(E, \epsilon, Z, A)}{d\epsilon} = \begin{cases} \frac{16}{3} \alpha N_A \left(\frac{m_e}{m_\mu} r_e \right)^2 \frac{1}{\epsilon A} Z(Z\Phi_n + \Phi_e) (1 - \nu + \frac{3}{4}\nu^2) \\ 0 \quad \text{if } \epsilon \geq \epsilon_{\text{max}} = E - m_\mu \end{cases} \quad (31)$$

where m_μ and m_e are the muon and electron masses, r_e is the electron radius, Z and A are the atomic number and atomic weight of the material, and N_A is the Avogadro’s number. By considering that E and T are the initial total and kinetic energy of the muon, and ϵ is the emitted photon energy, then $\epsilon = T - T'$ and the relative energy transfer $\nu = \epsilon/E$. Φ_n and Φ_e are the contributions from the nucleus and the electrons, respectively.

2.3.2 Positron - electron pair production by muons

Positron - electron pair production by muons [62] is defined as indicated in the following process:

$$\mu^{+,-} + \text{nucleus} \rightarrow \mu^{+,-} + e^+ + e^- + \text{nucleus} \quad (32)$$

The direct electron pair production is one of the most important muon interaction processes. At the TeV muon energies, the pair production cross section exceeds those of the other muon interaction processes over a range of energy transfers between 100 MeV and $0.1E_\mu$. The average energy loss

for the pair production increases linearly with the muon energy, and this process contributes more than half of the total energy loss rate in the TeV region.

To adequately describe the number of pairs produced, the average energy loss and the stochastic energy loss distribution, the differential cross section behavior over an energy transfer range of $5 \text{ MeV} \leq \epsilon \leq 0.1E_\mu$ must be accurately reproduced. This is because the main contribution to the total cross section is given by transferred energies $5 \text{ MeV} \leq \epsilon \leq 0.01E_\mu$ and because the contribution to the average muon energy loss is determined mostly in the region $0.001E_\mu \leq \epsilon \leq 0.1E_\mu$. For a theoretical description of the cross section, the formulation in [65] is employed on top of a correction for the finite nuclear size [66]. To take the electron pair production into consideration in the field of atomic electrons, the inelastic atomic form factor contribution in [67] is also implemented.

The differential cross section denoted by $\sigma(E, \epsilon, Z, A)$ for the pair production by muons can be written as:

$$\sigma(E, \epsilon, Z, A) = \frac{4}{3\pi} \frac{Z(Z + \zeta)}{A} N_A (\alpha r_e)^2 \frac{1 - \nu}{\epsilon} \int_0^{\rho_{\max}} G(E, \nu, \rho, Z) d\rho \quad (33)$$

where

$$G(E, \nu, \rho, Z) = \Phi_e + (m_e/m_\mu)^2 \Phi_\mu \quad (34)$$

In Eqs. (33) and (34), ρ is an auxiliary variable, and ζ takes the process on atomic electrons (inelastic atomic form factor contribution) into consideration in addition to the above-listed parameters that are already defined in Eq. (31).

2.3.3 Muon photonuclear reactions

The inelastic interaction of muons with nuclei is important at the high muon energies ($E \geq 10 \text{ GeV}$) and at the relatively high energy transfers ν ($\nu/E \geq 10^{-2}$). It is especially crucial for the light materials as well as for the study of detector response to the high energy muons, the muon propagation, and the muon-induced hadronic background. The average energy loss for this process increases almost linearly with energy, and it constitutes about 10% of the energy loss rate at the TeV muon energies.

2.4 Muon decay

The muon decay [68] with a long lifetime occurs in the forms of

$$\mu^- \rightarrow e^- + \bar{\nu}_e + \nu_\mu \quad (35)$$

and

$$\mu^+ \rightarrow e^+ + \nu_e + \bar{\nu}_\mu \quad (36)$$

G4MuonDecayChannel governs the muon decay according to the vector minus axial vector (V-A) theory [69]. The electron/positron energy is sampled from the following distribution:

$$d\Gamma = \frac{G_F^2 m_\mu^5}{192\pi^3} 2\epsilon^2(3 - 2\epsilon) \quad (37)$$

where Γ is the decay rate, G_F is the Fermi coupling constant, m_μ is the muon mass, and $\epsilon = E_e/E_{\max}$ in which E_e is the electron energy and E_{\max} is $m_\mu/2$.

2.5 Muon absorption

In the course of the muon penetration through the media, its kinetic energy is deducted by multiple mechanisms, and this collective slowing-down is implicitly contingent on the intrinsic properties of the media as well as the thickness of the media. Especially in the case of the relatively low-energetic muons, the energy loss due to the VOI might lead to either the zero-energy value or the quasi-zero-energy level that commonly results in the capture of the corresponding muon at rest. In the GEANT4 nomenclature for a negative muon denoted by μ^- , this process is entitled "muMinusCapture-AtRest".

2.6 Implementation of muon interactions in GEANT4

Implementation of the above-mentioned interactions in GEANT4 is summarized as documented in [3]. The energy loss mechanisms in GEANT4 have continuous as well as discrete parts [1, 70, 71]. The high energy transfers are expressed as a real discrete act of an interaction, whereas the low energy transfers are treated as a continuous process of the energy loss. The average value of this restricted energy loss is acquired via the integration of the following equation:

$$-\frac{dE}{dx} = \int_0^{\epsilon_m} \epsilon \sigma(\epsilon, E) d\epsilon = E \int_0^{\epsilon_m} \epsilon \nu \sigma(\epsilon, E) d \ln \nu \quad (38)$$

The restricted cross section of each process is determined and listed in the separate lambda tables as expressed in

$$\lambda(E) = \int_{\epsilon_m}^E \sigma(\epsilon, E) d\epsilon \quad (39)$$

where $\lambda(E)$ is the inverse interaction length, and ϵ_m is the same threshold value as used in Eq. (38).

Part 1: Energy estimation based on deflection angle

3 Investigation of deflection angle for muon energy classification in muon scattering tomography via GEANT4 simulations

3.1 Introduction

In this study, we investigate the muon deflection due to the plastic scintillators present in our current tomographic prototype [14, 72] that includes three detector layers with a thickness of 0.4 cm as well as an accuracy of 1 mrad in both the top section and the bottom section by determining the variation of the deflection angle with respect to the muon energy [73, 74]. We perform the Monte Carlo simulations by using the GEANT4 code [1] in order to obtain the deflection angles and we follow an experimentally replicable procedure based on the hit locations in the detector layers.

3.2 Average deflection angle and standard deviation

As described in Fig. 1, the computation of the deflection angle requires the construction of two separate vectors by utilizing at least three muon hit locations in the detector layers where the first vector is the difference between the second hit location and the first hit location, while the subtraction of the second hit location from the third hit location yields the latter vector.

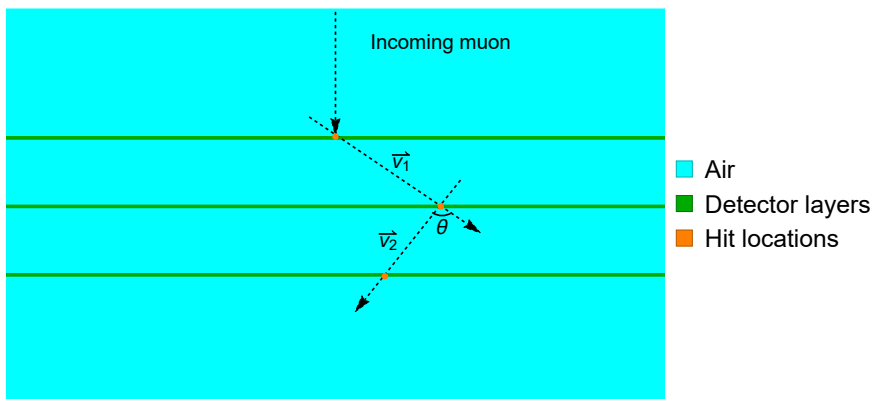


Figure 1: Definition of the deflection angle denoted by θ according to the hit points in the detector layers.

The deflection angle is obtained by using these two vectors as follows [75–77]

$$\theta = \arccos \left(\frac{\vec{v}_1 \cdot \vec{v}_2}{|\vec{v}_1| |\vec{v}_2|} \right) \quad (40)$$

Since a significant number of muons reach the detector layers, the average profile of the deflection angle at a certain energy is calculated by averaging

the previously determined deflection angles over N number of the non-absorbed/non-decayed muons as written in

$$\bar{\theta} = \frac{1}{N} \sum_{i=1}^N \theta_i \quad (41)$$

where its standard deviation is

$$\delta\theta = \sqrt{\frac{1}{N} \sum_{i=1}^N (\theta_i - \bar{\theta})^2} \quad (42)$$

In view of the fact that the deflection angle is an outcome of a stochastic process, the standard deviation of the deflection angle is expected to be reduced in order to have a better energy estimation. In essence, the average deflection angle of two different hodoscopes indicated by x and y at a given energy value over N number of the non-absorbed/non-decayed muons yields the following expression

$$\bar{\theta}_{\frac{x+y}{2}} = \frac{1}{N} \sum_{i=1}^N \frac{\theta_{x,i} + \theta_{y,i}}{2} \quad (43)$$

Consequently, its standard deviation parameterized in terms of the contributions from both the top section and the bottom section is

$$\delta\theta = \sqrt{\frac{1}{N} \sum_{i=1}^N \left(\frac{\theta_{x,i} + \theta_{y,i}}{2} - \bar{\theta}_{\frac{x+y}{2}} \right)^2} \quad (44)$$

The resulting deflection angle for our present prototype is anticipated to be very small [6], i.e. either below or in the close neighborhood of our detector accuracy that is 1 mrad. Accordingly, the necessity of a stronger deflecting medium is foreseen in order to augment the angular deviation, and we introduce a stainless steel layer of 0.4 cm, the density of which is 8 g/cm³, into the top section and the bottom section in order to join this aim. For the sake of comparison, we also explore the coefficient of variation (CV) attributed to these two configurations with respect to the energy increase, which is defined as the ratio between the standard deviation and the average value as expressed in

$$\text{CV} = \frac{\text{Standard deviation}}{\text{Average}} = \frac{\delta\theta}{\bar{\theta}} \quad (45)$$

3.3 Hodoscope schemes and simulation properties

The geometrical schemes for either setup are depicted in Figs. 2(a) and (b), and it is seen that the detector layers are separated by a distance of 10 cm,

whereas the span between these two hodoscopes is 100 cm. Furthermore, the dimensions of both the detector layers and the stainless steel layers are $100 \times 0.4 \times 100 \text{ cm}^3$.

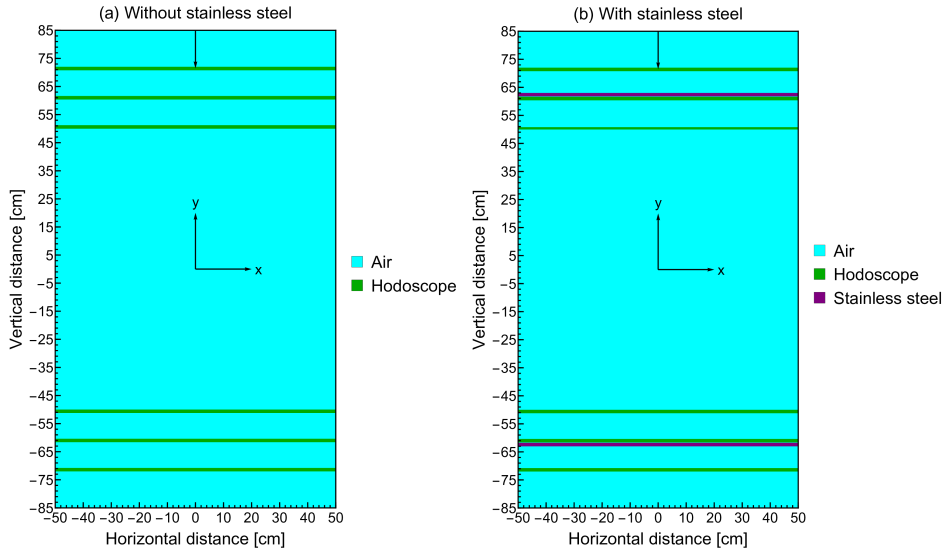


Figure 2: Layouts of (a) the current hodoscope without the stainless steel layers (b) the alternative hodoscope with the stainless steel layers.

We use a central mono-energetic mono-directional beam that is generated at $y=85 \text{ cm}$ via G4ParticleGun where the y -axis is chosen as the vertical component in the Cartesian coordinates, and the generated muons are propagating in the vertically downward direction, i.e. from the top edge of the simulation box through the bottom edge as indicated by the black arrow in Fig. 2. Noting that the distribution of the incident angle (α) is approximated via $\cos^2(\alpha)$ for an interval between $-\pi/2$ and $\pi/2$ [41], this source setup stands for a feasible approach since the present aperture of the entire detection geometry typically only covers the narrow angles besides the very rare entries around the corners. At a given energy, the number of the simulated muons is 1000, and we investigate the deflection angle for an energy interval between 0.5 and 8 GeV with an increase step of 0.5 GeV. All the materials in the current study are defined according to the GEANT4/NIST material database. The reference physics list used in these simulations is FTFP_BERT.

3.4 Comparison between hodoscopes without/with stainless steel layers

We initiate our investigation based on our first configuration by showing the simulation results for the average deflection angles in Fig. 3(a). In connection with the energy increase, the observed trend in the mean deflection angle is the exponential decay. Due to the exact symmetry in the structural composition in both the top section and the bottom section, the simulation outcomes are similar in either section. It is also seen that the resulting deflection angles are either under the detector accuracy of 1 mrad or in its close periphery, and this is a principal problem to be addressed in the present study. Regarding the standard deviations, it is demonstrated that the deflection angles are dispersed widely, rather than converging in a narrow interval, which sets the energy categorization more challenging. As described in Eq. (44), the consecutive averaging sequentially over the number of sections and the number of the non-absorbed/non-decayed muons leads to a significant reduction in the angular width.

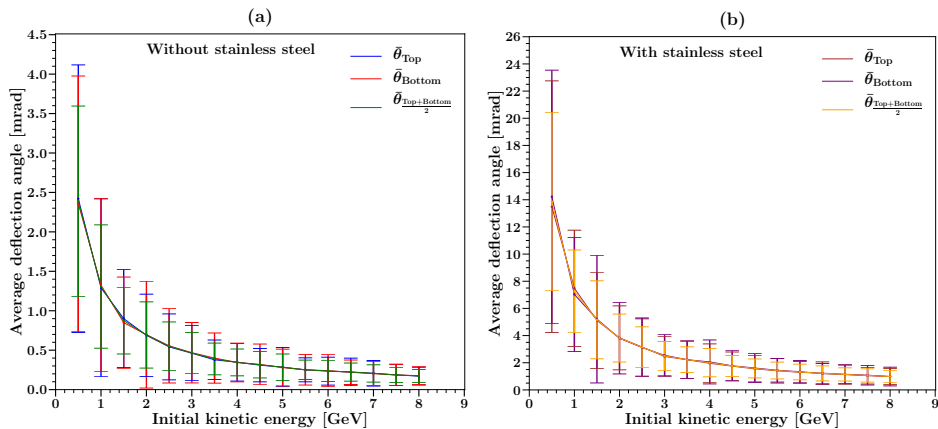


Figure 3: Variation of the average deflection angles versus the energy increase (a) in the present hodoscope (b) in the alternative hodoscope with the stainless steel layers.

After the qualitative examination of the average deflection angles for our current hodoscope, an experimental limitation that awaits to be attacked is our present detector accuracy of 1 mrad. As an alternative to a significant detector upgrade that captures angular values below 1 mrad, we propose the introduction of stainless steel layers with an optimally low thickness of 0.4 cm as well as a density of 8 g/cm³, which arouse the angular deflection, into either section as depicted in Fig. 2(b). We repeat our simulations on this

alternative configuration by using the same simulation features, and the average deflection angles along with the standard deviations for the new tomographic setup with the stainless steel layers are displayed in Fig. 3(b). In addition to the notable increase in the average deflection angles, the angular width is also remarkably reduced except the fluctuations at a couple of energy values, i.e. 1.5 and 4 GeV. Concerning the visible influence of the stainless steel layers on the standard deviations, Fig. 4 shows the trends in coefficients of variation as expressed in Eq. (45) with the intention of comparing both detector setups, and it is concretely seen that the angular uncertainty is lowered by the presence of the inserted stainless steel layers, which also means that an improved energy classification is expected from the proposed alternative scheme.

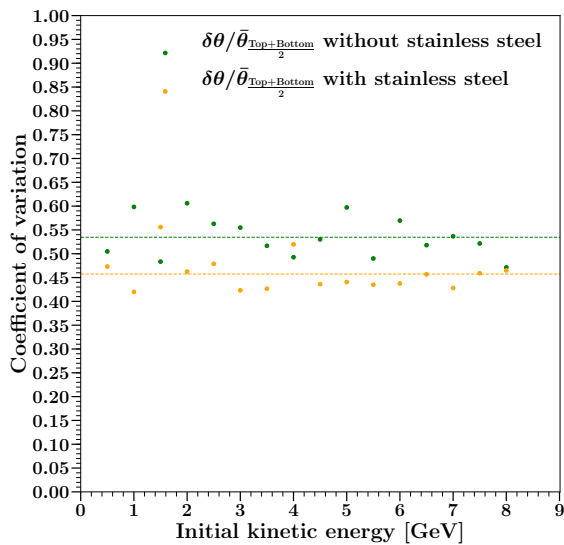


Figure 4: Effect of the stainless steel layers on the trend in the coefficient of variation.

4 On muon energy group structure based on deflection angle for application in muon scattering tomography: A Monte Carlo study through GEANT4 simulations

4.1 Introduction

This study intends to inform the choice of muon energy categories based on the internal deflection angle. The minimum number of distinct energy categories is of course limited by the angular resolution of the detection setup, but it also has an intrinsic limit due to the stochastic nature of the scattering process. To this end, in the ideal condition of perfect detectors, hence absolute angular detector resolution (similarly to previous studies in this area, such as [78–80]), we computationally analyze the energy group structure obtained via the angular deviation of the entering muons through the detector layers in our tomographic system [14] including three plastic scintillators manufactured from polyvinyl toluene in both the top section and the bottom section. This setup is representative of most muon tomography scanners proposed in the literature [4]. The present study is structured as follows. We first define the deflection angle in agreement with the deviation of the transversing muons through the detector layers. Then, we express the mean deflection angle that is averaged over the top hodoscope and the bottom hodoscope in addition to the corresponding standard deviation. In order to determine the misclassification probability, we propose two approaches where the first methodology is based on the angular linear coincidence for the adjacent energy groups within one standard deviation in one dimension, while the second procedure assumes a two-dimensional overlap governed by the positively defined modified Gaussian distributions. We simulate our approaches over a four-group as well as a three-group energy structure by using the GEANT4 code [1] and we finally expose our simulation results.

4.2 Deflection angle and misclassification probabilities

As described in Fig. 1, the deflection angle denoted by θ is the measure that indicates the internal angular deviation of an incoming muon due to the plastic scintillators. While the overall deflection from the initial trajectory is inaccessible, which results in a limiting uncertainty in the identification of materials in the VOI, the angle θ is a measurable quantity regardless of the direction of incidence. In order to compute the deflection angle, it is necessary to collect three hit locations in three detector layers, and the collected hit points serve to construct two vectors where the first vector is generated by the difference between the second hit location and the first hit

location, while the second vector is obtained by subtracting the second hit point from the third hit point. Then, the deflection angle of a detected muon is determined as expressed in Eq. (40). By assuming that the detector layers in both the top section and the bottom section capture approximately the same number of the propagating muons, the deflection angle determined for a tracked muon that hits the top hodoscope as well as the bottom hodoscope is averaged over these two sections, thereby yielding Eq. (43) where N indicates the number of simulated non-absorbed and non-decayed muons. The corresponding standard deviation is expressed as written in Eq. (44).

Recalling that the average deflection angle declines as a function of the kinetic energy, we already acquire the opportunity to set out a binary relation between the average deflection angle and the kinetic energy. Having said that it is possible to coarsely predict the kinetic energies of the tracked muons by using the average deflection angle, the standard deviation is a crucial parameter to precise the uncertainty propagated through the energy group structure since different kinetic energies periodically generate a set of similar deflection angles, which also means that the width of the angular spectrum at a given energy is sufficiently high to overlap with the angular distribution obtained at another energy level. This problem is first addressed by using an assumption such that the deflection angles obtained for two adjacent energy groups linearly coincide within one standard deviation in one dimension. Thus, for a finite linear approximation, the misclassification probability is the ratio between the overlapping length and the total length in the case of two adjacent energy groups denoted by A and B in a descending order as follows

$$P_{\text{Linear}} = \begin{cases} \frac{\bar{\theta}_B + \delta\theta_B - \bar{\theta}_A + \delta\theta_A}{\bar{\theta}_A + \delta\theta_A - \bar{\theta}_B + \delta\theta_B} & \bar{\theta}_B + \delta\theta_B > \bar{\theta}_A - \delta\theta_A \\ 0 & \bar{\theta}_B + \delta\theta_B \leq \bar{\theta}_A - \delta\theta_A \end{cases} \quad (46)$$

It is worth mentioning that the linear finite approximation conditions the misclassification probability to null if the angular spectra for two adjacent energy groups are distinct beyond one standard deviation.

The latter practice to determine the misclassification probability consists of considering the angular spectrum at a certain energy by using a positively defined modified Gaussian distribution since the deflection angle acquired through Eq. (40) is cardinally positive. Thus, based on the obtained average deflection angle as well as the corresponding standard deviation, we suggest a positively defined modified Gaussian probability density function (PDF) for an energy value of A as indicated in

$$G'(\bar{\theta}_A, \delta\theta_A, \theta) = \frac{G(\bar{\theta}_A, \delta\theta_A, \theta)}{\int_0^\infty G(\bar{\theta}_A, \delta\theta_A, \theta) d\theta} \quad (47)$$

and

$$G'(\bar{\theta}_B, \delta\theta_B, \theta) = \frac{G(\bar{\theta}_B, \delta\theta_B, \theta)}{\int_0^\infty G(\bar{\theta}_B, \delta\theta_B, \theta)d\theta} \quad (48)$$

In contrast with the finite linear approximation in Eq. (46), two overlapping distribution functions yield an area in two dimensions, and the prevalent term that is commonly utilized to describe such an area is called overlapping coefficient (OVL) as defined in

$$\text{OVL} = \int_0^\infty \min[G'(\bar{\theta}_A, \delta\theta_A, \theta), G'(\bar{\theta}_B, \delta\theta_B, \theta)]d\theta \quad (49)$$

The determination of the OVL leads to the definition of the misclassification probability for a positively defined modified Gaussian PDF by using the following expression:

$$P_{\text{Gaussian}} = \frac{\text{OVL}}{\int_0^\infty G'(\bar{\theta}_A, \delta\theta_A, \theta)d\theta + \int_0^\infty G'(\bar{\theta}_B, \delta\theta_B, \theta)d\theta - \text{OVL}} = \frac{\text{OVL}}{2 - \text{OVL}} \quad (50)$$

4.3 Simulation features in GEANT4

Our demonstrations about the misclassification probabilities are based on the simulations in the GEANT4 framework, and the tomographic setup is described in Fig. 2(a). Both the top hodoscope and the bottom hodoscope include three detector layers made of polyvinyl toluene, and the dimensions of these plastic scintillators are $100 \times 0.4 \times 100 \text{ cm}^3$ as illustrated in Fig. 2(a). We employ a central mono-energetic mono-directional beam that is generated at $y=85 \text{ cm}$ (as indicated in the figure by the downward black arrow) via G4ParticleGun, and the initiated muons are propagating in the vertically downward direction, i.e. from the top edge of the simulation box through the bottom edge. Since the incident angle (α) is approximately distributed as $\cos^2 \alpha$ within the detector acceptance of interest [41], most of the muon flux is almost vertical, hence this source setup is considered a sufficiently reliable approximation for the purposes of this study. At a given energy group, the number of the simulated muons is 10^4 , and we use a production cut-off of 0.25 GeV as well as an energy threshold of 8 GeV. We prefer a uniform energy distribution as long as a flat distribution provides a less unfavorable uncertainty [7]. All the geometrical components in the present study are defined according to the GEANT4/NIST material database. FTFP_BERT is the reference physics list that is utilized in all the simulations.

4.4 Simulation results

We commence performing our simulations with a four-group energy structure, and the muon energy interval between 0.25 and 8 GeV is divided into four sub-intervals where the energy groups are labeled with the average energy value in accordance with the corresponding sub-interval. Hence, the first group refers to a sub-interval between 0.25 and 0.75 GeV with a mean energy of 0.5 GeV, then the second group includes the incoming muons of a kinetic energy between 0.75 and 2.25 GeV with an average energy of 1.5 GeV, whereas the kinetic energy of the third group lies on an interval between 2.25 and 3.75 GeV with a mean energy of 3 GeV, and finally the fourth group represents all the muons that exceed 3 GeV on average by taking the exponential decay into account.

Following the computation of the average deflection angle as well as the corresponding standard deviation, we first verify our finite linear approximation over the four-group energy structure, and the computed parameters are shown in Fig. 5.

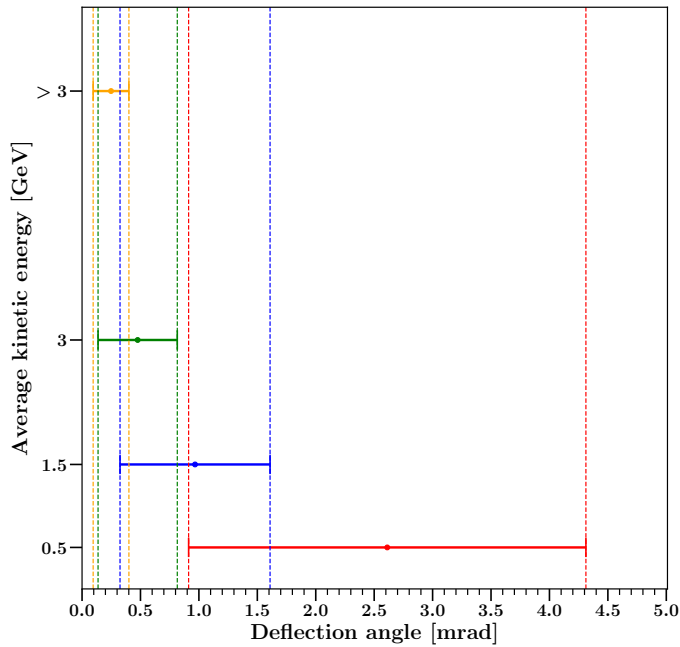


Figure 5: Linear overlap of the deflection angles generated by four muon energy groups composed of 0.5, 1.5, 3, and >3 GeV.

It is implicitly seen that the deflection angles of discrete groups share a non-negligible common interval due to the generation of the similar angular

set. It is also noticed that not only the neighboring energy groups but also the last energy group entitled >3 GeV coincides with an unconnected energy group such as 1.5 GeV. According to Fig. 5, it is relatively equitable to state that it is hard to consider a four-group approach as feasible since the total misclassified region for a four-group strategy is discouraging.

In the latter step for the same energy categorization, we link the mean deflection angle and the associated standard deviation with a positively defined Gaussian PDF, and the overlapping areas, i.e. the OVL of two adjacent energy groups, are depicted in Fig. 6.

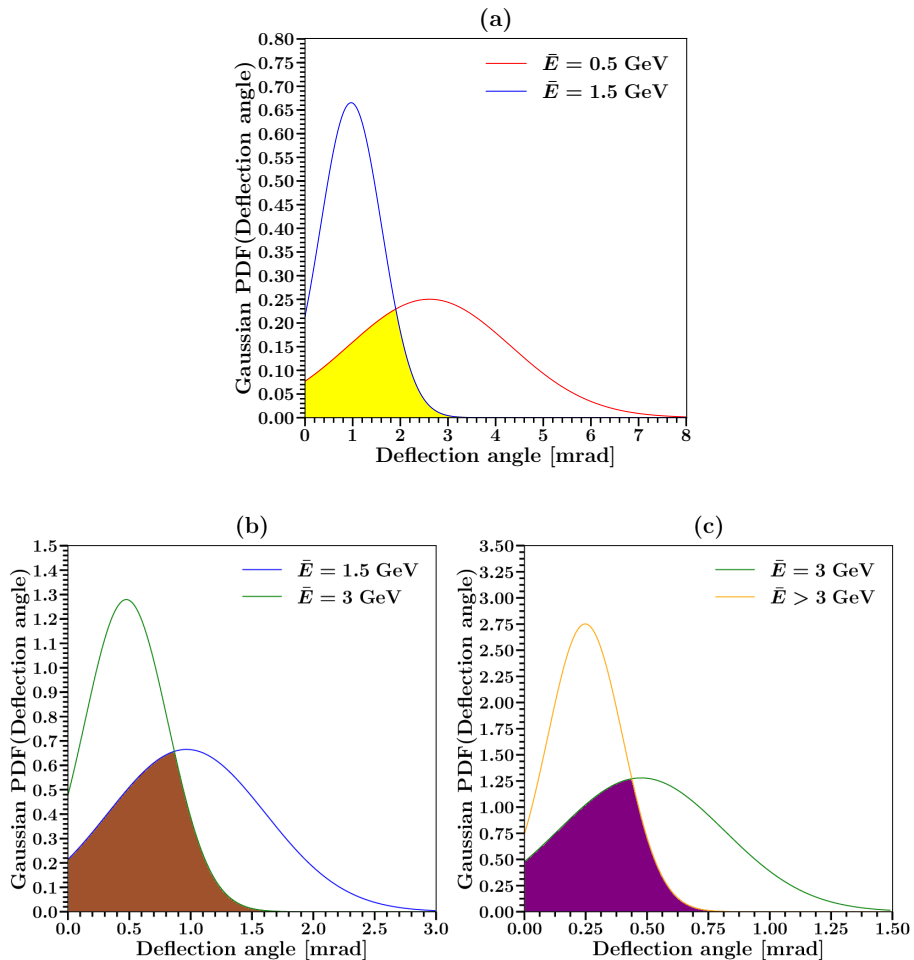


Figure 6: Overlapping areas for the adjacent energy groups (a) 0.5 and 1.5 GeV, (b) 1.5 and 3 GeV, and (c) 3 and >3 GeV in the four-group structure by using a modified Gaussian PDF.

As opposed to the linear overlap illustrated in Fig. 5, the intersection of two distribution results in an area that directly indicates the non-zero misclassified domain in any condition.

Since both the overlapping length in the linearly finite approximation and the intersection areas in the positively defined modified Gaussian PDF suffice to determine the misclassification probabilities under our assumptions, Table 1 lists the numerical values yielded by these two approaches.

Table 1: Misclassification probabilities for the four-group structure where $E_{\text{Mean},i} = 0.5, 1.5, 3, > 3$.

\bar{E} pairs [GeV]	$\bar{\theta}_{\frac{\text{Top}+\text{Bottom}}{2}} \pm \delta\theta$ pairs [mrad]	OVL	P_{Gaussian}	P_{Linear}
0.5 - 1.5	$2.612 \pm 1.700 - 0.967 \pm 0.642$	0.371	0.228	0.174
1.5 - 3	$0.967 \pm 0.642 - 0.476 \pm 0.339$	0.533	0.363	0.330
3 - > 3	$0.476 \pm 0.339 - 0.248 \pm 0.153$	0.521	0.352	0.366

At last, the initial four-group structure based on the average deflection angle and the standard deviation ends up with the large overlaps and consequently the high misclassification probabilities, which lead to the practical difficulties in consideration. However, it is also possible to envisage that the reduction in the group number is expected to eventually lead to the diminution in the overlapping intervals, thereby reducing the misclassification probabilities. Therefore, we devote our next step to another group structure that is based on three energy partitions.

By maintaining the initial energy group as well as the final energy group, we merge two previous mid-groups, i.e. labeled as 1.5 GeV and 3 GeV, into a single group that is named as 2.25 GeV where the energy interval is between 0.75 and 3 GeV. As performed in the four-group procedure, we repeat our methodologies over a three-group structure, and we first demonstrate the coincided linear intervals in Fig. 7.

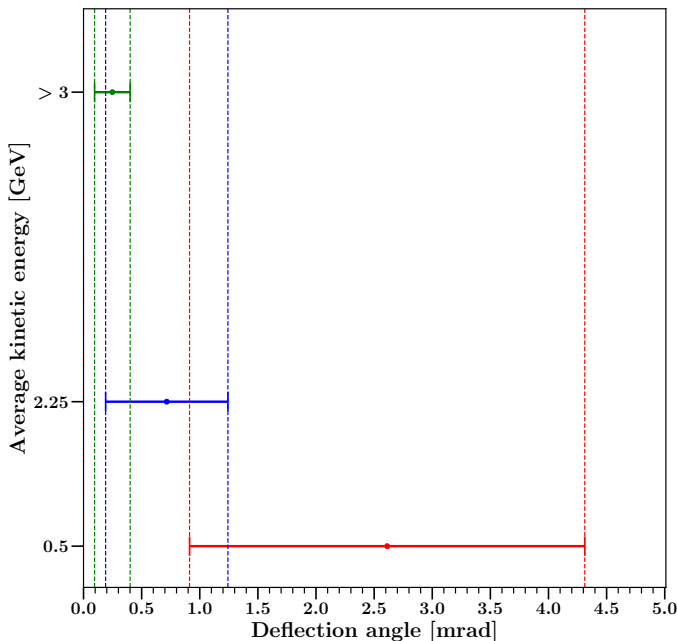


Figure 7: Linear overlap of the deflection angles generated by three muon energy groups composed of 0.5, 2.25, and >3 GeV.

In accordance with our expectation, Fig. 7 shows a significantly more optimistic outcome where the non-adjacent groups do not show any overlap addition to the visible reduction in the intersected domains. In order to check the presence of such a beneficial influence in the positively defined modified Gaussian PDF, we depict the overlapping areas for the three-group procedure in Fig. 8, and it is revealed that the intersection areas of the adjacent energy groups are diminished in comparison with Fig. 6, which also means that a reduced number of groups results in the decreased uncertainty as justified by our both approaches.

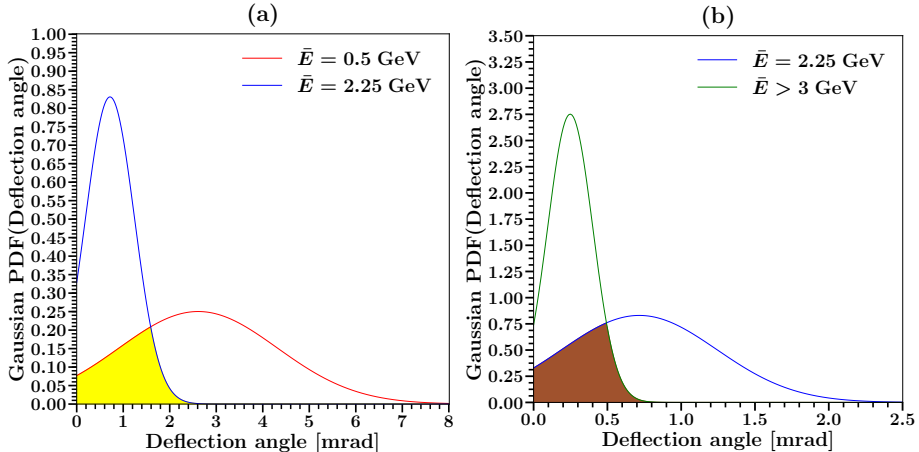


Figure 8: Overlapping areas for the adjacent energy groups (a) 0.5 and 2.25 GeV and (b) 2.25 and >3 GeV in the three-group structure by using a modified Gaussian PDF.

To numerically quantify the misclassification probabilities for the three-group structure, we tabulate our simulation results in Table 2 and we observe that the misclassification probabilities listed in Table 2 are more advantageous compared to those shown in Table 1, which implies that a three-group energy classification based on the deflection angle is relatively more feasible in the muon scattering tomography.

Table 2: Misclassification probabilities for the three-group structure where $E_{\text{Mean},i} = 0.5, 2.25, > 3$.

\bar{E} pairs [GeV]	$\bar{\theta}_{\frac{\text{Top}+\text{Bottom}}{2}} \pm \delta\theta$ pairs [mrad]	OVL	P_{Gaussian}	P_{Linear}
0.5 - 2.25	$2.612 \pm 1.700 - 0.716 \pm 0.526$	0.278	0.161	0.080
2.25 - > 3	$0.716 \pm 0.526 - 0.248 \pm 0.153$	0.330	0.197	0.180

Furthermore, it can be noted that the addition of a realistic angular uncertainty would further impede a finer binning. Table 1 shows that, in the four-group structure, even an excellent angular resolution of better than 0.5 mrad would not be sufficient to maintain these energy categories, while a realistically achievable resolution is sufficient in the three-group structure as apparent in Table 2.

5 Effect of passive metallic layers on muon energy estimation by means of deflection angle for muon scattering tomography: A comparative study based on GEANT4 simulations

5.1 Introduction

In this study, we categorize the incoming muons into three groups based on their deflection angle within the hodoscope that we use as a proxy for their kinetic energy. We compare the classification performance in this three-group energy structure between our current tomographic prototype that contains three detector layers manufactured from polyvinyl toluene with a thickness of 0.4 cm as well as an accuracy of 1 mrad in both the top section and the bottom section, and an alternative hodoscope scheme including stainless steel layers in addition. In order to quantify the uncertainty propagated through the energy groups, we present a couple of misclassification probabilities characterized by one standard deviation where the first means supposes a linear finite approximation in one dimension, while the latter procedure is governed by the positively defined modified Gaussian distributions in two dimensions. The present study is organized as follows. In section 5.2, we express the average deflection angle as well as the corresponding standard deviation in terms of the hit positions and we also introduce the corresponding expressions averaged over the top section as well as the bottom section to diminish the width of the deflection angle. While we demonstrate our simulation setup in the GEANT4 code [1] besides the simulation features in section 5.3, we exhibit our simulation results in section 5.4.

5.2 Average deflection angle and standard deviation

By reminding that the crossing muons undergo deviations from the initial trajectory owing to the interactions with matter, the deflection angle of the incoming muons throughout a set of three detector layers is estimated via constructing two distinct vectors where the first vector is defined in accordance with the hit locations on the first two detector layers, whereas the remaining vector is the sequel of the hit positions on the last two detector layers as illustrated in Fig. 1.

Upon these two vectors that suffice the computation of the angular deviation, the deflection angle of a muon crossing the detector layers denoted by θ is obtained by using Eq. (40). Since the detector layers accept a significant number of muons, the average deflection angle at a particular energy is determined by averaging the previously calculated deflection angles over N number of the non-absorbed/non-decayed muons as indicated in Eq. (41),

which refers to a standard deviation as written in Eq. (42).

In light of the fact that the deflection angle is a consequence of a stochastic process, the standard deviation of the deflection angle is anticipated to be lessened with the intention of a better energy estimation. By harking back to the entire tomographic setup consisting of two separate sections (i.e. the top section and the bottom section), each of which includes three detector layers, the deflection angle determined for each non-absorbed/non-decayed muon in each section is first averaged over the number of sections, then the mean deflection angle of both sections is re-averaged over the number of the non-absorbed/non-decayed muons according to Eq. (43).

5.3 Simulation scheme

The present study is conducted by means of the GEANT4 simulations, and we initially track the muon hit locations on the detector layers made out of polyvinyl toluene in order to calculate the average deflection angles as well as the corresponding standard deviations for the associated groups of kinetic energies. The simulation geometry for our present prototype without passive metallic layers in addition to the alternative hodoscope scheme containing stainless steel layers is depicted in Fig. 2. As described in Fig. 2(a), the dimensions of each the detector layer fabricated from polyvinyl toluene are $100 \times 0.4 \times 100 \text{ cm}^3$, and the inter-layer spacing at each section is 10 cm. In the proposed hodoscope setup, where we introduced stainless steel layers as illustrated in Fig. 2(b), the dimensions of each metallic layer are $100 \times 0.4 \times 100 \text{ cm}^3$, i.e. identical to those of the detector layers. In both the tomographic schemes, the gap between the top hodoscope and the bottom hodoscope is 100 cm into the bargain.

A central mono-directional beam with the uniform energy distribution that is generated at $y=85 \text{ cm}$ via G4ParticleGun is employed, and the generated muons are crossing in the vertically downward direction, i.e. from the top edge of the simulation box through the bottom edge as indicated with the black arrows in Fig. 2. Since the current aperture of the entire detection geometry commonly only accepts the narrow angles apart from the very rare entries around the corners, this beam setup is considered significantly reliable by reminding that the distribution of the incident angle (α) approximately corresponds to $\cos^2 \alpha$ for an interval between $-\pi/2$ and $\pi/2$ [41]. We favor a uniform energy distribution lying on an energy interval between 0.25 and 8 GeV so as to achieve the absorption minimization especially in the case of stainless steel layers besides the numerical accuracy optimization [7]. We partition the entire energy interval bounded by 0.25 and 8 GeV into three energy groups such that the first energy group consists of the energy values between 0.25 and 0.75 GeV, whereas the second energy group is composed of the muon energies between 0.75 and 3.75 GeV,

and the muon energies between 3.75 and 8 GeV finally constitute the third energy group.

For each of the three energy groups, the number of the simulated muons is 10^4 . All the materials in the current study are defined in accordance with the GEANT4/NIST material database. The reference physics list used in these simulations is FTFP_BERT. The muon tracking is sustained by G4Step, and the registered hit positions are post-processed with the assistance of a Python script where the deflection angle is first determined for every single non-absorbed/non-decayed muon of a given energy group at each hodoscope. Finally, we conclude the post-processing stage by applying Eqs. (43) and (44) on the datasets of deflection angle attained through the top hodoscope and the bottom hodoscope, thereby obtaining the average deflection angle and the corresponding standard deviation.

5.4 Simulation outcomes

Our GEANT4 simulations initially yield the average deflection angles as well as the associated standard deviations for both our current prototype and our proposed new scheme as tabulated in Table 3. By contrasting the present prototype with the alternative hodoscope in agreement with the average deflection angles in Table 3, the first positive influence of stainless steel layers in terms of the detection performance is already revealed. To better elucidate, by reminding the existing detector accuracy of 1 mrad, all the average deflection angles generated by the proposed hodoscope containing stainless steel layers exceed the angular value of 1 mrad for the three-group energy structure; on the other hand, the average deflection angles obtained through the present configuration remains below this detector accuracy in two among three energy groups, i.e. $\bar{E} = 2.25$ GeV and $\bar{E} > 3$ GeV.

Table 3: Average deflection angles and standard deviations obtained through a three-group energy structure for the cases without stainless steel layers and with stainless steel layers, respectively.

Without stainless steel				
Energy interval [GeV]	\bar{E} [GeV]	$\bar{\theta}_{\text{Top}} \pm \delta\theta$ [mrad]	$\bar{\theta}_{\text{Bottom}} \pm \delta\theta$ [mrad]	$\bar{\theta}_{\frac{\text{Top}+\text{Bottom}}{2}} \pm \delta\theta$ [mrad]
0.25 - 0.75	0.5	2.590±2.107	2.632±2.463	2.612±1.700
0.75 - 3.75	2.25	0.712±0.657	0.719±0.686	0.716±0.526
3.75 - 8	> 3	0.248±0.217	0.249±0.204	0.248±0.153
With stainless steel				
Energy interval [GeV]	\bar{E} [GeV]	$\bar{\theta}_{\text{Top}} \pm \delta\theta$ [mrad]	$\bar{\theta}_{\text{Bottom}} \pm \delta\theta$ [mrad]	$\bar{\theta}_{\frac{\text{Top}+\text{Bottom}}{2}} \pm \delta\theta$ [mrad]
0.25 - 0.75	0.5	14.797±10.915	15.055±10.871	14.925±8.310
0.75 - 3.75	2.25	4.080±3.459	4.128±3.559	4.104±2.800
3.75 - 8	> 3	1.418±1.051	1.427±1.034	1.422±0.766

On top of the augmented average deflection angles that lead to a better detection efficiency, the presence of stainless steel layers is partially expected to result in the diminished uncertainty. To verify this hypothesis over our GEANT4 simulations, the linear overlap based on the standard deviations is shown in Fig. 9, and we observe that the uncertainty in the deflection angle is apparently decreased in the case of stainless layers compared to the present hodoscope scheme without any passive metallic layers.

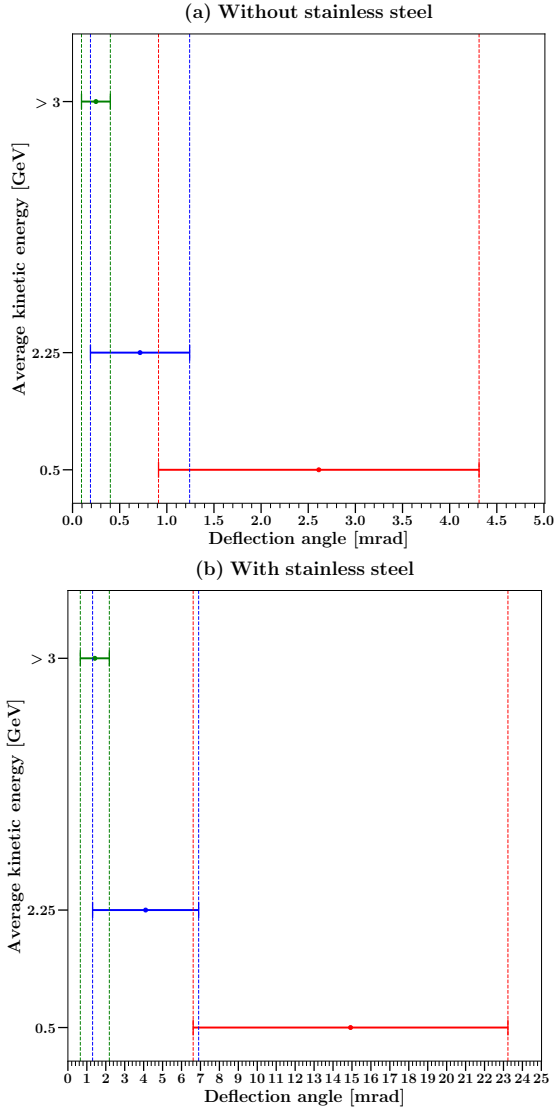


Figure 9: Comparison of linear overlaps over a three-group energy categorization by using a finite linear approximation for the simulation cases (a) without stainless steel layers and (b) with stainless steel layers.

In order to further evaluate the effect of stainless steel layers, the areal overlap of the positively defined modified Gaussian distributions as defined in Eqs. (47) and (48) is displayed in Fig. 10, and we face a similar reduction in the angular uncertainty for the reason of the areal contraction.

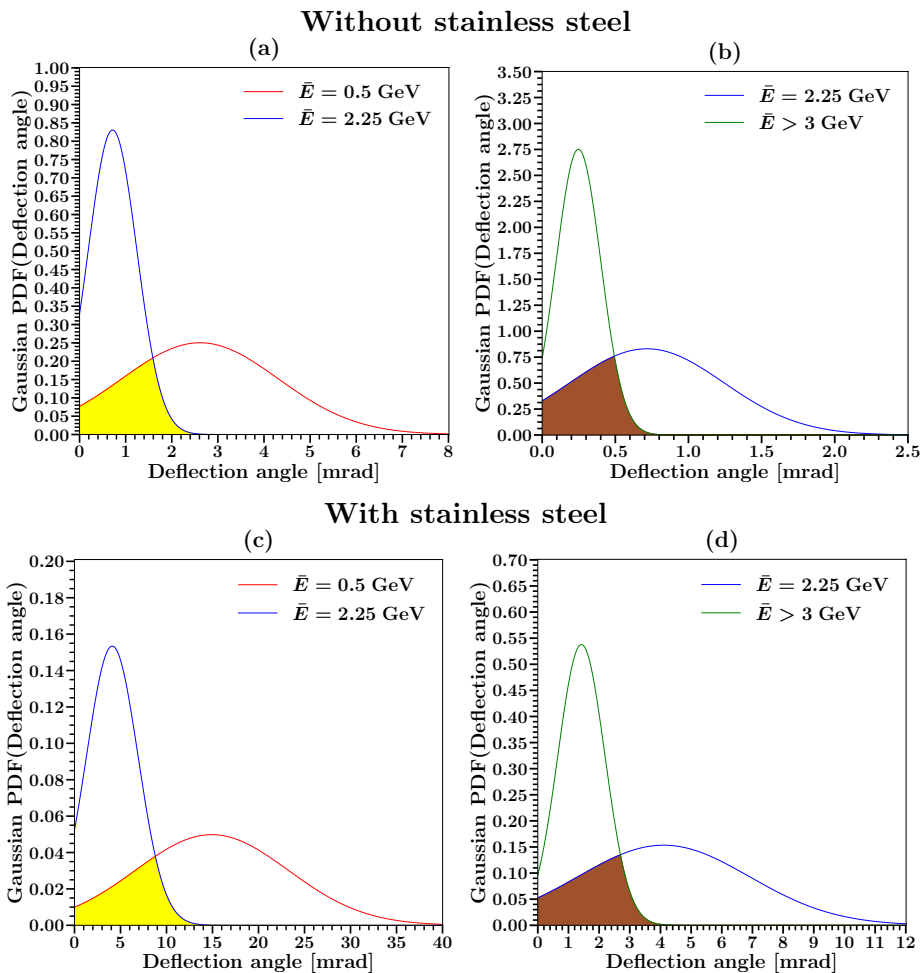


Figure 10: Contrast between the hodoscope schemes (a)-(b) without stainless steel layers and (c)-(d) with stainless steel layers over a three-group energy classification by means of positively defined modified Gaussian distributions.

In the long run, the misclassification probabilities calculated by means of these methodologies are listed in Table 4, and it is numerically exhibited that the proposed hodoscope scheme with stainless steel layers leads to the remarkably lower misclassification probabilities in comparison with the present tomographic setup without stainless steel layers.

Table 4: Misclassification probabilities for the cases without stainless steel layers and with stainless steel layers, respectively.

Without stainless steel				
\bar{E} pairs [GeV]	$\bar{\theta}_{\frac{\text{Top}+\text{Bottom}}{2}} \pm \delta\theta$ pairs [mrad]	OVL	P_{Gaussian}	P_{Linear}
0.5 - 2.25	2.612±1.700 - 0.716±0.526	0.278	0.161	0.080
2.25 - > 3	0.716±0.526 - 0.248±0.153	0.330	0.197	0.180
With stainless steel				
\bar{E} pairs [GeV]	$\bar{\theta}_{\frac{\text{Top}+\text{Bottom}}{2}} \pm \delta\theta$ pairs [mrad]	OVL	P_{Gaussian}	P_{Linear}
0.5 - 2.25	14.925±8.310 - 4.104±2.800	0.251	0.144	0.013
2.25 - > 3	4.104±2.800 - 1.422±0.766	0.304	0.179	0.141

Part 2: Material characterization

6 Unveiling triangular correlation of angular deviation in muon scattering tomography by means of GEANT4 simulations

6.1 Introduction

In the present study, we first show that the same set of four hit locations collected from the two detector layers at every hodoscope might lead to split the scattering angle into two opposite angles by forming a triangular correlation where the scattering angle is considered an exterior angle, while the two separate angles by definition are interior angles that are not neighboring the scattering angle. In the second place, we perform a series of GEANT4 simulations [1] by changing the vertical position of the VOI made out of stainless steel within our tomographic scheme [14] consisting of three plastic scintillators manufactured of polyvinyl toluene and we demonstrate that the interior opposite angles vary depending on the VOI location, whereas the scattering angle that is expressed according to the regular definition does not yield a significant difference despite this spatial change. Last but not least, the triangular correlation between the scattering angle and the interior opposite angles is corroborated by the equality between the scattering angle and the sum of these non-adjacent angles via our GEANT4 simulations. The current study is organized as follows. In section 6.2, we define the scattering angle as well as the interior separate angles in accordance with the triangular correlation by delineating over our tomographic configuration, and section 6.3 is composed of our simulation schemes in order to explore the position sensitivity of the scattering angle as well as the opposite interior angles obtained by splitting the scattering angle. We exhibit our simulation results in section 6.4.

6.2 Triangular correlation

To begin with, our tomographic setup is depicted in Fig. 11(a) where the scattering angle indicated by θ is determined by building a vector at each section, the components of which are obtained through the hit locations on two detector layers. The scattering angle might be split into two opposite angles by setting up a triangular correlation as illustrated in Fig. 11(b) where the exterior angle referred to the scattering angle is equal to the superposition of the two non-adjacent angles.

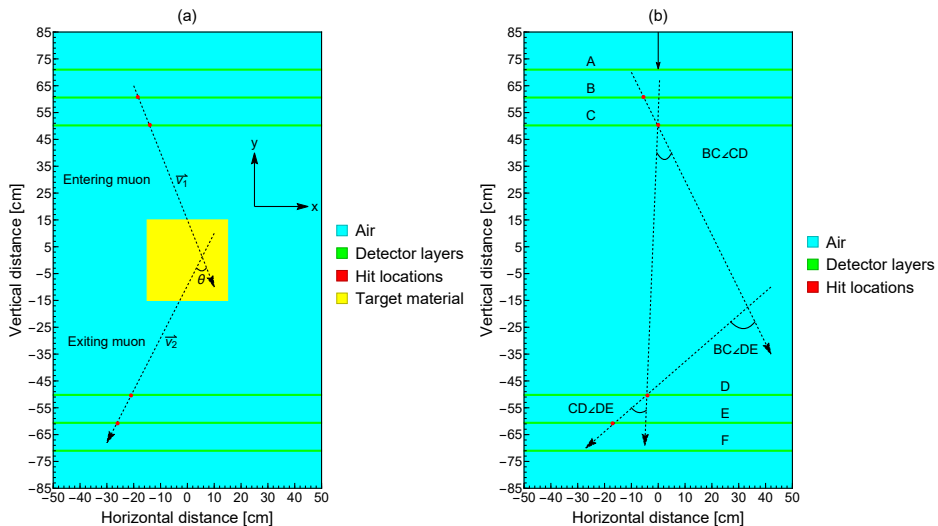


Figure 11: Delineation of angular deviation due to the target volume in our tomographic scheme: (a) scattering angle denoted by θ and (b) triangular correlation between $\theta = BC \angle DE$ and the interior angles denoted by $BC \angle CD$ and $CD \angle DE$ after splitting.

By reminding that the capital letters listed as A, B, C, D, E, and F in Fig. 11(b) point to the hit locations in the specific detector layers, the conventional scattering angle denoted by θ that also refers to the exterior angle is commonly defined as written in [75–77]

$$\theta = BC \angle DE = BC \angle CD + CD \angle DE = \arccos \left(\frac{\vec{BC} \cdot \vec{DE}}{|\vec{BC}| |\vec{DE}|} \right) \quad (51)$$

The same set of four hit locations also gives access to compute two opposite interior angles as expressed in

$$BC \angle CD = \arccos \left(\frac{\vec{BC} \cdot \vec{CD}}{|\vec{BC}| |\vec{CD}|} \right) \quad (52)$$

and

$$CD \angle DE = \arccos \left(\frac{\vec{CD} \cdot \vec{DE}}{|\vec{CD}| |\vec{DE}|} \right) \quad (53)$$

It is worth mentioning that the computation of the interior angles indicated by $BC \angle CD$ and $CD \angle DE$ does not require any further data collection from the detector layers since the same set of four hit locations are already mandatory to calculate the scattering angle, and three hit points out of four are sufficient in order to determine these non-adjacent angles. The average

angular deviation of any combination, i.e. $\overline{x\angle y}$, at a given energy value is determined by averaging over N number of the non-absorbed/non-decayed muons as defined in

$$\overline{x\angle y} = \frac{1}{N} \sum_{i=1}^N (x\angle y)_i \quad (54)$$

and the standard deviation is expressed as written in

$$\delta = \sqrt{\frac{1}{P} \sum_{i=1}^P \left((\overline{x\angle y})_i - \overline{\overline{x\angle y}} \right)^2} \quad (55)$$

where P is the number of seeds. The resulting standard deviation from M independent contributions might be described as follows

$$\delta_{\text{Resulting}} = \sqrt{\sum_{i=1}^M \delta_i^2} \quad (56)$$

By recalling that the angular resolution δ_{angular} is 1 mrad, the angular resolution is always very small compared to the average scattering angle in Eq. (54) as well as the standard deviation expressed in Eq. (42), thus the resulting standard deviation in Eq. (56) is approximately equal to that in Eq. (42) in the rest of our studies since an angular resolution of 1 mrad is negligible.

6.3 Simulation scheme for vertical position sensitivity

Following the definition of the triangular correlation and the associated angles of this correlation collected based on the tracked hits from the detector layers, we perform a sequence of GEANT4 simulations in order to verify the triangular correlation as well as to testify for the position sensitivity. We define three position cases in cm that consist of origin, up, and down as delineated in Fig. 12(a)-(c) where (a) shows the case called origin and the center of the VOI is located at (0, 0), (b) demonstrates the case labeled up and the center of VOI is moved to (30, 0), and (c) depicts the case termed down and the center of VOI is situated at (-30, 0). Apart from the VOI position, the VOI material is stainless steel with a cubic volume of $30 \times 30 \times 30$ cm³.

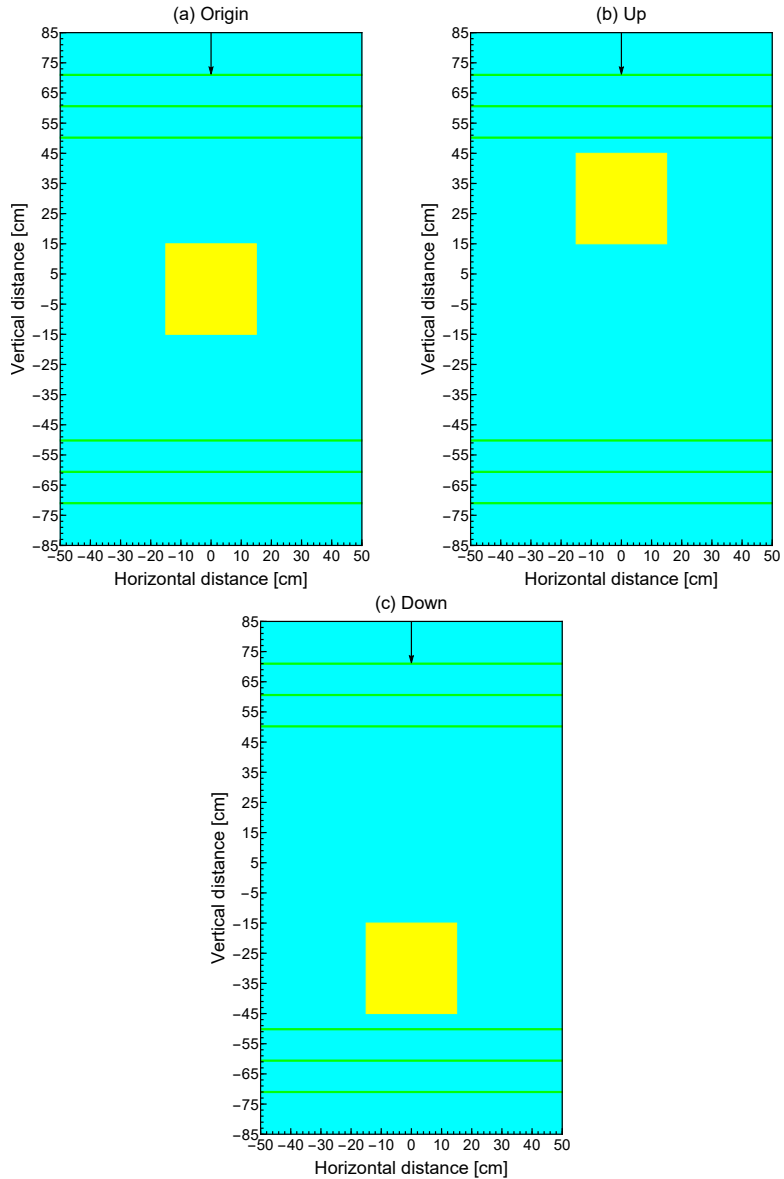


Figure 12: Simulation schemes for the position sensitivity by using three different vertical VOI centers with (a) origin at (0, 0), (b) up at (30, 0), and (c) down at (-30, 0) in cm.

To concisely summarize, our tomographic setup in GEANT4 simulations is composed of three plastic scintillators made out of polyvinyl toluene with the dimensions of $100 \times 0.4 \times 100 \text{ cm}^3$ at every section. We utilize a central mono-directional uniform muon beam as indicated by a downward black

arrow in Fig. 12(a)-(c), and the uniform energy distribution [7] lies on an interval between 0.1 and 8 GeV for the reason of more favorable numerical stability. Since the current aperture of the entire detection geometry commonly only accepts the narrow angles apart from the very rare entries around the corners, this beam setup is considered significantly reliable by reminding that the distribution of the incident angle (α) approximately corresponds to $\cos^2(\alpha)$ for an interval between $-\pi/2$ and $\pi/2$ [41]. The number of the simulated muons in each defined position is 10^5 . The tomographic components in the GEANT4 simulations are defined in agreement with the G4/NIST database, and the preferred physics list is FTFP_BERT. The simulation features are listed in Table 5.

Table 5: Simulation features.

Particle	μ^-
Beam direction	Vertical
Momentum direction	(0, -1, 0)
Source geometry	Planar
Initial position (cm)	([-0.5, 0.5], 85, [-0.5, 0.5])
Number of particles	10^5
Energy distribution	Uniform
Energy interval (GeV)	[0, 8]
Bin step length (GeV)	0.5
Energy cut-off (GeV)	0.1
Target material	Stainless steel
Target geometry	Cube
Target size (cm)	30
Material database	G4/NIST
Reference physics list	FTFP_BERT

The muon tracking is accomplished by G4Step (see Appendix A), and the tracked hit locations are post-processed by the support of a Python script (see Appendix B) where the scattering angle and the interior non-adjacent angles are initially computed for every single non-absorbed/non-decayed muon, then the uniform energy spectrum limited by 0.1 and 8 GeV is divided into 16 bins by marching with a step of 0.5 GeV, and each obtained energy bin is labeled with the central point in the energy sub-interval. Finally, the determined angles are averaged for the associated energy bins.

6.4 Simulation outcomes

Initially, we check the variation of the scattering angle with respect to five seed numbers in order to see if there is a significant fluctuation as illustrated

in Fig. 13, and we observe that the average BC \angle DE is not significantly affected by different seed numbers.

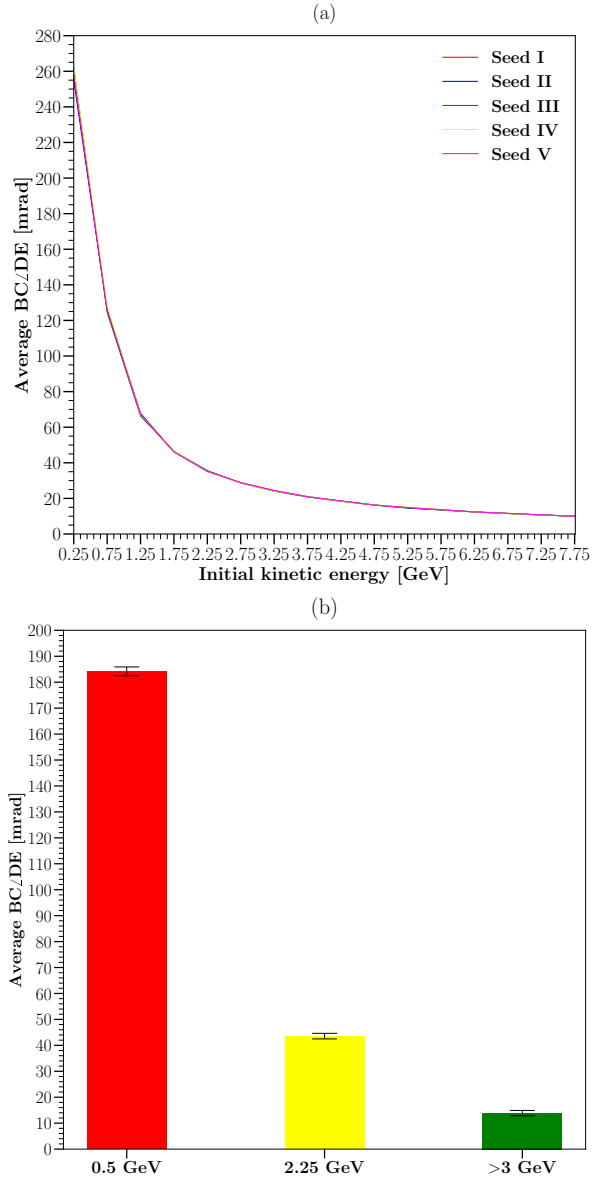


Figure 13: Average BC \angle DE via five seed numbers (a) over the energy interval between 0.1 and 8 GeV and (b) over a three-group energy structure in accordance with Eqs. (55) and (56) by including the angular resolution of 1 mrad.

We furthermore check the variation of the average scattering angle as well as the standard deviation defined in Eq. (42) with respect to the number of particles and we show that these two parameters do not vary significantly when the number of particles is increased as shown in Fig. 14.

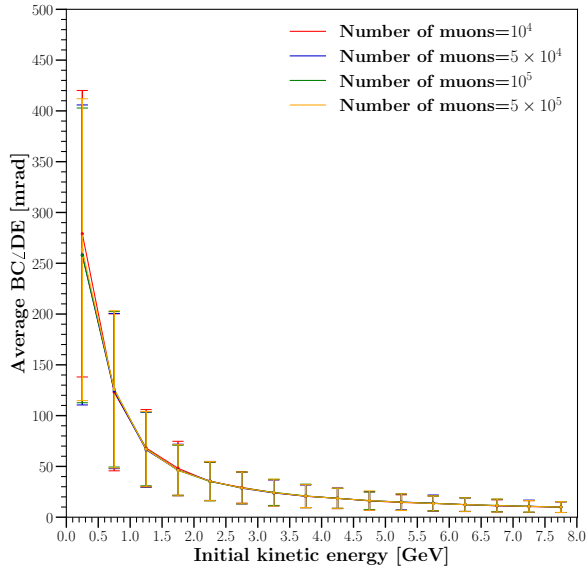


Figure 14: Average BC∠DE and the corresponding standard deviation as defined in Eq. (42) by using four different number of particles.

We continue our simulations with the scattering angle denoted by BC∠DE in order to investigate its position sensitivity versus the vertical displacement, and Fig. 15(a) shows the average BC∠DE as a function of the kinetic energy. We observe that the average BC∠DE does not exhibit a tendency to vary with the vertical position change as demonstrated in Fig. 15(a).

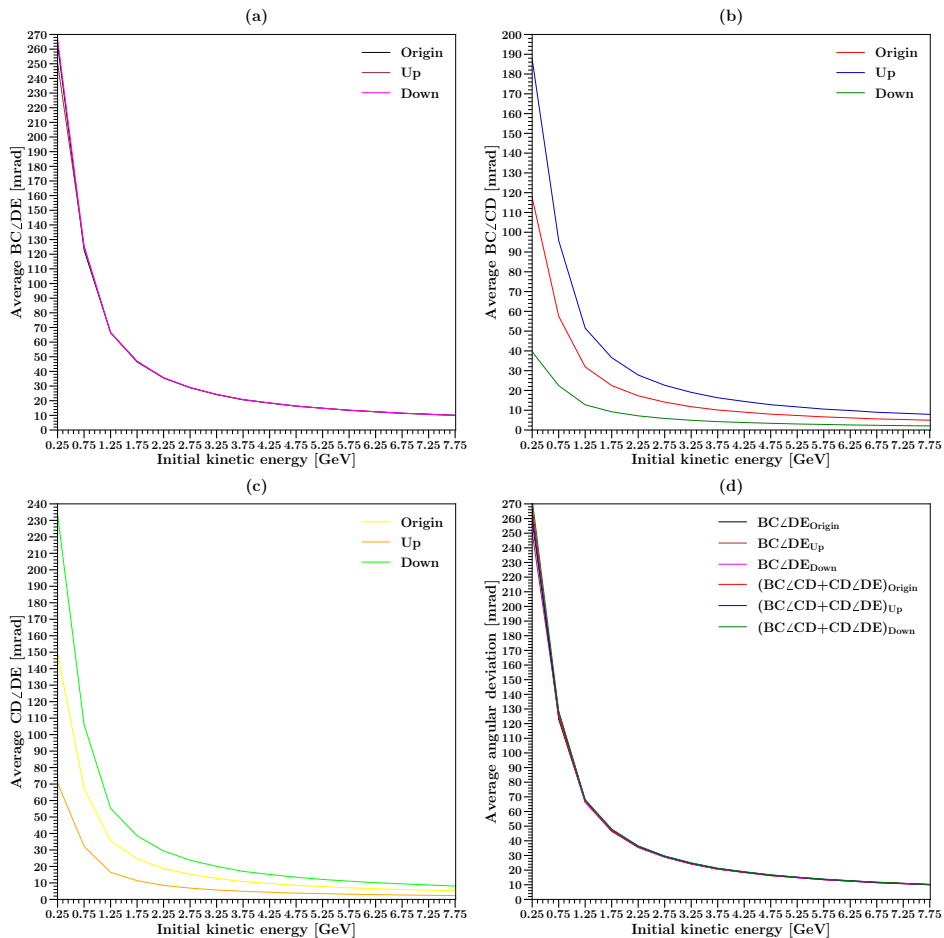


Figure 15: Comparison between the average angular deviations over (a) $BC\angle DE$, (b) $BC\angle CD$, (c) $CD\angle DE$, and (d) sum of $BC\angle CD$ and $CD\angle DE$ for three different positions.

Whereas the average $BC\angle DE$ remains almost constant in spite of the spatial variation, the average interior non-adjacent angles indicated by $BC\angle CD$ and $CD\angle DE$ yield three distinct curves in the three different vertical positions as shown in Fig. 15(b) and (c). Another reflection that we notice from Fig. 15(b) and (c) is the opposite numerical trend among the opposite interior angles, which means that the average $BC\angle CD$ increases in terms of the vertical boost, while $CD\angle DE$ augments by the downward drop. At long last, we verify the triangular correlation as defined in Eq. (51), and Fig. 15(d) ratifies the equality between the scattering angle and the superposition of the interior non-adjacent angles through our GEANT4 simulations over three different positions.

7 Applying triangular correlation of angular deviation for multi-block materials via GEANT4 simulations

7.1 Introduction

In another study [81], we already show that the scattering angle might be split into two interior angles, and these interior angles vary depending on the position of the VOI although the scattering angle almost remains as the same. In this study, we apply the triangular correlation on a three-block material configuration that consists of concrete, stainless steel, and uranium in order to check whether the triangular correlation holds. We perform a number of GEANT4 simulations [1] by changing the material order within our tomographic scheme [14] consisting of three plastic scintillators manufactured of polyvinyl toluene and we demonstrate that the triangular correlation is conserved for the multi-block material systems. The current study is organized as follows. Section 7.2 is composed of our simulation schemes in order to explore the triangular correlation as well as the material order, while we show our simulation results in section 7.3.

7.2 Simulation properties

Following the definition of the triangular correlation and the associated angles of this correlation collected based on the tracked hits from the detector layers, we perform a series of GEANT4 simulations in order to verify the triangular correlation. Since we have three different blocks, we define six combinations that consist of concrete+stainless steel+uranium (case I), concrete+uranium+stainless steel (case II), stainless steel+concrete+uranium (case III), stainless steel+uranium+concrete (case IV), uranium+concrete+stainless steel (case V), and uranium+stainless steel+concrete (case VI) according to Fig. 16 . Apart from the material order, each block is a cubic volume with the dimensions of $20 \times 20 \times 20 \text{ cm}^3$.

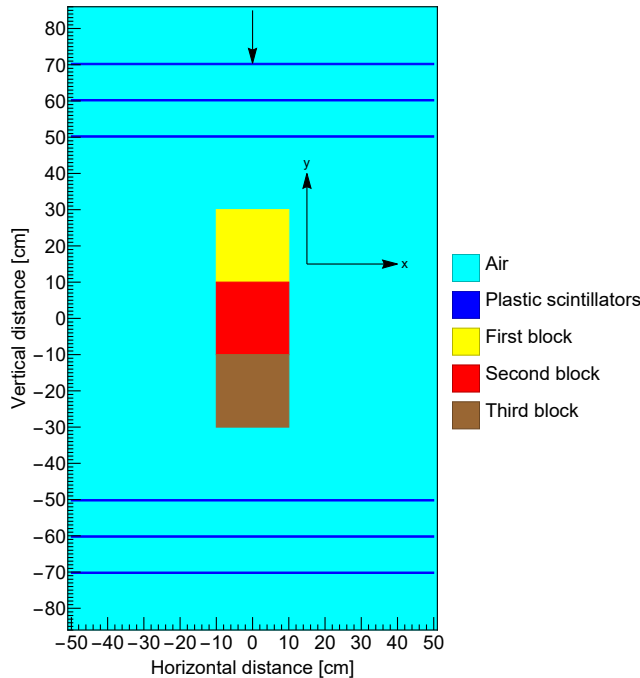


Figure 16: Simulation setup for the multi-block material configuration that consists of concrete, stainless steel, and uranium.

To briefly summarize, our tomographic setup in GEANT4 simulations is composed of three plastic scintillators made out of polyvinyl toluene with the dimensions of $100 \times 0.4 \times 100 \text{ cm}^3$ at every section. We utilize a central mono-directional uniform muon beam as indicated by a downward black arrow in Fig. 16, and the uniform energy distribution [7] lies on an interval between 0.1 and 8 GeV for the reason of more favorable numerical stability. Since the current aperture of the entire detection geometry commonly only accepts the narrow angles apart from the very rare entries around the corners, this beam setup is considered significantly reliable by reminding that the distribution of the incident angle (α) approximately corresponds to $\cos^2(\alpha)$ for an interval between $-\pi/2$ and $\pi/2$ [41]. The number of the simulated muons in each defined position is 10^5 . The tomographic components in the GEANT4 simulations are defined in agreement with the G4/NIST database, and the preferred physics list is FTFP_BERT. The simulation features are listed in Table 6.

Table 6: Simulation properties.

Particle	μ^-
Beam direction	Vertical
Momentum direction	(0, -1, 0)
Source geometry	Planar
Initial position (cm)	([-0.5, 0.5], 85, [-0.5, 0.5])
Number of particles	10^5
Energy interval (GeV)	[0, 8]
Energy cut-off (GeV)	0.1
Bin step length (GeV)	0.5
Energy distribution	Uniform
Material database	G4/NIST
Reference physics list	FTFP_BERT

The muon tracking is accomplished by G4Step, and the tracked hit locations are post-processed by the support of a Python script where the scattering angle and the interior non-adjacent angles are initially computed for every single non-absorbed/non-decayed muon, then the uniform energy spectrum limited by 0.1 and 8 GeV is divided into 16 bins by marching with a step of 0.5 GeV, and each obtained energy bin is labeled with the central point in the energy sub-interval. Finally, the determined angles are averaged for the associated energy bins.

7.3 Simulation outcomes

We first investigate the average BC \angle DE as shown in Fig. 17(a). For the average BC \angle DE, we show that the angular values converge in the high energy bins. According to Figs. 17(b) and (c), this convergence is not observed for the average BC \angle CD as well as the average CD \angle DE. Moreover, the average BC \angle CD and the average CD \angle DE result in more distinct curves compared to the average BC \angle DE, thereby implying an opportunity to coarsely predict the material order in the multi-block material systems. Finally in Fig. 17(d), by summing up the average BC \angle CD and the average CD \angle DE, we demonstrate that Eq. (51) holds for the multi-block materials.

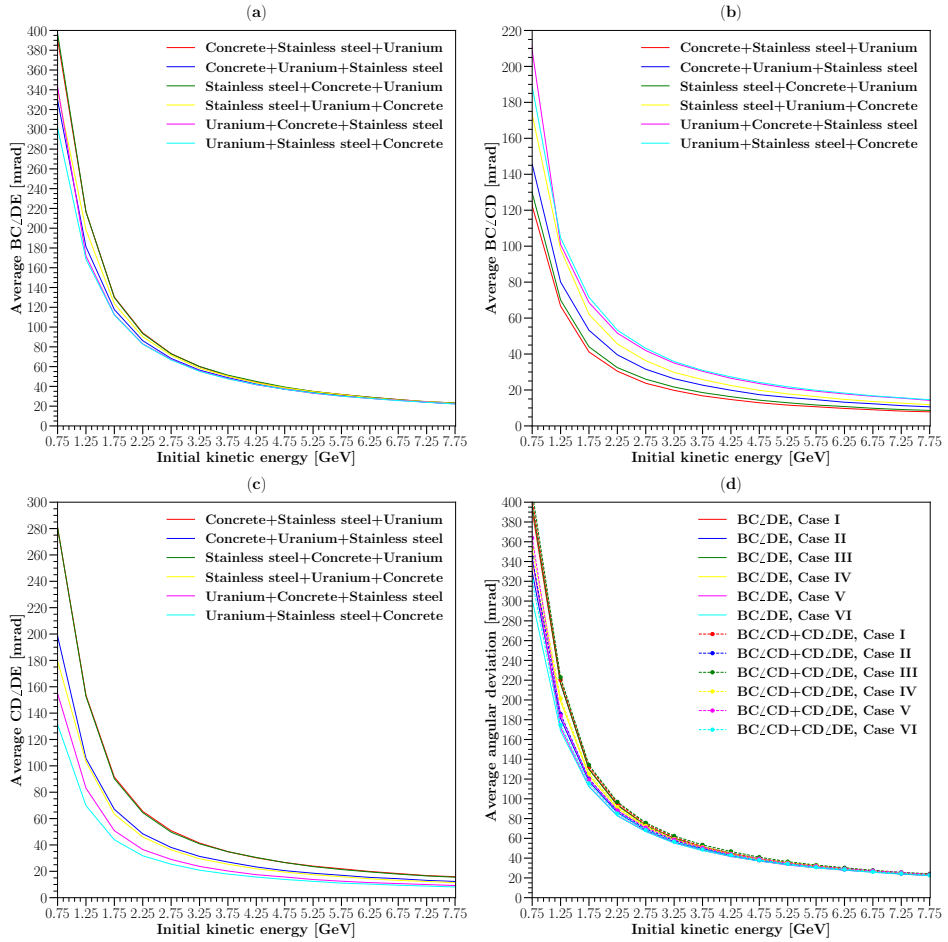


Figure 17: Simulation outcomes for the multi-block material system that consists of concrete, stainless steel, and uranium.

8 Non-destructive interrogation of nuclear waste barrels through muon tomography: A Monte Carlo study based on dual-parameter analysis via GEANT4 simulations

8.1 Introduction

In this study, we computationally explore the nuclear waste drums containing a certain amount of bulky radioactive volume [13] by aiming at revealing the quantitative information via the dual combination of the muon scattering angle and the muon absorption. We employ the Monte Carlo simulations by using the GEANT4 code [1] over our tomographic system [14] that consists of three plastic scintillators made out of polyvinyl toluene with a thickness of 0.4 cm as well as an accuracy of 1 mrad in both the top section and the bottom section [12, 13] and we follow an experimentally repeatable procedure founded on the hit locations in the detector layers. This study is organized as follows. In section 8.2, we express the characteristic parameters, i.e. the scattering angle and the relative absorption rate, for the discrimination of the nuclear waste barrels including different types of nuclear materials. While we present the hodoscope layout as well as the simulation properties in section 8.3, the simulations results are exhibited by using both quantitative and qualitative formats in section 8.4.

8.2 Definition of characteristic parameters

8.2.1 Average scattering angle and standard deviation

In the current study, the scattering angle of a muon means the three-dimensional positive angular difference between the direction of the entering muon through the VOI and the direction of the same exiting muon from the same VOI, and this angular aberration is caused by the interactions that stochastically occur between the propagating muons and the VOI. As described in Fig. 11 (a), the computation of the scattering angle requires the construction of two independent vectors by utilizing exactly four muon hit locations in the detector layers where the first vector is the difference between the hits locations in the second top detector layer and the third top detector layer, while the subtraction of the hit position in the first bottom plastic scintillator from the hit position in the second bottom plastic scintillator yields the latter vector.

The definition of these two vectors brings forth the scattering angle denoted by θ , and the scattering angle of a muon crossing the VOI is obtained by using these two vectors as defined in Eq. (40). Since a substantial number of muons reach the VOI, the average profile of the scattering angle at

a certain energy is quantified by averaging the previously determined scattering angles over N number of the non-absorbed/non-decayed muons as written in Eq. (41) where its standard deviation is given in Eq. (42).

8.2.2 Relative absorption rate

In the course of the muon penetration through the VOI, its kinetic energy is deducted by multiple mechanisms [82], and this collective slowing-down is implicitly contingent on the intrinsic properties of the VOI as well as the thickness of the VOI. Especially in the case of the relatively low-energetic muons, the energy loss due to the VOI might lead to either the zero-energy value or the quasi-zero-energy level that commonly results in the capture of the corresponding muon at rest. In the GEANT4 nomenclature for a negative muon denoted by μ^- , this process is entitled "muMinusCaptureAtRest", and it might strategically support the material characterization under certain circumstances. Hence, in the present study, we also track the number of the μ^- captures at rest within the VOI and we define a relative ratio called relative absorption rate (RAR) between the absorbed muons and the generated muons as expressed in

$$\text{RAR} = \frac{\text{Absorption}}{\text{Generation}} = \frac{\# \text{ of muMinusCaptureAtRest}}{\# \text{ of } \mu^-} \quad (57)$$

Besides the material properties, since the muon absorption is also dependent on the muon energy spectrum regarding the energy cut-off and the population size of the potentially absorbable muons, the absorption rate in Eq. (57) is axiomatically relative.

Even in the case of a fair energy cut-off, the non-absorbed muons leaving the VOI might be still subject to the capture at rest in either the surrounding medium or the bottom detector layers in accordance with their final energies, thus we further track the absorption events that occur outside the VOI.

8.3 Hodoscope scheme and simulation properties

Heretofore, we have briefly described the dual-parametric approach based on the muon scattering angle and the muon absorption. To perform the aforementioned analysis, the geometrical scheme is depicted in Fig. 18, and it is shown that the plastic scintillators are separated by a distance of 10 cm, whereas the distance between these two hodoscope sections is 100 cm. Furthermore, the dimensions of the detector layers are $100 \times 0.4 \times 100 \text{ cm}^3$. Concerning the nuclear waste drum, the VOI is held at the center of the tomographic system. Regarding the components of the nuclear waste barrel, the outermost layer is defined as a cylinder manufactured from stainless steel

layer, the height of which is 96 cm, and the thickness of which is 3.2 cm. The filling material is the cylindrical ordinary concrete slab with the height of 88 cm as well as the radius of 26.2 cm, while the nuclear material placed at the middle of the concrete padding is a cubic solid box of $20 \times 20 \times 20 \text{ cm}^3$.

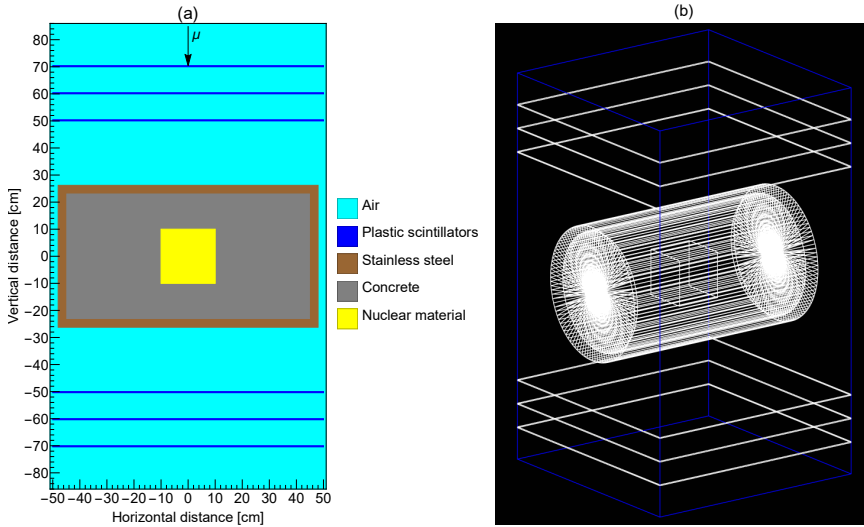


Figure 18: Illustration of simulation components (a) layout of the nuclear waste barrel within the tomographic system and (b) reproduced geometry in GEANT4.

By fulfilling the geometrical properties of the tomographic setup as well as the regular nuclear waste drum, we conduct the Monte Carlo simulations via the GEANT4 code in order to register the hit positions in the plastic scintillators. The simulation parameters are listed in Table 7, and the dimension of the simulation box is $100 \times 170 \times 100 \text{ cm}^3$ where the Cartesian components are situated symmetrically in the interval of $(-50 \text{ cm}, 50 \text{ cm})$, $(-85 \text{ cm}, 85 \text{ cm})$, and $(-50 \text{ cm}, 50 \text{ cm})$, respectively as indicated in Fig. 18(a). Into the bargain, we exhibit the reproduced geometry in GEANT4 as displayed in Fig. 18(b). We use a narrow planar multi-energetic mono-directional beam that is generated at $([-0.5, 0.5] \text{ cm}, 85 \text{ cm}, [-0.5, 0.5] \text{ cm})$ via G4ParticleGun, and the generated muons are propagating in the vertically downward direction as shown by the black arrow in Fig. 18(a), i.e. from the top edge of the simulation box through the bottom edge.

Table 7: Simulation properties.

Particle	μ^-
Beam direction	Vertical
Momentum direction	(0, -1, 0)
Source geometry	Planar
Initial position (cm)	([-0.5, 0.5], 85, [-0.5, 0.5])
Number of particles	10^5
Energy interval (GeV)	[0, 8]
Energy cut-off (GeV)	0.1
Bin step length (GeV)	0.5
Energy distribution	Uniform
Material database	G4/NIST
Reference physics list	FTFP_BERT

A uniform energy distribution lying on the interval between 0 and 8 GeV with the energy cut-off of 0.1 GeV, which is selected to minimize the probability of the muon absorption in the top detector layers as well as to maximize the encounter between the incoming muons and the VOI, is utilized by recalling the numerical advantages [7]. The total number of the generated μ^- is 10^5 in every simulation. All the materials in the simulation geometry are defined in agreement with the GEANT4/NIST material database, and FTFP_BERT is the reference physics list used in the present study.

The muon tracking is maintained by G4Step, and the registered hit locations are post-processed by the aid of a Python script where the scattering angle is first calculated for every single non-absorbed/non-decayed muon, then the uniform energy spectrum bounded by 0 and 8 GeV is partitioned into 16 bins by marching with a step of 0.5 GeV, and each obtained energy bin is labeled with the central point in the energy sub-interval. Consequently, the obtained scattering angles are averaged for the associated energy bins. In the case of the muon capture at rest, the in-target absorption is acquired by directly probing the VOI, which also means that the events called "muMinusCaptureAtRest" are recorded during the muon propagation within the VOI.

8.4 Simulation outcomes

To test the feasibility of the dual-parametric methodology by using the above-mentioned simulation setup, we select a list of nuclear materials composed of caesium, strontium, cobalt, uranium, and plutonium. Accompanying the nuclear waste barrels that contain these bulky nuclear materials, we also define an ordinary waste drum denoted by waste barrel or WB

that only consists of stainless steel and concrete for the sake of comparison. On the first basis, we first determine the scattering angle distribution (see Appendix C) by using a 1-mrad step length, and Fig. 19 depicts the distribution of the scattering angles for the nuclear waste barrels over the energy interval between 0.1 and 8 GeV.

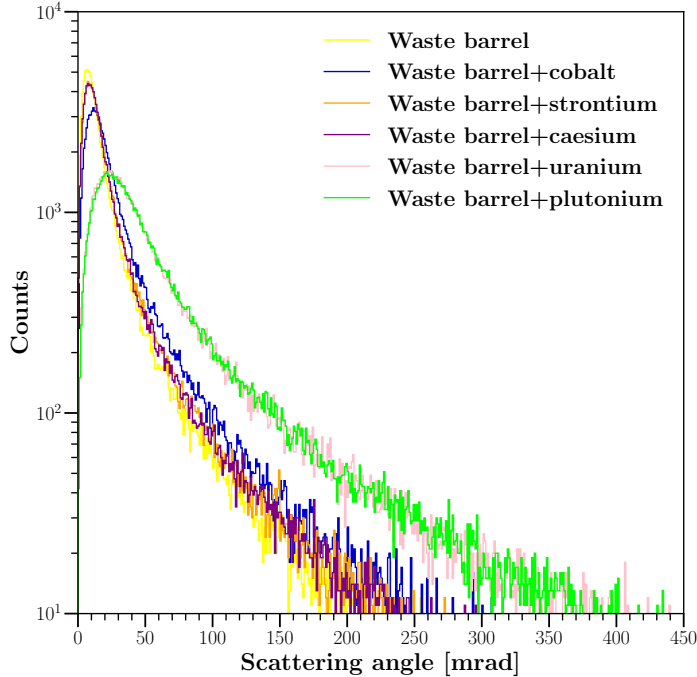


Figure 19: Distribution of the scattering angles for the nuclear waste barrels with a step length of 1 mrad over the energy interval between 0.1 and 8 GeV.

It is demonstrated that both the nuclear waste drums including strontium and caesium exhibit a close trend compared to the waste barrel, while both the nuclear waste barrels encompassing plutonium and uranium yield significantly distinct scattering angle profiles due to their high atomic numbers and the high density values in comparison with the waste barrel as well as the rest of nuclear waste barrels. Thus, regarding the practical efficiency of the material discrimination, the region around uranium along with the trans-uranium elements in the periodic table shows a remarkable advantage contrary to the other materials. It is worth mentioning that, for this specific setup that assumes the bulky radioactive volume, a nuclear waste drum containing cobalt also displays a visibly different distribution.

Whereas the distribution of the scattering angle provides a qualitative profile for the initial evaluation, we calculate the average scattering angle and the corresponding standard deviation for a set of 16 energy bins in order to obtain the quantitative details about the present nuclear waste

Table 8: Average scattering angles of the nuclear waste barrels and their corresponding standard deviations over the energy interval between 0.1 and 8 GeV.

\bar{E} [GeV]	$\bar{\theta}_{\text{WB}} \pm \delta\theta$ [mrad]	$\bar{\theta}_{\text{WB}+\text{Co}} \pm \delta\theta$ [mrad]	$\bar{\theta}_{\text{WB}+\text{Sr}} \pm \delta\theta$ [mrad]	$\bar{\theta}_{\text{WB}+\text{Cs}} \pm \delta\theta$ [mrad]	$\bar{\theta}_{\text{WB}+\text{U}} \pm \delta\theta$ [mrad]	$\bar{\theta}_{\text{WB}+\text{Pu}} \pm \delta\theta$ [mrad]
0.25	182.389±117.135	-	201.051±124.601	199.948±120.593	-	-
0.75	78.994±47.122	157.400±105.707	92.951±55.837	89.627±53.821	289.983±161.253	297.717±163.556
1.25	43.522±24.559	75.429±42.140	51.847±29.057	51.126±28.367	168.248±92.783	173.095±96.537
1.75	30.718±17.368	50.800±27.873	36.381±20.748	35.690±19.545	108.194±58.337	110.977±60.585
2.25	23.602±12.956	38.686±20.690	27.900±15.105	27.553±14.894	81.011±43.143	83.956±45.269
2.75	19.446±10.581	31.110±16.801	22.672±12.227	22.315±11.966	63.784±33.997	66.758±36.016
3.25	16.117±8.957	26.122±14.312	19.382±10.527	19.236±10.413	53.779±28.704	55.828±29.753
3.75	14.108±7.820	22.599±11.932	16.366±8.758	16.414±8.826	46.368±24.609	47.536±25.213
4.25	12.254±6.802	20.111±10.894	14.590±7.974	14.473±7.845	40.141±21.139	41.817±22.291
4.75	10.822±5.927	17.527±9.548	13.051±7.402	12.909±7.035	36.105±18.756	37.172±19.537
5.25	10.014±5.873	15.987±8.576	11.667±6.399	11.702±6.427	32.208±18.083	33.383±17.889
5.75	8.980±4.926	14.466±7.934	10.649±5.684	10.733±5.894	29.290±16.529	30.168±16.031
6.25	8.390±4.524	13.295±7.162	9.805±5.398	9.770±5.299	26.823±14.305	27.933±15.374
6.75	7.723±4.286	12.335±6.522	9.203±5.396	9.115±4.944	24.759±12.938	25.357±13.712
7.25	7.256±5.968	11.427±6.169	8.535±4.688	8.471±4.631	23.085±12.056	23.903±12.730
7.75	6.789±5.355	10.525±5.626	8.037±5.289	7.891±4.320	21.386±11.532	22.359±11.670

barrels, and Table 8 tabulates the average scattering angles and the standard deviations over the energy interval between 0.1 and 8 GeV. According to Table 8, the nuclear waste drums containing uranium or plutonium generate similar scattering angles, and the nuclear waste barrels including strontium and caesium give rise to the close scattering angles. Although it is partially hard to claim a remarkable difference between the waste barrel and the nuclear waste drums having strontium and caesium by just checking the distribution of the scattering angles in Fig. 19, Table 8 indicates a slight difference between these cases, thereby providing a challenging possibility for the material identification. By analyzing Table 8, it is also revealed that the average scattering angle declines with respect to the energy increase as shown in another study with the root-means-square values [83], and this behavior provides another qualitative format to contrast the nuclear waste barrels as illustrated in Fig. 20, and it is seen that the angular difference between the nuclear waste drums decreases when the initial kinetic energy increases.

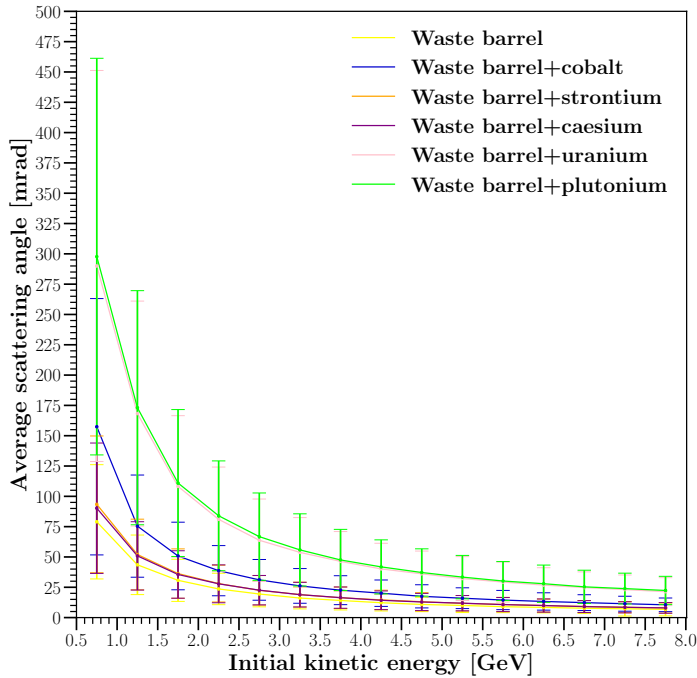


Figure 20: Variation of the average scattering angle with respect to the energy bins with a bin length of 0.5 GeV over the energy interval between 0.1 and 8 GeV by recalling the standard deviations listed in Table 8.

A similar consequence from Fig. 19 might be drawn from Fig. 20 by stating that the nuclear waste barrel with the bulky cobalt acts as a considerable deflector against the propagating muons following the uranium-

and plutonium-containing barrels; however, the deflecting capability of the nuclear waste drum with strontium or caesium is not significantly different from that of the waste barrel considering the present configuration.

The qualitative information as well as the numerical data already shows that the nuclear waste barrels might be classified according to the scattering angle that is directly dependent on the constituents in the nuclear waste barrels. As a matter of fact, Table 8 already implies the second characteristic parameter that might be utilized in order to identify the nuclear waste barrels. When the initial energy bin, which is 0.25 GeV, is examined, it is observed that the nuclear waste drums including uranium, plutonium, and cobalt do not possess any value; on the other hand, the waste barrel and also the nuclear waste drums encompassing strontium and caesium have an average scattering angle at the energy bin of 0.25 GeV. The reason behind this absence might be formulated by either the complete absorption of the penetrating muons within the energy bin of 0.25 GeV in the case of plutonium and uranium or the statistically insufficient number of the surviving muons for the energy bin of 0.25 GeV in the case of cobalt. Hence, mo-

Table 9: Number of the absorbed muons within the nuclear waste barrels by using five seed numbers over the energy interval between 0.1 and 8 GeV.

Material	Seed I	Seed II	Seed III	Seed IV	Seed V	Average	Standard deviation
WB	2820	2754	2853	2790	2825	2808.4	37.7
WB+Co	5048	4932	5178	4991	5142	5058.2	102.4
WB+Sr	2697	2628	2702	2670	2715	2682.4	34.5
WB+Cs	2397	2353	2423	2408	2445	2405.2	34.3
WB+U	7304	7206	7403	7248	7140	7314.2	91.2
WB+Pu	7508	7423	7629	7464	7620	7528.8	92.4

tivated by this certitude, we track the absorbed muons within the nuclear waste barrels by utilizing five seed numbers, and Table 9 lists the number of the muon captures at rest inside the nuclear waste barrels over the energy interval between 0.1 and 8 GeV.

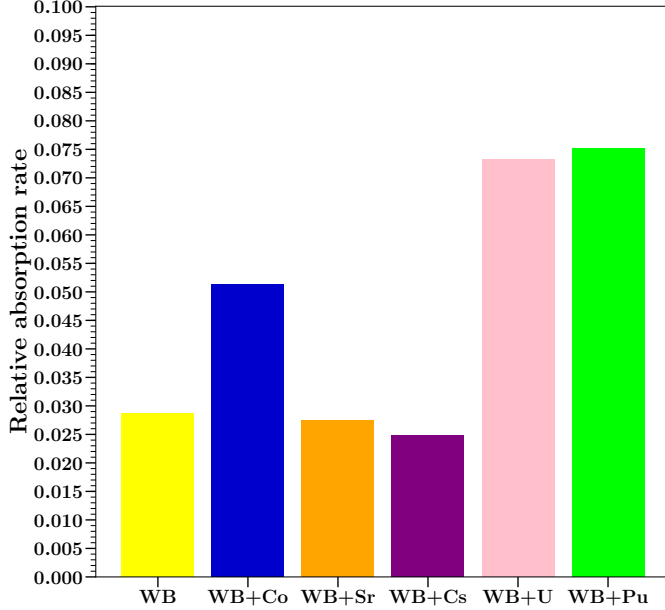


Figure 21: Relative absorption rates of the nuclear waste barrels over the energy interval between 0.1 and 8 GeV by reminding the standard deviations tabulated in Table 9.

It is explicitly demonstrated that the nuclear waste drums containing uranium or plutonium yield the highest number of the μ^- captures at rest as they generate the highest average scattering angles among the current barrels under the investigation; in contrast, the moderating power for the remaining drums except the cobalt case is almost alike. According to our observations, it is worth bearing in mind that a negligible number of muons about 21 to 40 are subject to the post-target absorption, most of which occur in the bottom detector layers in every case of the present GEANT4 simulations.

In order to compute the RAR as defined in Eq. (57), we divide the number of the μ^- captures at rest within the nuclear waste drums, i.e. the average number of the muon absorption over five seed numbers as indicated in the sixth column of Table 9, by the total number of the generated muons, which is 10^5 as stated in Table 7, and Fig. 21 presents the RAR for the current nuclear waste barrels. However, it is worth noting that a very small portion of the entire muon population usually has the absorption potential, which also means that a statistically reliable absorption dataset undoubtedly requires a long period of muon irradiation.

9 On discrimination of nuclear waste barrels subject to in-drum mixing by muon scattering tomography: A characterization study based on GEANT4 simulations

9.1 Introduction

Motivated by the feasibility verification of cosmic ray muon tomography in the discrimination of the nuclear waste/cement mixtures, we employ the GEANT4 simulations by using our tomographic setup consisting of plastic scintillators in order to determine the characteristic parameters such as the scattering angle, the muon absorption, and the muon displacement owing to the nuclear waste barrels exposed to the in-drum mixing over a set of radioactive materials consisting of cobalt, strontium, caesium, uranium, and plutonium in the present study. Upon our simulation results based on a cylindrical stainless steel drum with a radius of 29.6 cm as well as a height of 96 cm in which the nuclear materials of volume 8000 cm³ are homogeneously combined with the regular concrete, we show that the presence of uranium and plutonium in the cementitious forms is qualitatively and quantitatively visible from the characteristic parameters, while the remaining radioactive waste/cement mixtures with the nuclear sources such as cobalt, strontium, and caesium do not exhibit a significant difference in comparison with the ordinary concrete slab since the intrinsic properties of the resulting mixtures that shape the characteristic parameters are predominantly governed by the matrix properties unless the associated additives are drastically denser along with the substantially higher Z-values.

9.2 Methodology

As described in Fig. 11(a), the calculation of the scattering angle requires the construction of two distinct vectors by using exactly four muon hit points in the detector layers where the first vector is the difference between the hits locations in the second top detector layer and the third top detector layer, while the subtraction of the hit position in the first bottom plastic scintillator from the hit position in the second bottom plastic scintillator yields the second vector.

The definition of these two vectors yields the scattering angle indicated by θ , and the scattering angle of a muon crossing the VOI is determined by Eq. (40). Since a serious number of muons reach the VOI, the mean profile of the scattering angle at a certain energy is quantified by averaging the previously computed scattering angles over N number of the non-absorbed/non-decayed muons as written in Eq. (41) where its standard deviation is Eq. (42).

We also track the number of the μ^- captures at rest within the VOI and we express a relative ratio called relative absorption rate (RAR) between the absorbed muons and the generated muons as defined in Eq. (57). The displacement based on the spatial coordinates x and z over the hit locations on A and B is expressed as follows

$$\Delta = \Delta(x, z) = \sqrt{(x_B - x_A)^2 + (z_B - z_A)^2} \quad (58)$$

Since a substantial number of muons reach the VOI, the average displacement at a certain energy is quantified by averaging the previously determined displacements over N number of the non-absorbed/non-decayed muons as written in

$$\bar{\Delta} = \frac{1}{N} \sum_{i=1}^N \Delta_i \quad (59)$$

where its standard deviation is

$$\delta\Delta = \sqrt{\frac{1}{N} \sum_{i=1}^N (\Delta_i - \bar{\Delta})^2} \quad (60)$$

9.3 Simulation properties

We assume that a certain amount of nuclear waste is mixed with the regular cement within the stainless drum as illustrated in Fig. 22. This process is called in-drum mixing, and we use a volume of $20 \times 20 \times 20 \text{ cm}^3$ for a list of nuclear materials consisting of cobalt, strontium, caesium, uranium, and plutonium besides a regular waste barrel (WB) that does not contain any nuclear waste.

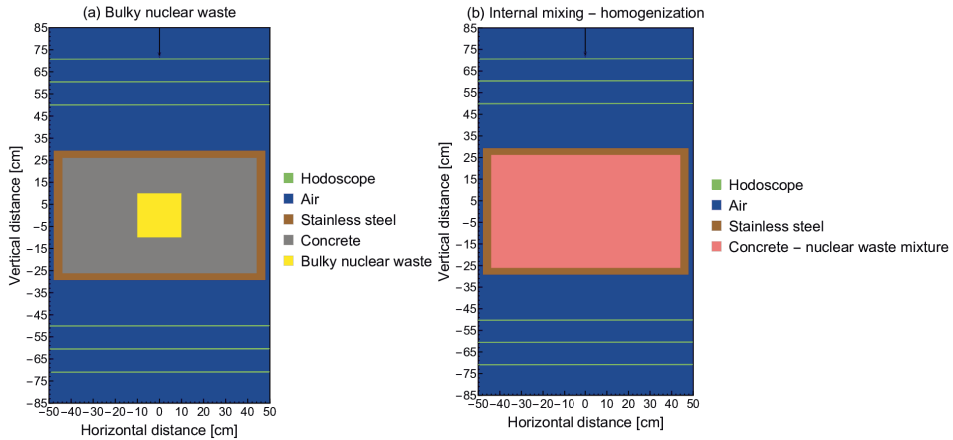


Figure 22: Scheme of the homogenized nuclear waste barrel in which the concrete and the radioactive waste are mixed.

By satisfying the geometrical properties of the tomographic configuration as well as the homogenized nuclear waste barrel, we perform the Monte Carlo simulations via the GEANT4 code in order to register the hit positions in the plastic scintillators. The simulation parameters are listed in Table 10, and the dimension of the simulation box is $100 \times 170 \times 100 \text{ cm}^3$ where the Cartesian components are positioned symmetrically in the interval of $(-50 \text{ cm}, 50 \text{ cm})$, $(-85 \text{ cm}, 85 \text{ cm})$, and $(-50 \text{ cm}, 50 \text{ cm})$ as indicated in Fig. 22.

Table 10: Simulation properties.

Particle	μ^-
Beam direction	Vertical
Momentum direction	(0, -1, 0)
Source geometry	Planar
Initial position (cm)	([-0.5, 0.5], 85, [-0.5, 0.5])
Number of particles	10^5
Energy interval (GeV)	[0, 8]
Energy cut-off (GeV)	0.1
Bin step length (GeV)	0.5
Energy distribution	Uniform
Material database	G4/NIST
Reference physics list	FTFP_BERT

A uniform energy distribution lying on the interval between 0 and 8 GeV with the energy cut-off of 0.1 GeV, which is selected to minimize the

probability of the muon absorption in the top detector layers as well as to maximize the encounter between the incoming muons and the VOI, is utilized by recalling the numerical advantages [7]. The total number of the generated μ^- is 10^5 in every simulation. All the materials in the simulation geometry are defined in agreement with the GEANT4/NIST material database, and FTFP_BERT is the reference physics list used in the present study. Again, a Python script is employed to process the GEANT4 outputs.

9.4 Simulation outcomes

We initially check the distribution of the scattering angles for the nuclear waste barrels subject to the in-drum mixing with a step length of 1 mrad over the energy interval between 0.1 and 8 GeV as depicted in Fig. 23. We see that, while the homogenized nuclear barrels with uranium or plutonium are distinguishable from the regular waste barrel indicated by WB, the remaining nuclear waste drums result in the similar curves compared to WB.

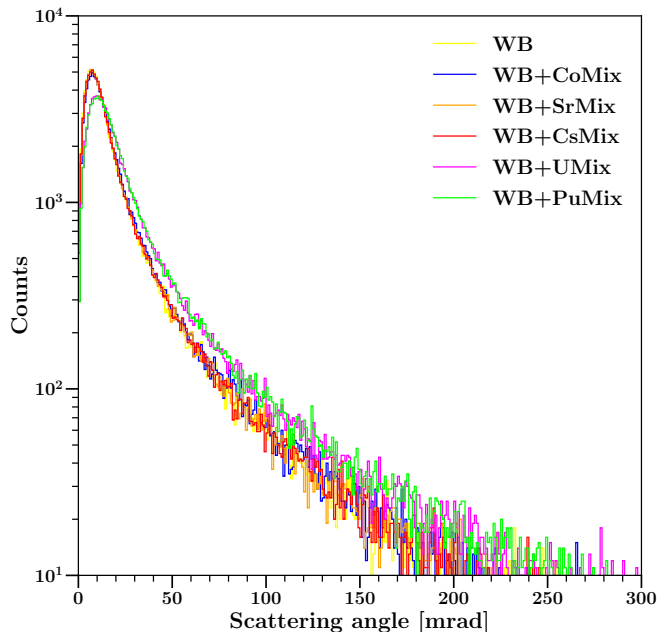


Figure 23: Distribution of the scattering angles for the nuclear waste barrels subject to in-drum mixing with a step length of 1 mrad over the energy interval between 0.1 and 8 GeV.

In order to emphasize the presence of uranium as well as plutonium, the variation of the scattering angle with respect to the same energy bins is

listed in Table 11 together with the mean scattering angle and its standard deviation.

Moreover, the variation of the average scattering angle with respect to the kinetic energy is illustrated in Fig. 24. In addition to the above-mentioned difference between WB and the waste drums containing the high-Z materials (i.e. WB+UMix and WB+PuMix), we qualitatively observe that the scattering angle declines depending on the kinetic energy.

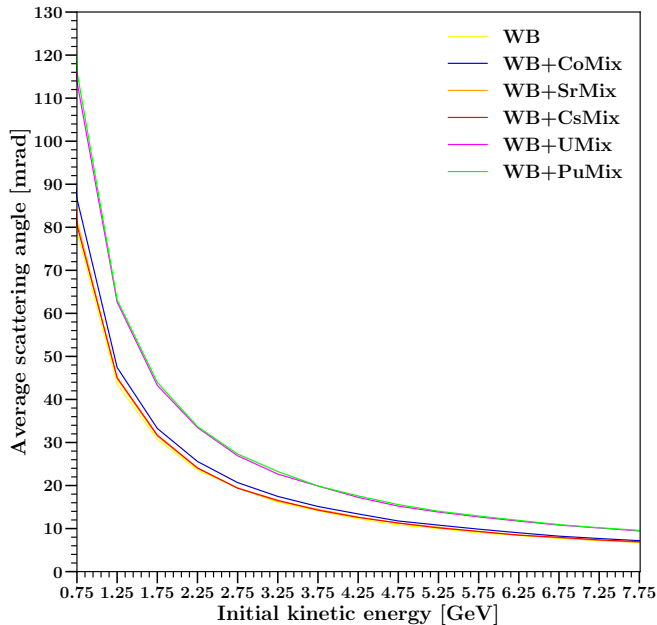


Figure 24: Variation of the average scattering angle with respect to the energy bins with a bin length of 0.5 GeV over the energy interval between 0.1 and 8 GeV.

Specific to the present study, we also determine the xz -displacement due to the homogenized nuclear waste barrels for the propagating muons, and Fig. 25 shows the distribution of the xz -displacement for the nuclear waste barrels subject to the in-drum mixing with a step length of 0.1 cm over the same energy interval, and we also observe a similar exponential trend existing in Fig. 24 in comparison with the scattering angle.

Table 11: Scattering angles of the nuclear waste barrels subject to internal mixing and their corresponding standard deviations over the energy interval between 0.1 and 8 GeV.

\bar{E} [GeV]	$\hat{\theta}_{\text{WB}} \pm \delta\theta$ [mrad]	$\hat{\theta}_{\text{WB}+\text{CoMix}} \pm \delta\theta$ [mrad]	$\hat{\theta}_{\text{WB}+\text{SiMix}} \pm \delta\theta$ [mrad]	$\hat{\theta}_{\text{WB}+\text{CsMix}} \pm \delta\theta$ [mrad]	$\hat{\theta}_{\text{WB}+\text{UMix}} \pm \delta\theta$ [mrad]	$\hat{\theta}_{\text{WB}+\text{PMix}} \pm \delta\theta$ [mrad]
0.25	182.389±117.135	197.132±124.229	184.741±119.540	182.003±116.956	244.912±143.759	244.771±138.223
0.75	78.994±47.122	86.670±53.353	81.475±49.789	80.492±48.819	113.835±69.373	116.190±70.277
1.25	43.522±24.559	47.428±27.799	44.807±25.736	45.060±25.255	62.617±34.842	63.140±35.111
1.75	30.718±17.368	33.260±18.270	31.45±17.436	31.717±17.345	43.261±23.607	43.965±23.974
2.25	23.602±12.956	25.588±13.909	23.999±13.049	24.086±13.177	33.469±18.194	33.692±18.125
2.75	19.446±10.581	20.677±11.241	19.376±10.820	19.395±10.905	26.905±14.567	27.299±14.889
3.25	16.117±8.957	17.470±9.723	16.329±9.197	16.551±8.982	22.652±12.346	23.247±13.782
3.75	14.108±7.820	15.129±8.151	14.470±7.859	14.276±7.997	19.883±10.703	19.884±10.585
4.25	12.254±6.802	13.396±8.647	12.672±6.961	12.592±6.976	17.249±9.656	17.576±9.365
4.75	10.822±5.927	11.763±6.439	11.248±6.256	11.286±6.081	15.210±8.105	15.562±8.354
5.25	10.014±5.873	10.798±5.917	10.322±6.105	10.158±5.544	13.834±7.360	14.028±7.504
5.75	8.980±4.926	9.864±5.425	9.255±5.152	9.343±5.310	12.711±6.802	12.918±6.877
6.25	8.390±4.524	9.020±5.037	8.508±4.576	8.462±4.557	11.720±6.401	11.900±6.338
6.75	7.723±4.286	8.234±4.499	7.835±4.327	7.966±4.358	10.807±5.895	10.915±5.843
7.25	7.256±5.968	7.689±4.200	7.258±3.983	7.382±4.043	10.135±5.366	10.195±5.750
7.75	6.789±5.355	7.193±3.918	6.814±3.741	6.945±4.045	9.436±5.181	9.583±5.121

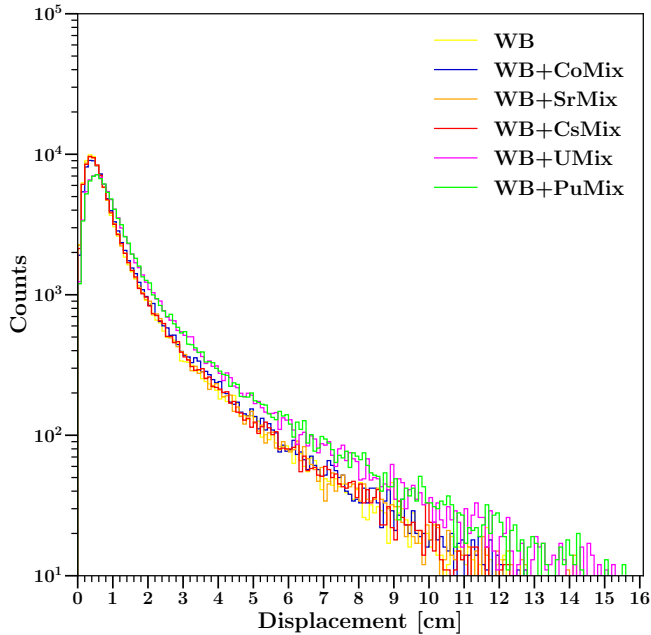


Figure 25: Distribution of the xz -displacement for the nuclear waste barrels subject to in-drum mixing with a step length of 0.1 cm over the energy interval between 0.1 and 8 GeV.

In the next step, we tabulate the variation of the scattering angle with respect to the kinetic energy for a set of 16 bins over the energy interval between 0.1 and 8 GeV in Table 12, and the nuclear waste drums including uranium or plutonium show a remarkable difference in contrast with the waste barrels that contain the nuclear materials such as cobalt, strontium, and caesium. Furthermore, we illustrate the variation of the muon displacement with respect to the kinetic energy in Fig. 26, and it is seen that the muon displacement might be used in to characterize the homogenized nuclear waste with or without uranium or plutonium.

Table 12: Displacement due to the nuclear waste barrels subject to internal mixing and their corresponding standard deviations over the energy interval between 0.1 and 8 GeV.

\bar{E} [GeV]	$\bar{\Delta}_{WB} \pm \delta\Delta$ [cm]	$\bar{\Delta}_{WB+CoMix} \pm \delta\Delta$ [cm]	$\bar{\Delta}_{WB+SrMix} \pm \delta\Delta$ [cm]	$\bar{\Delta}_{WB+CsMix} \pm \delta\Delta$ [cm]	$\bar{\Delta}_{WB+UMix} \pm \delta\Delta$ [cm]	$\bar{\Delta}_{WB+PuMix} \pm \delta\Delta$ [cm]
0.25	7.241±4.386	7.645±4.507	7.471±4.533	7.347±4.537	10.140±6.028	10.137±5.831
0.75	3.772±2.287	4.083±2.497	3.892±2.365	3.806±2.288	5.310±3.173	5.455±3.266
1.25	2.195±1.275	2.395±1.352	2.250±1.311	2.265±1.292	3.089±1.712	3.118±1.734
1.75	1.593±0.894	1.702±0.958	1.617±0.918	1.617±0.904	2.176±1.203	2.192±1.206
2.25	1.203±0.668	1.307±0.727	1.242±0.678	1.249±0.702	1.686±0.910	1.702±0.932
2.75	0.995±0.556	1.075±0.597	1.013±0.565	1.012±0.569	1.378±0.749	1.382±0.762
3.25	0.843±0.489	0.916±0.501	0.852±0.494	0.867±0.477	1.155±0.635	1.189±0.732
3.75	0.736±0.412	0.796±0.444	0.762±0.419	0.750±0.421	1.014±0.545	1.022±0.552
4.25	0.648±0.498	0.699±0.393	0.666±0.368	0.665±0.367	0.890±0.490	0.899±0.492
4.75	0.576±0.319	0.626±0.347	0.593±0.337	0.595±0.326	0.781±0.424	0.807±0.432
5.25	0.530±0.292	0.567±0.310	0.545±0.319	0.532±0.295	0.716±0.384	0.726±0.394
5.75	0.489±0.293	0.515±0.279	0.489±0.275	0.491±0.290	0.655±0.354	0.669±0.356
6.25	0.446±0.248	0.475±0.264	0.451±0.247	0.450±0.246	0.607±0.324	0.612±0.338
6.75	0.407±0.225	0.441±0.321	0.416±0.233	0.424±0.233	0.558±0.308	0.565±0.302
7.25	0.378±0.207	0.409±0.223	0.384±0.216	0.391±0.219	0.521±0.281	0.529±0.310
7.75	0.356±0.194	0.381±0.214	0.364±0.204	0.368±0.219	0.488±0.271	0.493±0.265

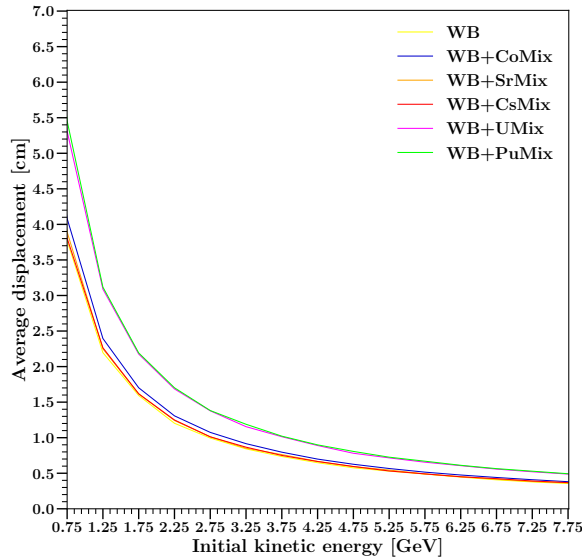


Figure 26: Variation of displacement with respect to the energy bins with a bin length of 0.5 GeV over the energy interval between 0.1 and 8 GeV.

Finally, the relative absorption rate, which is denoted by RAR, is demonstrated for the present homogenized nuclear waste barrels in Fig. 27, and we conclude that the existence of uranium and plutonium within the studied waste drums might be traceable by profiting from the absorption data.

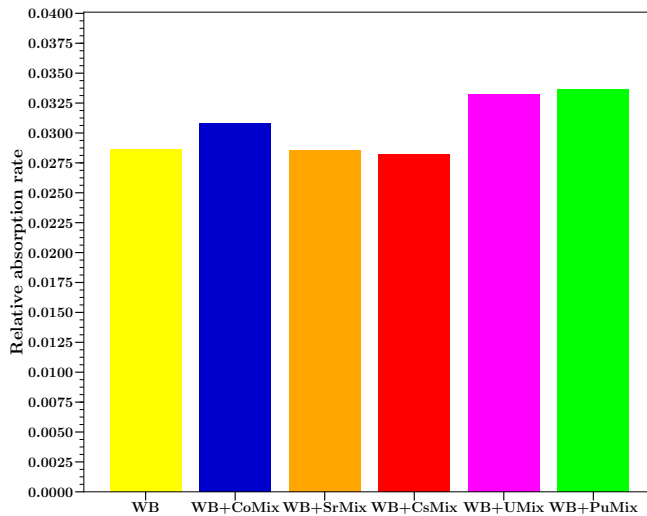


Figure 27: Relative absorption rates for the nuclear waste barrels subject to in-drum mixing over the energy interval between 0.1 and 8 GeV.

10 Energy difference between hodoscope sections in muon tomography: Application for nuclear waste barrels by means of GEANT4 simulations

10.1 Introduction

The traversing muons lose their energies [82, 84] through the volume-of-interest (VOI) in the tomographic setups based on the muon scattering [4, 10]. This energy loss is not frequently mentioned because most of the tomographic configurations do not have a custom spectrometer to track the kinetic energy of the propagating muons. However, the deflection angle through the hodoscope section might be used to roughly estimate the kinetic energy of the entering muons as described in another study [85, 86]. In this study, we explore the energy loss of the incoming muons through the VOIs over the nuclear waste barrels [12, 13, 27–30, 87] that include cobalt, caesium, strontium, uranium, and plutonium by means of the GEANT4 simulations [1]. Then, we propose a correction factor for the image reconstruction codes that coarsely group the entering muons according to the deflection angle through the hodoscope sections. The present study is organized as follows. In section 10.2, we state our methodology in order to determine the energy difference between the hodoscope sections. While we mention our simulation setup as well our simulation features in section 10.3, we exhibit our simulation outcomes in section 10.4. We suggest our correction factor for the image reconstruction codes that are founded on the deflection angle in section 10.5.

10.2 Methodology

We start with illustrating our tomographic setup that is given in Fig. 28, and the energy values are collected at the top hodoscope section above the VOI as well as the bottom hodoscope section below the VOI as indicated by the red circle and the green circle, respectively.

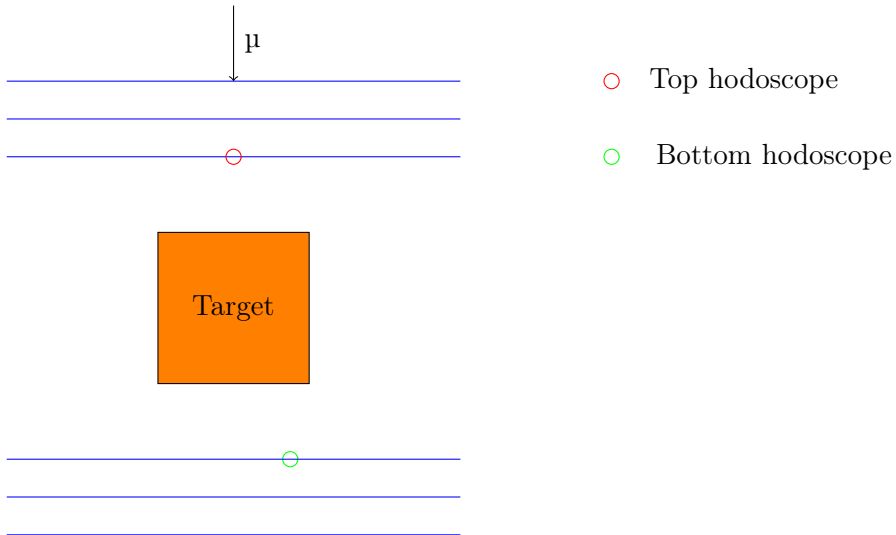


Figure 28: Tomographic setup for the collection of energy values.

The energy difference between the hodoscope sections depicted in Fig. 28 is determined by using the following expression:

$$\Delta E = E_{\text{Top}} - E_{\text{Bottom}} \quad (61)$$

where E_{Top} is the kinetic energy that is registered in the third top detector layer before the target volume, and E_{Bottom} is the kinetic energy that is tracked in the first bottom detector layer after the target volume. Since a substantial number of muons reach the VOI, the average energy difference at a certain energy bin is determined by averaging the previously determined energy differences over N number of the non-absorbed/non-decayed muons as written in

$$\overline{\Delta E} = \frac{1}{N} \sum_{i=1}^N \Delta E_i \quad (62)$$

where its standard deviation is

$$\delta \Delta E = \sqrt{\frac{1}{N} \sum_{i=1}^N (\Delta E_i - \overline{\Delta E})^2} \quad (63)$$

10.3 Simulation properties

To perform the aforementioned analysis for the nuclear waste barrels, the geometrical scheme is depicted in Fig. 18(a), and it is shown that the plastic scintillators are separated by a distance of 10 cm, whereas the distance between these two hodoscope sections is 100 cm. Furthermore, the dimensions

of the detector layers are $100 \times 0.4 \times 100 \text{ cm}^3$. Concerning the nuclear waste drum, the VOI is held at the center of the tomographic system. Regarding the components of the nuclear waste barrel, the outermost layer is defined as a cylinder manufactured from stainless steel layer, the height of which is 96 cm, and the thickness of which is 3.2 cm. The filling material is the cylindrical ordinary concrete slab with the height of 88 cm as well as the radius of 26.2 cm, while the nuclear material placed at the middle of the concrete padding is a cubic solid box of $20 \times 20 \times 20 \text{ cm}^3$.

By satisfying the geometrical properties of the tomographic setup as well as the regular nuclear waste drum, we conduct the Monte Carlo simulations via the GEANT4 code in order to register the energy values in the plastic scintillators. The simulation parameters are listed in Table 13, and the dimension of the simulation box is $100 \times 170 \times 100 \text{ cm}^3$ where the Cartesian components are situated symmetrically in the interval of (-50 cm, 50 cm), (-85 cm, 85 cm), and (-50 cm, 50 cm), respectively as indicated in Fig. 18(a). We use a narrow planar multi-energetic mono-directional beam that is generated at $([-0.5, 0.5] \text{ cm}, 85 \text{ cm}, [-0.5, 0.5] \text{ cm})$ via G4ParticleGun, and the generated muons are propagating in the vertically downward direction as shown by the black arrow in Fig. 18(a), i.e. from the top edge of the simulation box through the bottom edge.

A uniform energy distribution lying on the interval between 0 and 8 GeV with the energy cut-off of 0.1 GeV, which is selected to minimize the probability of the muon absorption in the top detector layers as well as to maximize the encounter between the incoming muons and the VOI, is utilized by recalling the numerical advantages [7]. The total number of the generated μ^- is 10^5 in every simulation. All the materials in the simulation geometry are defined in agreement with the GEANT4/NIST material database, and FTFP_BERT is the reference physics list used in the present study.

Table 13: Simulation properties.

Particle	μ^-
Beam direction	Vertical
Momentum direction	(0, -1, 0)
Source geometry	Planar
Initial position (cm)	([-0.5, 0.5], 85, [-0.5, 0.5])
Number of particles	10^5
Energy interval (GeV)	[0, 8]
Energy cut-off (GeV)	0.1
Bin step length (GeV)	0.5
Energy distribution	Uniform
Material database	G4/NIST
Reference physics list	FTFP_BERT

The muon tracking is maintained by G4Step, and the registered energy values are post-processed by the aid of a Python script where the energy difference is first calculated for every single non-absorbed/non-decayed muon, then the uniform energy spectrum bounded by 0 and 8 GeV is partitioned into 16 bins by marching with a step of 0.5 GeV, and each obtained energy bin is labeled with the central point in the energy sub-interval. Consequently, the obtained energy differences are averaged for the associated energy bins.

10.4 Simulation results

We exhibit our simulation outcomes in Table 14 and we initially show that the energy loss is a characteristic parameter that is dependent on the intrinsic properties of the VOIs. While the waste barrels containing uranium and plutonium yields the highest deposited energy, the reference barrel indicated by WB, which only includes stainless steel and concrete, leads to the lowest energy loss. According to the listed values in Table 14, the energy loss is not negligible for the first few energy bins. This also means that the scattering regime for the initial energy bins changes significantly after the VOIs, and this may necessitate a correction factor for the image reconstruction codes where the kinetic energy of the incoming muons is coarsely estimated according to the deflection angle in the top hodoscope and the bottom hodoscope since the deflection angle is contingent on the kinetic energy of the crossing muons. In order to highlight the spectral difference between two hodoscope sections, Fig. 29 shows the energy distributions at either section.

Table 14: Energy difference between hodoscope sections and their corresponding standard deviations for the nuclear waste barrels over the energy interval between 0.1 and 8 GeV.

\bar{E} [GeV]	$\Delta\bar{E}_{\text{WB}} \pm \delta\Delta E$ [GeV]	$\Delta\bar{E}_{\text{WB}+\text{C}_6} \pm \delta\Delta E$ [GeV]	$\Delta\bar{E}_{\text{WB}+\text{S}_7} \pm \delta\Delta E$ [GeV]	$\Delta\bar{E}_{\text{WB}+\text{C}_8} \pm \delta\Delta E$ [GeV]	$\Delta\bar{E}_{\text{WB}+\text{U}} \pm \delta\Delta E$ [GeV]	$\Delta\bar{E}_{\text{WB}+\text{Pu}} \pm \delta\Delta E$ [GeV]
0.75	0.291±0.018	0.470±0.021	0.283±0.018	0.261±0.017	0.648±0.026	0.664±0.026
1.25	0.307±0.029	0.495±0.034	0.300±0.028	0.276±0.028	0.678±0.039	0.695±0.039
1.75	0.317±0.040	0.516±0.050	0.310±0.043	0.286±0.038	0.713±0.057	0.731±0.061
2.25	0.325±0.050	0.530±0.062	0.317±0.050	0.292±0.050	0.739±0.076	0.755±0.077
2.75	0.330±0.064	0.541±0.077	0.323±0.058	0.299±0.057	0.758±0.099	0.776±0.092
3.25	0.335±0.076	0.550±0.092	0.331±0.074	0.304±0.073	0.774±0.116	0.793±0.113
3.75	0.341±0.095	0.558±0.108	0.333±0.076	0.308±0.088	0.787±0.134	0.805±0.127
4.25	0.342±0.085	0.564±0.118	0.337±0.105	0.311±0.095	0.800±0.160	0.819±0.175
4.75	0.345±0.106	0.571±0.128	0.342±0.119	0.314±0.091	0.810±0.174	0.833±0.176
5.25	0.349±0.112	0.575±0.142	0.342±0.118	0.316±0.107	0.813±0.183	0.835±0.193
5.75	0.354±0.133	0.579±0.155	0.347±0.118	0.320±0.123	0.824±0.202	0.850±0.231
6.25	0.353±0.126	0.584±0.169	0.347±0.123	0.321±0.144	0.831±0.218	0.855±0.223
6.75	0.354±0.132	0.591±0.186	0.352±0.165	0.321±0.130	0.840±0.255	0.867±0.265
7.25	0.360±0.155	0.593±0.193	0.356±0.183	0.326±0.150	0.849±0.295	0.865±0.256
7.75	0.359±0.147	0.598±0.221	0.357±0.175	0.330±0.162	0.851±0.278	0.879±0.293

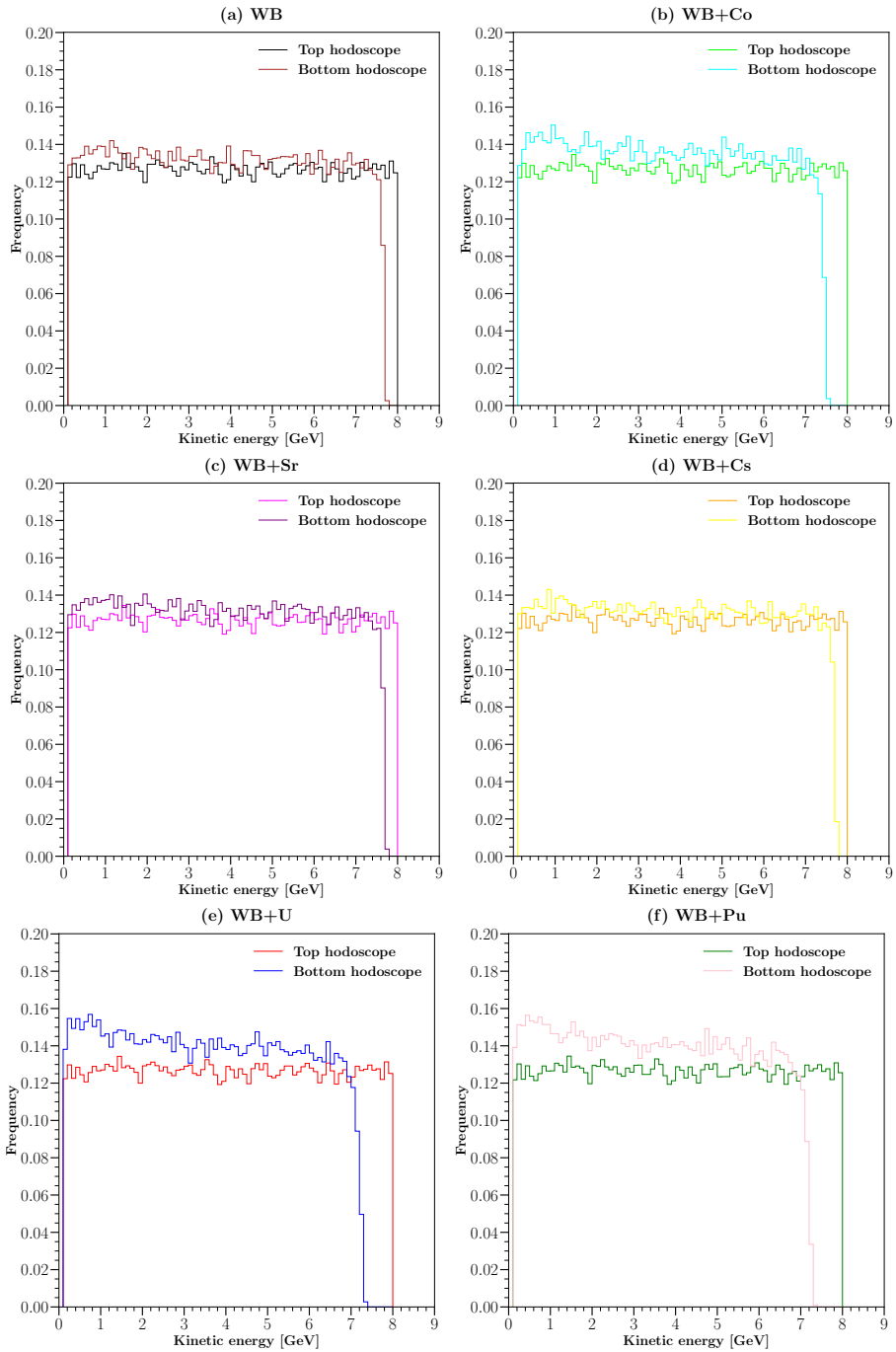


Figure 29: Spectral difference between hodoscope sections for nuclear waste barrels over the energy interval between 0.1 and 8 GeV.

10.5 Correction factor for image reconstruction

As described in another study [85, 86], the kinetic energy of the incoming muons might be estimated by using the deflection angle at the hodoscope sections. Moreover, the deflection angles obtained through these hodoscope sections are averaged in order to decrease the resulting standard deviation. According to Table 14 and Fig. 29, it is shown that the energy values of the incoming muons are different from those of the outgoing muons in the presence of the VOIs, and the deflection angle at the bottom section varies depending on the intrinsic properties of the VOIs. Thus, it is necessary to renormalize the bottom deflection angle for the image reconstruction purposes. The distribution of the deflection angle as function of momentum is described in the following expression:

$$\theta \approx \frac{13.6 \text{ MeV}}{\beta p} \sqrt{\frac{l}{X_0}} \quad (64)$$

where p is the momentum, β is the velocity, l is the thickness of the material, and X_0 is the radiation length of the material. Then, by assuming that the top hodoscope and the bottom hodoscope are completely symmetrical and made out of the same materials as shown in Figs. 18(a) and 28,

$$\frac{\theta_{\text{Top}}}{\theta_{\text{Bottom}}} \approx \frac{\frac{13.6 \text{ MeV}}{\beta_{\text{Top}} p_{\text{Top}}} \sqrt{\frac{l}{X_0}}}{\frac{13.6 \text{ MeV}}{\beta_{\text{Bottom}} p_{\text{Bottom}}} \sqrt{\frac{l}{X_0}}} = \frac{\beta_{\text{Bottom}} p_{\text{Bottom}}}{\beta_{\text{Top}} p_{\text{Top}}} \approx \frac{E_{\text{Bottom}}}{E_{\text{Top}}} \quad (65)$$

So, a correction factor for the bottom hodoscope might be formulated as

$$C = \frac{\bar{\theta}_{\text{Top}}}{\bar{\theta}_{\text{Bottom}}} \quad (66)$$

This correction factor might be useful for the image reconstruction codes where the kinetic energy of the entering muons is roughly predicted according to the deflection angle.

Part 3: Muon source optimization

11 Towards energy discretization for muon scattering tomography in GEANT4 simulations: A discrete probabilistic approach

11.1 Introduction

In the present study, by aiming at obtaining a fast, verifiable, and modifiable muon source in the GEANT4 simulations, we initially exhibit our procedure that is based on the multi-binned approximation of the CRY muon energy spectrum. In the latter instance, we incorporate our discrete spectra in the GEANT4 code by using a one-dimensional probability grid that operates under G4ParticleGun. Following this step, we furthermore gain the capability of utilizing the existing experimental spectra. Then, we test our methodology over our tomographic setup consisting of plastic scintillators fabricated from polyvinyl toluene with the dimensions of $100 \times 0.4 \times 100 \text{ cm}^3$ and we determine the characteristic parameters such the average scattering angle, the root-mean-square of the scattering angle, and the number of the muon absorption by using a set of slabs composed of aluminum, copper, iron, lead, and uranium with the dimensions of $40 \times 10 \times 40 \text{ cm}^3$. Finally, we contrast our simulation outcomes by means of both the CRY discrete spectrum and the BESS muon spectrum. This study is outlined as follows. In section 11.2, we compute the discrete probabilities for the corresponding discrete energies, and section 11.3 describes the implementation in the GEANT4 code. While we express our characteristic parameters as well as our simulation setup in section 11.4, we expose our simulation outcomes in section 11.5.

11.2 Discrete energies and discrete probabilities

At the outset, we strive for the energy discretization based on the extracted energy list from the CRY muon generator [31] between 0 and 8 GeV. To achieve this aim, we first set out our constant bin length that is selected as 0.1 GeV. Thus, the number of non-zero energy bins is evidently 80 as written in

$$\#_{\text{Bins}} = \frac{E_{\text{Max}} - E_{\text{Min}}}{L_{\text{Bins}}} = \frac{8.0 - 0}{0.1} = 80 \quad (67)$$

Then, in agreement with the energy dataset acquired through the CRY generator, the number of the counts in the specific energy bin denoted by E_i in GeV is computed by incorporating any $E_x \in (E_{i-1}, E_i]$ under the condition of $m_0 = 0$ for $E_0 = 0$ as described in

$$m_i = \sum_{k=1} 1 \text{ if } E_{i-1} < E_x \leq E_i \text{ for } i=1, 2, 3, \dots, 80 \quad (68)$$

Basically, Eq. (68) might be performed by using the existing tools in Python, e.g. NumPy. While this operation is an approximation by definition, we do not significantly neglect any fundamental information in the case of the fine energy bins as accomplished in the present study, which also implies that the simulation outcomes by means of the finely binned histogram do not yield consequential differences in comparison with the continuous energy spectra. Whereas the count numbers in the particular energy bins already provides an opportunity to employ the discrete energy distributions in the wake of renormalization, we favor to determine the discrete probabilities that serve to constitute a probability grid; hence, we first calculate the total count over 80 energy bins as shown in

$$\sum_{i=0}^{\#Bins} m_i = \sum_{i=0}^{80} m_i \quad (69)$$

In the end, the discrete probability, i.e. the discrete normalized frequency to rephrase it, at a given energy bin indicated by E_i is the ratio between the specific count in E_i and the total counts over 80 bins by satisfying the unity condition as noted in

$$p_i = \frac{m_i}{\sum_{i=0}^{80} m_i} \quad \text{with} \quad \sum_{i=0}^{80} p_i = 1 \quad (70)$$

Finally, we tabulate the discrete probabilities along with the discrete muon energies obtained via the CRY muon source in Table 15 by entitling D-CRY. As indicated in Table 15, we view that the highest discrete probability appertains to the energy bin of 0.5 GeV, i.e. the mode of our discrete energy distribution, which is reduced approximately by one order of magnitude at 8 GeV, and the trend observed in D-CRY resembles to a log-normal distribution with a positive skewness.

Table 15: D-CRY discrete probabilities between 0 and 8 GeV.

E_i [GeV]	p_i	E_i [GeV]	p_i	E_i [GeV]	p_i
0.0	0.000000	2.7	0.014713	5.4	0.006189
0.1	0.012536	2.8	0.014224	5.5	0.006348
0.2	0.025745	2.9	0.014126	5.6	0.006653
0.3	0.028020	3.0	0.012842	5.7	0.006507
0.4	0.027066	3.1	0.012610	5.8	0.005614
0.5	0.035285	3.2	0.012133	5.9	0.005895
0.6	0.028265	3.3	0.012903	6.0	0.005895
0.7	0.031579	3.4	0.012487	6.1	0.005785
0.8	0.030784	3.5	0.011962	6.2	0.005577
0.9	0.027776	3.6	0.010641	6.3	0.005504
1.0	0.025464	3.7	0.010579	6.4	0.004342
1.1	0.031506	3.8	0.009626	6.5	0.004354
1.2	0.028155	3.9	0.010384	6.6	0.004085
1.3	0.025807	4.0	0.009283	6.7	0.003645
1.4	0.023642	4.1	0.008794	6.8	0.003999
1.5	0.021709	4.2	0.008843	6.9	0.003889
1.6	0.021526	4.3	0.007938	7.0	0.003963
1.7	0.023483	4.4	0.007864	7.1	0.004317
1.8	0.021342	4.5	0.007693	7.2	0.003681
1.9	0.019691	4.6	0.007094	7.3	0.003632
2.0	0.020364	4.7	0.007363	7.4	0.003620
2.1	0.018419	4.8	0.007192	7.5	0.004109
2.2	0.017184	4.9	0.007216	7.6	0.003363
2.3	0.017001	5.0	0.006923	7.7	0.003584
2.4	0.016242	5.1	0.006433	7.8	0.003620
2.5	0.015398	5.2	0.006788	7.9	0.003486
2.6	0.015362	5.3	0.006739	8.0	0.003596

In view of the fact that we aim at carrying out a multi-group approach, we are furthermore capable of utilizing the empirical muon energy spectrum as in the case of the BESS spectrometer [39] where the discrete energies are measured at the distinct particle fluxes. We adopt the first 36 non-zero energy bins between 0.598 and 8.1 GeV and their corresponding separate fluxes by labeling as EXP-BESS, and the discrete probabilities are determined by the quotient between the particular flux value at a specific energy

and the total flux as follows

$$p_i = \frac{\phi_i}{\sum_{i=0}^{36} \phi_i} \quad \text{with} \quad \sum_{i=0}^{36} p_i = 1 \quad (71)$$

Since the energy list is already discretized, we exert neither a further approximation nor a simplifying assumption in Eq. (71). The experimental energy values obtained through the BESS spectrometer as well as the computed discrete probabilities are listed in Table 16.

Table 16: Discrete EXP-BESS probabilities between 0 and 8.1 GeV.

E_i [GeV]	p_i	E_i [GeV]	p_i
0.000	0.000000	2.290	0.025003
0.598	0.058310	2.460	0.022951
0.644	0.056910	2.650	0.021551
0.694	0.055511	2.860	0.019079
0.748	0.053645	3.080	0.017213
0.806	0.052712	3.310	0.015440
0.868	0.050379	3.570	0.014274
0.936	0.049447	3.850	0.012595
1.010	0.046648	4.140	0.011055
1.080	0.044782	4.470	0.009843
1.170	0.042449	4.810	0.008723
1.260	0.041050	5.180	0.007744
1.360	0.039790	5.580	0.006811
1.460	0.037365	6.010	0.005784
1.570	0.035126	6.480	0.005271
1.700	0.033680	6.980	0.004478
1.830	0.031347	7.520	0.003872
1.970	0.029295	8.100	0.003233
2.120	0.026636		

As can be noticed from Table 16, the EXP-BESS muon spectrum exhibits an exponentially decreasing trend where the lower bound is associated with the highest discrete probability, whereas the upper bound is identified with the minimum discrete normalized frequency. In order to qualitatively show the variation of both D-CRY and EXP-BESS, Fig. 30 displays the energy histograms where (a) indicates D-CRY in comparison with the discrete CMSCGEN data reproduced from another study [88] that is dedicated to the CMS strip tracker, while (b) points out EXP-BESS. From Fig. 30(a),

we experience that our D-CRY tends to show strong similarities when compared to the existing qualitative data of the CMSCGEN muon generator, thereby relatively authenticating our discretized energy spectrum hinged on the CRY muon generator.

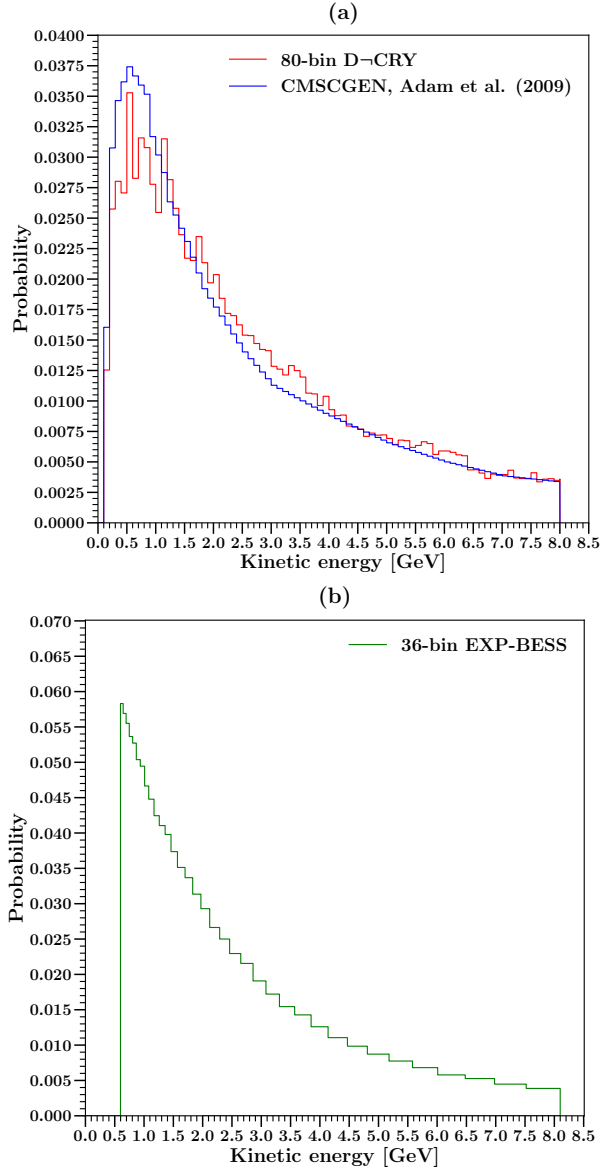


Figure 30: Comparison between discrete energy histograms (a) 80-bin D-CRY compared to CMSCGEN and (b) 36-bin EXP-BESS.

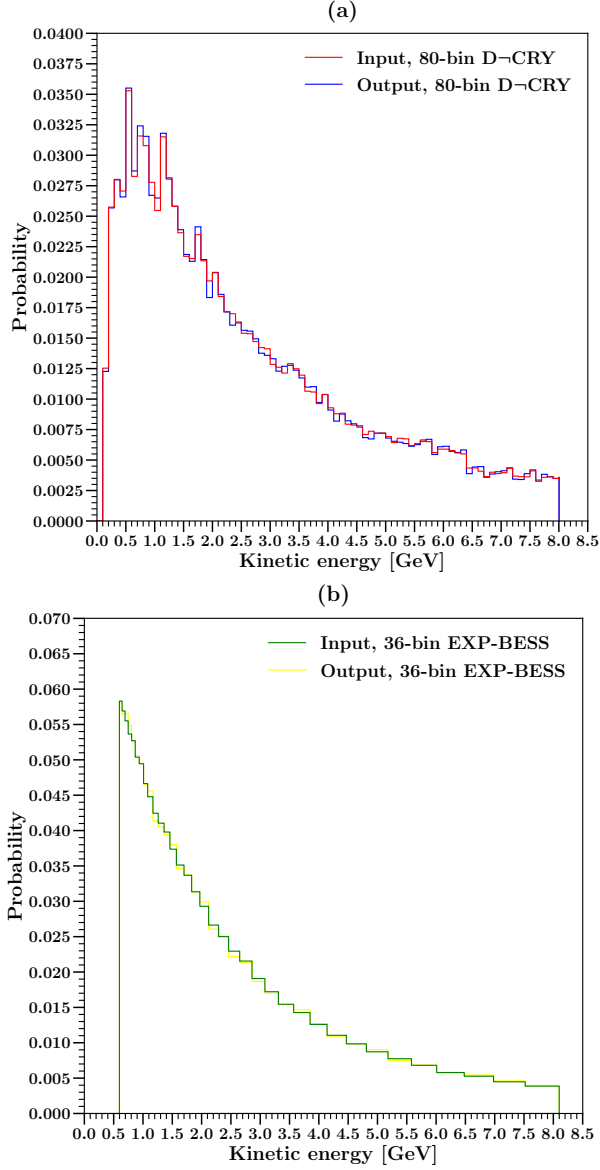


Figure 32: Contrast between the input dataset before processing with the probability grid and the output values through the activation of our probability grid (a) 80-bin D-CRY and (b) 36-bin EXP-BESS.

11.4 Characteristic parameters and simulation properties

For the purpose of appraisal, we express a number of characteristic parameters consorted with the muon tomography. By defining two vectors, we bring forth the scattering angle denoted by θ as depicted in Fig. 33, and the

scattering angle of a muon crossing the volume-of-interest (VOI) is obtained by using these two vectors as expressed in Eq. (40). The mean scattering angle due to the VOI and its standard deviation over N number of the non-absorbed/non-decayed muons are calculated as written down in Eqs. (41) and (42). Furthermore, the root-mean-square (RMS) of the scattering angle over N number of the non-absorbed/non-decayed muons is determined by using the following equation:

$$\theta_{\text{RMS}} = \sqrt{\frac{1}{N} \sum_{i=1}^N \theta_i^2} \quad (72)$$

On top of the scattering angle, we precisely register the number of the absorbed muons within the VOI as denoted in Eq. (57).

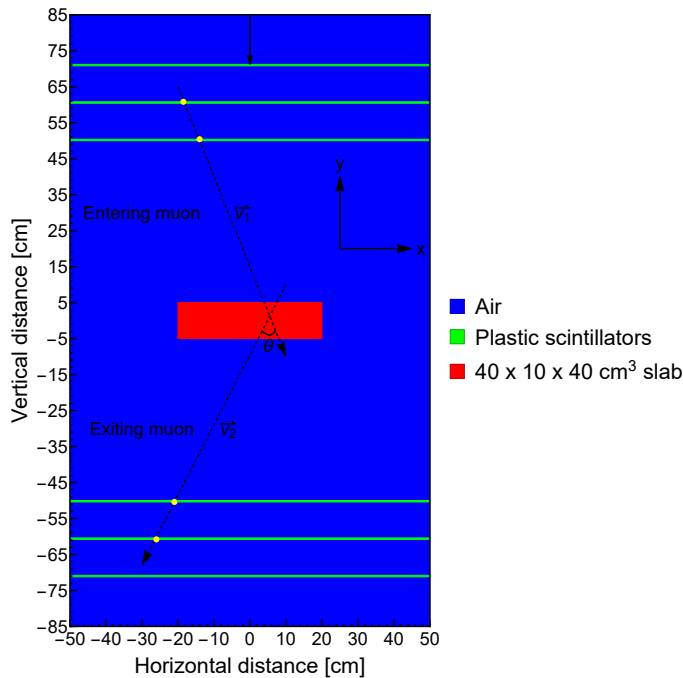


Figure 33: Delineation of scattering angle within the present tomographic configuration.

Lastly, our simulation features are tabulated in Table 17, and we conduct our GEANT4 simulations over a set of slabs including aluminum, copper, iron, lead, and uranium with the dimensions of $40 \times 10 \times 40 \text{ cm}^3$ in accordance with another study [89]. The particle tracking is managed by G4Step, and the registered hit locations on the plastic scintillators are post-processed by dint of a Python script.

Table 17: Simulation properties.

Particle	μ^-
Beam direction	Vertical
Momentum direction	(0, -1, 0)
Source geometry	Planar
Initial position (cm)	([-0.5, 0.5], 85, [-0.5, 0.5])
Particle injector	G4ParticleGun
Number of particles	10^5
Energy distribution	Non-linear discrete
Target geometry	Rectangular prism
Target volume (cm ³)	$40 \times 10 \times 40$
Material database	G4/NIST
Reference physics list	FTFP_BERT

11.5 Simulation results

In the long run, we inaugurate our GEANT4 simulations founded on our discrete approach, the initial outcomes of which are displayed in Fig. 34 in terms of the angular counts. From Fig. 34(a)-(b), we explicitly see that the angular populations characteristically vary depending on the atomic number as well as the material density for the same thickness. Moreover, 80-bin D-CRY yields a typical exponential decrease towards the higher angles, whereas this trend appears to be a parabolic reduction in the case of 36-bin EXP-BESS.

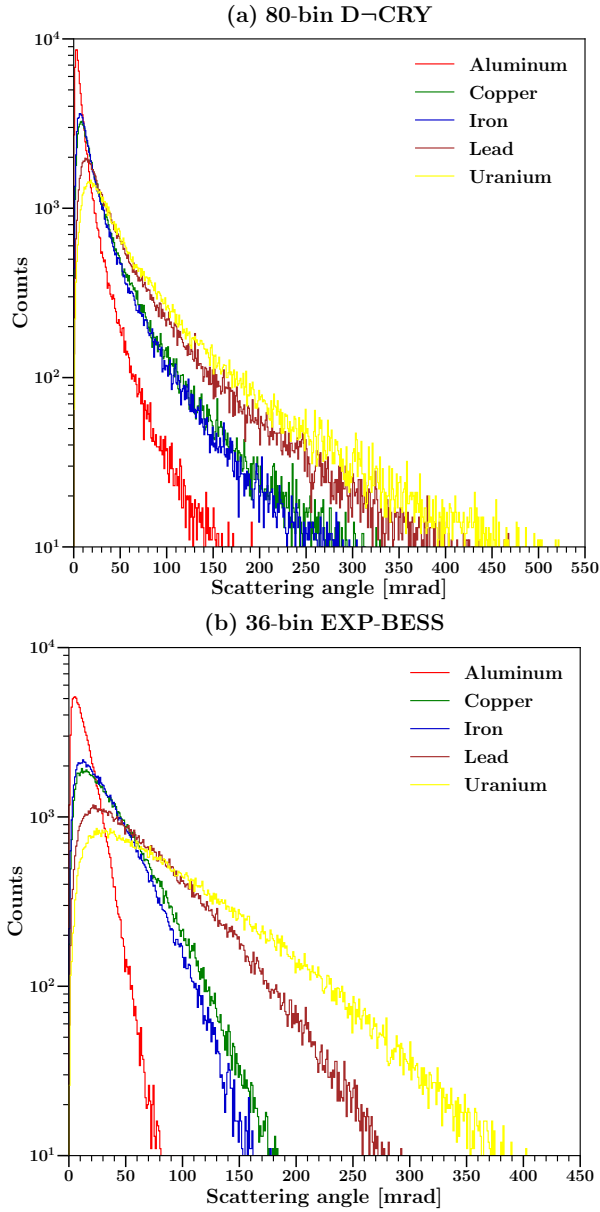


Figure 34: Difference between the angular counts by using a step length of 1 mrad (a) 80-bin D-CRY and (b) 36-bin EXP-BESS.

Then, we also determine the average scattering angle as well as the RMS of the scattering angle in addition to the muon absorption and we compare both the discrete muon sources, i.e. 80-bin D-CRY and 36-bin EXP-BESS, as listed in Table 18. From the contrast shown in Table 18, we

initially observe that the average scattering angle acquired via these discrete distributions is alike except in the case of lead and uranium. Secondly, 80-bin D-CRY constantly results in a strikingly higher standard deviation in comparison with 36-bin EXP-BESS since the first five energy bins of 80-bin D-CRY constitute a low-energy population excluded in 36-bin EXP-BESS that drastically amplifies the propagated uncertainty. Furthermore, this increased tendency is also examined in the RMS values owing to the same reason. Crucially, an essential fact is traced in the event of the muon absorption, and we demonstrate that 36-bin EXP-BESS does not yield any muon capture within the VOI since the energy level above 0.598 GeV has no potential for the muon absorption when the material thickness is merely 10 cm by recalling that the lower bound of 36-bin EXP-BESS is 0.598 GeV, while the lowest bin value in 80-bin D-CRY belongs to 0.1 GeV.

Table 18: Characteristic parameters obtained via 80-bin D-CRY as well as 36-bin EXP-BESS.

Material	$\bar{\theta}_{\text{D-CRY}} \pm \delta\theta$ [mrad]	$\theta_{\text{D-CRY}}^{\text{RMS}}$ [mrad]	$\#_{\text{D-CRY}}^{\text{Capture}}$	$\bar{\theta}_{\text{EXP-BESS}} \pm \delta\theta$ [mrad]	$\theta_{\text{EXP-BESS}}^{\text{RMS}}$ [mrad]	$\#_{\text{EXP-BESS}}^{\text{Capture}}$
Aluminum	15.980±27.004	31.378	-	15.036±12.413	19.499	-
Copper	40.638±60.312	72.725	1230±35	40.759±31.898	51.757	-
Iron	35.824±51.548	62.773	1222±35	36.200±28.518	46.084	-
Lead	65.325±88.323	109.856	1272±36	68.138±52.450	85.987	-
Uranium	81.822±100.321	129.457	3836±62	95.721±75.376	121.836	-

12 Particle generation through restrictive planes in GEANT4 simulations for potential applications of cosmic ray muon tomography

12.1 Introduction

Motivated by the excessive particle loss and its effect on the computation time as well as the characteristic parameters identified in the muon tomography, we set forth in the present study a scheme that is hinged on the particle generation through the planar restriction by means of the vectorial construction over our tomographic setup consisting of plastic scintillators manufactured from polyvinyl toluene with the dimensions of $100 \times 0.4 \times 100$ cm³. This study is organized as follows. In section 12.2, we elucidate our methodology based on the restrictive planes and we express our characteristic parameters as well as our simulation features in section 12.3. We disclose our simulation outcomes in section 12.4.

12.2 Generation via planar restriction

To begin with, we principally exhibit two planar restrictive schemes to be adapted in GEANT4 as illustrated in Fig. 35 where (a) shows the particle generation from a fixed point as well as the direction restriction by means of a restrictive pseudo-plane, whereas (b) demonstrates the randomly picked up particles from a generative plane, the directions of which are projected into a similar restrictive plane.

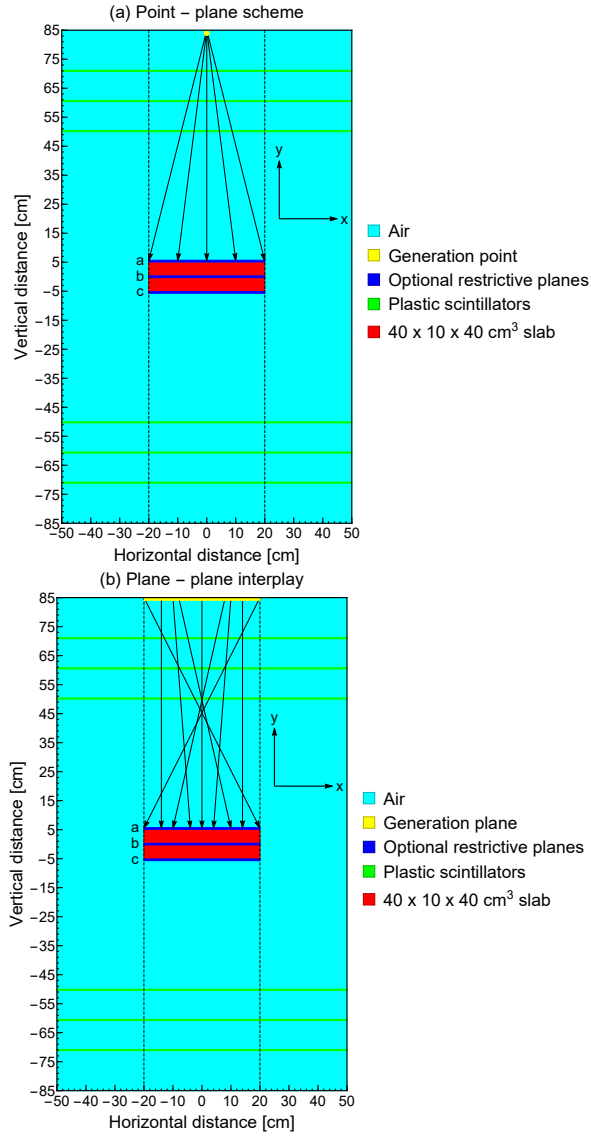


Figure 35: Depiction of particle generation through restrictive planes in GEANT4 (a) generative point - restrictive plane scheme and (b) generative - restrictive planar interplay.

In order to practically outline the present methodology that is initially described in Fig. 35(a), the particle location in cm on the central point at height=85 cm is listed as written in

$$x_0 = 0, \quad y_0 = 85, \quad z_0 = 0 \quad (73)$$

Subsequently, the confined location in cm on any restrictive plane of $2L \times 2D \text{ cm}^2$ is noted as shown in

$$\begin{aligned}x_1 &= -L + 2 \times L \times \text{G4UniformRand}(), \\y_1 &= \text{constant}, \\z_1 &= -D + 2 \times D \times \text{G4UniformRand}()\end{aligned}\tag{74}$$

Here, $\text{G4UniformRand}()$ is the uniform random number generator between 0 and 1, which is pre-defined in GEANT4. Then, by constructing a vector from the generative point to the restrictive plane, we obtain

$$\begin{aligned}px &= x_1 - x_0 = x_1, \\py &= y_1 - y_0, \\pz &= z_1 - z_0 = z_1\end{aligned}\tag{75}$$

Thus, the selective momentum direction, i.e. $\vec{P} = (P_x, P_y, P_z)$, is

$$\begin{aligned}P_x &= \frac{px}{\sqrt{px^2 + py^2 + pz^2}}, \\P_y &= \frac{py}{\sqrt{px^2 + py^2 + pz^2}}, \\P_z &= \frac{pz}{\sqrt{px^2 + py^2 + pz^2}}\end{aligned}\tag{76}$$

The latter scheme that assumes a planar generation as delineated in Fig. 35(b) entails particle locations in cm on the generative plane of $2L \times 2D \text{ cm}^2$ as written in

$$\begin{aligned}x_0 &= -L + 2 \times L \times \text{G4UniformRand}(), \\y_0 &= 85, \\z_0 &= -D + 2 \times D \times \text{G4UniformRand}()\end{aligned}\tag{77}$$

As performed in Eq. 74 for the previous scheme, the limited locations in cm on any restrictive plane of $2L \times 2D \text{ cm}^2$ are selected from

$$\begin{aligned}x_1 &= -L + 2 \times L \times \text{G4UniformRand}(), \\y_1 &= \text{constant}, \\z_1 &= -D + 2 \times D \times \text{G4UniformRand}()\end{aligned}\tag{78}$$

Additionally, via a vector construction between two planes, we acquire anew

$$px = x_1 - x_0, \quad py = y_1 - y_0, \quad pz = z_1 - z_0\tag{79}$$

Therefore, the selective momentum direction denoted by $\vec{P} = (P_x, P_y, P_z)$ is again

$$\begin{aligned} P_x &= \frac{px}{\sqrt{px^2 + py^2 + pz^2}}, \\ P_y &= \frac{py}{\sqrt{px^2 + py^2 + pz^2}}, \\ P_z &= \frac{pz}{\sqrt{px^2 + py^2 + pz^2}} \end{aligned} \quad (80)$$

The initial particle positions and the selective momentum directions are incorporated by using G4ParticleGun. The simulation previews through both the restrictive schemes are displayed in Fig. 36 where (a) indicates the particles generated from a fixed point, while (b) presents the randomly generated particles from a fixed plane.

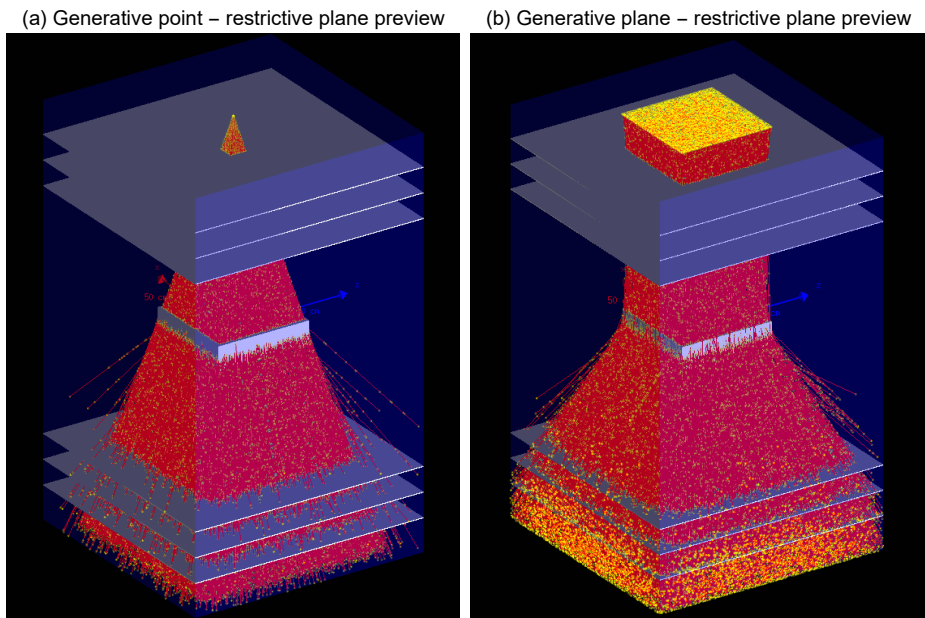


Figure 36: Simulation previews by using restrictive plane b for copper in GEANT4 (a) point - plane scheme and (b) plane - plane scheme.

It is worth mentioning that neither generation points/planes nor restrictive planes are subject to any limitation in terms of shape, size, or location since our recent concept is preferred in the first instance for the sake of simplicity. On top of this, it is also possible to favor different distributions especially already implemented in GEANT4, e.g. Gauss or Poisson distribution depending on the envisaged application.

12.3 Characteristic parameters and simulation setup

Before getting down to test our schemes, we express our characteristic parameters to be computed in the wake of the GEANT4 simulations. The average scattering angle due to the target volume and its standard deviation over N number of the non-absorbed/non-decayed muons is determined as expressed in Eqs. (41) and (42). Additionally, the root-mean-square (RMS) of the scattering angle over N number of the non-absorbed/non-decayed muons is calculated by using Eq. (72). Along with the scattering angle, we squarely track the number of the absorbed muons within the VOI as denoted in Eq. (57).

Last but not least, we define the particle loss entitled off-target loss as follows

$$\#_{\text{Loss}}^{\text{Off-target}} \approx \underbrace{\#_{\text{Out-scattering}}}_{\text{Characteristic}} + \underbrace{\#_{\text{Decay}}}_{\text{Negligible}} + \underbrace{\#_{\text{Capture}}^{\text{Off-target}}}_{\text{Negligible}} + \underbrace{\#_{\text{Deflection}}^{\text{Initial}}}_{\text{Occasional}} \quad (81)$$

where $\#_{\text{Out-scattering}}$ is the number of the scattered muons from the VOI by leaking out of the tomographic device, $\#_{\text{Decay}}$ is the negligible number of the decayed muons into electrons/positrons, $\#_{\text{Capture}}^{\text{Off-target}}$ is the insignificant number of the absorbed muons outside the VOI, and $\#_{\text{Deflection}}^{\text{Initial}}$ is the number of muons that miss the VOI only in the case of the wide beams, which occasionally occurs due to the barriers before the VOI despite the initial restricted orientation to the VOI boundary, i.e. the tiny deflection owing to the detector layers.

Table 19: Simulation features.

Particle	μ^-
Momentum direction	Restrictive downward
Beam geometry	Prismatic
Initial position (cm)	y=85
Particle injector	G4ParticleGun
Number of particles	10^5
Energy distribution	Non-linear discrete
Energy interval	[0, 8]
Energy bin step length (GeV)	0.1
Target geometry	Rectangular prism
Target volume (cm ³)	40×10×40
Material database	G4/NIST
Reference physics list	FTFP_BERT

Our simulation features are summarized in Table 19, and we use a 80-bin discrete muon energy spectrum extracted from the CRY generator [31]

between 0 and 8 GeV. The muon tracking is accomplished by G4Step, and the recorded hit positions on the detector layers are post-processed at the hand of a Python script.

12.4 Simulation outcomes

We asses our methodology over our tomographic configuration described in Fig. 35(a)-(b) and we select our set of materials and the VOI geometry in accordance with another study [89] dedicated to the muon tomography where the material list consists of aluminum, copper, iron, lead, and uranium, and the target geometry is composed of a rectangular prism with the dimensions of $40 \times 10 \times 40$ cm³. As indicated in Fig. 35, we contrast three restrictive planes labeled as a, b, and c that are placed atop the VOI, amidst the VOI, and beneath the VOI, respectively. We commence with the first scheme that is based on the point - plane generation, and the simulation outcomes by using restrictive plane a are listed in Table 20.

Table 20: Point - plane scheme, restrictive plane a, thickness=10 cm.

Material	$\bar{\theta} \pm \delta\theta$ [mrad]	θ_{RMS} [mrad]	$\#_{\text{Capture}}^{\text{In-target}}$	$\#_{\text{Loss}}^{\text{Off-target}}$
Aluminum	14.890±25.741	29.738	-	516±23
Copper	37.376±55.515	66.924	1083±33	616±25
Iron	32.980±47.420	57.761	1073±33	541±23
Lead	59.486±81.898	101.222	1135±34	1215±35
Uranium	73.649±91.114	117.158	3267±57	1542±39

As shown in Table 20, the computed parameters including the particle loss show a characteristic tendency depending on the atomic number as well as the material density for a fixed thickness. Although the muon beam is already directed to the VOI boundary even in the case of restrictive plane a, which leads to an immoderate reduction in the particle loss compared to the conventional approaches, a remarkable number of the loss events in agreement with the intrinsic properties of the target material are still observed.

Table 21: Point - plane scheme, restrictive plane b, thickness=10 cm.

Material	$\bar{\theta} \pm \delta\theta$ [mrad]	θ_{RMS} [mrad]	$\#_{\text{Capture}}^{\text{In-target}}$	$\#_{\text{Loss}}^{\text{Off-target}}$
Aluminum	15.771±26.427	30.775	-	54±7
Copper	39.545±56.941	69.326	1179±34	216±15
Iron	35.306±50.117	61.304	1172±34	133±12
Lead	63.172±84.172	105.241	1220±35	833±29
Uranium	78.160±93.551	121.904	3604±60	1187±34

In order to see the positional effect of the planar restriction, the simulation outcomes from restrictive plane b are tabulated in Table 21. In comparison with Table 20, we observe that the characteristic parameters except the particle loss slightly change when the muon beam is narrowed by using restrictive plane b; however, the particle loss manifests a minimum reduction of 31% as opposed to restrictive plane a. Whereas restrictive plane b is capable of diminishing the particle loss by a factor of order in certain cases, we still notice that the particle loss remains distinctive among the simulated materials.

By using restrictive plane c, we further decrease the incident angle and we obtain the simulation results as written down in Table 22. In comparison with Table 21, restrictive plane c yields a minuscule change in terms of the characteristic parameters containing the particle loss, which also means that the variation rate of the characteristic parameters is expected to be insignificant beyond restrictive plane c.

Table 22: Point - plane scheme, restrictive plane c, thickness=10 cm.

Material	$\bar{\theta} \pm \delta\theta$ [mrad]	θ_{RMS} [mrad]	$\#_{\text{Capture}}^{\text{In-target}}$	$\#_{\text{Loss}}^{\text{Off-target}}$
Aluminum	16.142±27.368	31.774	-	35±6
Copper	40.355±58.022	70.676	1216±35	193±14
Iron	35.916±50.635	62.080	1215±35	107±10
Lead	64.542±85.965	107.497	1287±36	793±28
Uranium	79.700±96.102	124.850	3764±57	1059±33

It is noteworthy to mention that a partial transition from the particle loss to the particle absorption is perceptible according to Tables 20-22 especially if the VOI material is a potent absorber since the low-energy muons

that lead to the particle loss in the wide beams typically have the absorption potential when interacting with the VOI material in the narrow beams, which also means that a certain portion of the particle loss is converted into the particle absorption in the VOI material towards restrictive plane c.

Table 23: Plane - plane scheme, restrictive plane a, thickness=10 cm.

Material	$\bar{\theta} \pm \delta\theta$ [mrad]	θ_{RMS} [mrad]	$\#_{\text{Capture}}^{\text{In-target}}$	$\#_{\text{Loss}}^{\text{Off-target}}$
Aluminum	15.196±26.036	30.146	-	1196±35
Copper	37.454±55.612	67.049	1118±33	1728±42
Iron	33.375±48.047	58.502	1092±33	1575±40
Lead	59.927±83.320	102.633	1206±35	2624±51
Uranium	74.073±92.787	118.728	3352±58	3299±57

In the next step, we continue with the plane - plane scheme, and Table 23 lists the simulation outcomes for restrictive plane a. In spite of the schematic change, we see that the characteristic parameters excluding the particle loss do not exhibit a significant difference. On the other hand, the particle loss via restrictive plane a within the plane - plane interplay results in the elevated values as displayed in Table 23 in contrast to Tables 20-22.

Table 24: Plane - plane scheme, restrictive plane b, thickness=10 cm.

Material	$\bar{\theta} \pm \delta\theta$ [mrad]	θ_{RMS} [mrad]	$\#_{\text{Capture}}^{\text{In-target}}$	$\#_{\text{Loss}}^{\text{Off-target}}$
Aluminum	16.103±27.566	31.925	-	138±12
Copper	39.897±57.927	70.337	1220±35	581±24
Iron	35.380±50.142	61.367	1206±35	430±21
Lead	63.335±84.573	105.659	1327±36	1423±38
Uranium	78.399±94.631	122.888	3699±61	1926±44

So as to demonstrate the impact of the spatial change in the planar restriction for this scheme, the simulation results via restrictive plane b are tabulated in Table 24, and we experience a similar trend compared to the point-plane scheme that induces a drastic diminution in the particle loss along with the tiny variations in the rest of the characteristic parameters. As a means to complete our quantitative investigation for the plane - plane scheme, the simulation results for restrictive plane c are listed in Table 25,

and we face a close trend as opposed to Table 22, which also means that the reduction rate in the particle loss is moderated together with the very minor variations in the remaining characteristic parameters.

Table 25: Plane - plane scheme, restrictive plane c, thickness=10 cm.

Material	$\bar{\theta} \pm \delta\theta$ [mrad]	θ_{RMS} [mrad]	$\#_{\text{Capture}}^{\text{In-target}}$	$\#_{\text{Loss}}^{\text{Off-target}}$
Aluminum	16.279±27.365	31.841	-	88±9
Copper	40.386±57.627	70.370	1258±35	389±20
Iron	36.135±50.751	62.300	1249±35	263±16
Lead	64.517±86.095	107.586	1358±37	1164±34
Uranium	80.087±96.225	125.193	3833±62	1537±39

In the long run, our last simulations are devoted to investigate the thickness effect by solely using restrictive plane b since we aim at optimizing the particle loss with an ideal angular acceptance. Thus, Table 26 shows the characteristic parameters that are acquired by means of the point - plane scheme as well as restrictive plane b for a thickness of 40 cm with the same material group.

Table 26: Point - plane scheme, restrictive plane b, thickness=40 cm.

Material	$\bar{\theta} \pm \delta\theta$ [mrad]	θ_{RMS} [mrad]	$\#_{\text{Capture}}^{\text{In-target}}$	$\#_{\text{Loss}}^{\text{Off-target}}$
Aluminum	27.849±37.186	46.458	3046±55	93±10
Copper	65.133±75.969	100.068	11072±105	588±24
Iron	58.208±67.893	89.429	10365±102	528±23
Lead	102.566±112.951	152.570	11036±105	2210±47
Uranium	121.060±121.502	171.517	20371±143	3084±55

From Table 26, we numerically demonstrate that all the characteristic parameters increase as a function of thickness, and we find the most notable rise in the particle absorption. Finally, Table 27 lists the simulation results through the plane-plane scheme for the same thickness, and we see that the latter scheme is not significantly different from the initial scheme with regard to the characteristic parameters omitting a higher number of the particle loss.

Table 27: Plane - plane scheme, restrictive plane b, thickness=40 cm.

Material	$\bar{\theta} \pm \delta\theta$ [mrad]	θ_{RMS} [mrad]	$\#_{\text{Capture}}^{\text{In-target}}$	$\#_{\text{Loss}}^{\text{Off-target}}$
Aluminum	28.022±37.620	46.910	3080±55	272±16
Copper	65.229±77.147	101.026	11341±106	1184±34
Iron	58.373±68.363	89.894	10599±103	1086±33
Lead	101.906±113.230	152.335	11341±106	3341±58
Uranium	120.089±121.872	171.097	20867±144	4181±65

13 DOME: Discrete oriented muon emission in GEANT4 simulations

13.1 Introduction

In practice, various shapes of radiation sources including but not limited to planar surfaces and parabolic beams have been utilized to mimic the associated reality in the desired applications, and one of these geometries includes hemispherical surfaces [90]. In this study, we describe the implementation steps of two schemes by aiming at building a hemispherical muon source where the generated particles are oriented towards a specific point or plane that we call selective momentum direction. While there exist different schemes to generate the 2D/3D sources, we prefer to use the existing algorithms in GEANT4 [1], i.e. `G4RandGauss::shoot()` and `G4UniformRand()` as a distribution function. Whereas the geometrical shape of the 2D/3D sources plays an important role or is a parameter for this aim, the momentum direction is another variable that awaits for a user decision. In this study, we first generate a spherical surface by using three Gaussian distributions for the three components of the Cartesian coordinates and we direct the generated particles from their initial positions on this spherical surface to the preferred location(s) by using a vector construction as described in our previous study [91]. This methodology is called discrete oriented muon emission (DOME) where the kinetic energy of the generated particles is intentionally discrete for the computational purposes as already implemented in another study [92]. In the latter scheme, we generate the initial positions by randomizing the spherical variables, i.e. altitude and longitude, and we perform the coordinate transformation from the spherical coordinates to the Cartesian coordinates [93–95]. We repeat the same operations as performed in the first scheme. This study is organized as follows. Section 13.2.1 describes the first scheme that is hinged on the Gaussian distribution functions, while section 13.2.2 consists of the second methodology founded on the coordinate transformation from the spherical coordinates to the Cartesian coordinates. An alternative focusing scheme is explained in section 13.3.

13.2 Central focus scheme

13.2.1 Generation through Gaussian distributions

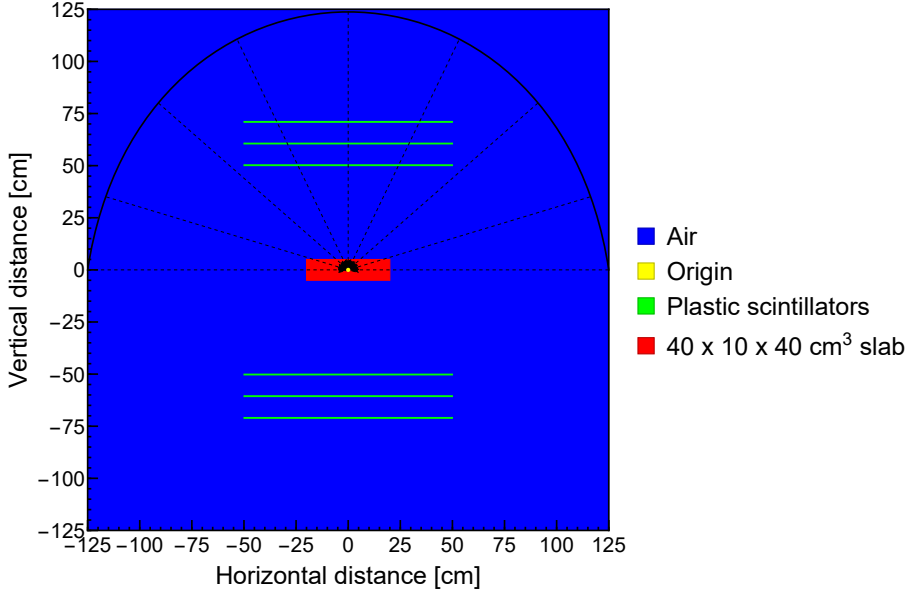


Figure 37: Delineation of the generated particles from the hemispherical source with a momentum direction towards the origin.

Our objective is to build a hemispherical muon source that surrounds our tomographic setup [14] similar to the other tomographic configurations existing in the literature [5, 13, 96] as delineated in Fig. 37. On the first basis, the particle locations in the Cartesian coordinates are generated by using the Gaussian distributions formally defined as `G4RandGauss::shoot()` in GEANT4 (see Appendix D) as written in

$$x_0 = G(\bar{x}, \sigma_x, x) = \text{G4RandGauss}::\text{shoot}() \quad (82)$$

and

$$y_0 = G(\bar{y}, \sigma_y, y) = \text{G4RandGauss}::\text{shoot}() \quad (83)$$

and

$$z_0 = G(\bar{z}, \sigma_z, z) = \text{G4RandGauss}::\text{shoot}() \quad (84)$$

where $\bar{x} = \bar{y} = \bar{z} = 0$ and $\sigma_x = \sigma_y = \sigma_z = 1$ by definition. The generated spatial points are renormalized in order to form a unit sphere as indicated in

$$x_0^* = \frac{x_0}{\sqrt{x_0^2 + y_0^2 + z_0^2}}, \quad y_0^* = \frac{y_0}{\sqrt{x_0^2 + y_0^2 + z_0^2}}, \quad z_0^* = \frac{z_0}{\sqrt{x_0^2 + y_0^2 + z_0^2}} \quad (85)$$

Given a sphere of radius denoted by R , the initial positions on the spherical surface of radius R in cm in the Cartesian coordinates are obtained as follows

$$x_i = R * x_0^*, \quad y_i = R * |y_0^*| = R * \text{ABS}(y_0^*), \quad z_i = R * z_0^* \quad (86)$$

where the y-component of the Cartesian coordinates constituting the vertical axis is positively defined in order to yield the hemispherical surface. Then, the generated particles on the spherical surface are directed to the origin

$$x_f = 0, \quad y_f = 0, \quad z_f = 0 \quad (87)$$

Then, by constructing a vector from the hemispherical surface to the origin, one obtains

$$px = x_f - x_i, \quad py = y_f - y_i, \quad pz = z_f - z_i \quad (88)$$

Thus, the selective momentum direction denoted by $\vec{P} = (P_x, P_y, P_z)$ is

$$\begin{aligned} P_x &= \frac{px}{\sqrt{px^2 + py^2 + pz^2}}, \\ P_y &= \frac{py}{\sqrt{px^2 + py^2 + pz^2}}, \\ P_z &= \frac{pz}{\sqrt{px^2 + py^2 + pz^2}} \end{aligned} \quad (89)$$

13.2.2 Generation via coordinate transformation

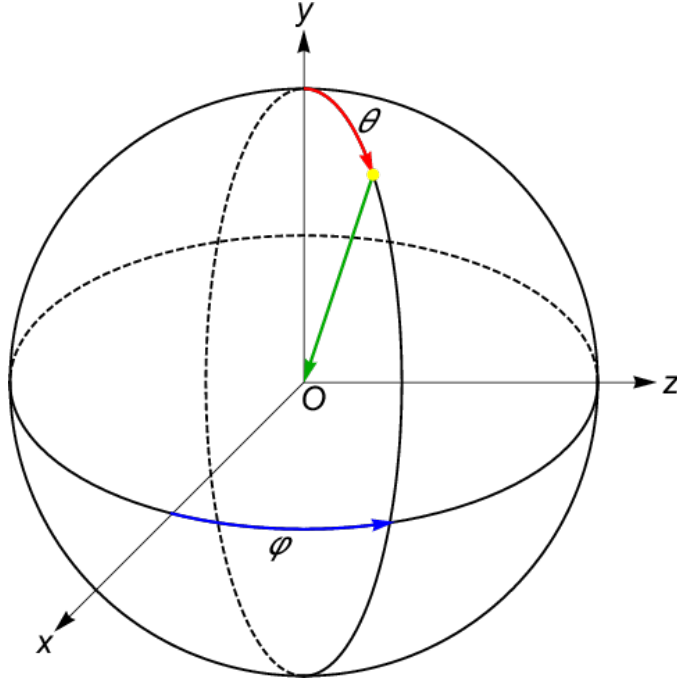


Figure 38: Spherical variables consisting of θ and φ with respect to the Cartesian coordinates (x,y,z) .

The latter scheme (see Appendix E) is composed of the coordinate transformation as shown in Fig. 38. To begin with, two numbers, i.e. q_1 and q_2 , are uniformly generated to be inserted to the associated expression of the spherical variables as follows

$$q_1 = \text{G4UniformRand()} \quad (90)$$

and

$$q_2 = \text{G4UniformRand()} \quad (91)$$

The surface generation is initiated by randomizing θ as well as φ as shown in

$$\theta = \arccos(2 \times q_1 - 1) \quad (92)$$

and

$$\varphi = 2 \times \pi \times q_2 \quad (93)$$

The coordinate transformation yields the generated points on the hemispherical surface for a sphere of radius R in the Cartesian coordinates as described in

$$x_i = R \times \sin \theta \times \cos \varphi \quad (94)$$

and

$$y_i = R \times |\cos \theta| = R \times \text{ABS}(\cos \theta) \quad (95)$$

and

$$z_i = R \times \sin \theta \times \sin \varphi \quad (96)$$

where the y-component of the Cartesian coordinates constituting the vertical axis is repeatedly positively defined in order to yield the hemispherical surface as usual. Then, the generated particles on the spherical surface are again directed to the origin

$$x_f = 0, \quad y_f = 0, \quad z_f = 0 \quad (97)$$

Then, by constructing a vector from the hemispherical surface to the origin, one obtains

$$px = x_f - x_i, \quad py = y_f - y_i, \quad pz = z_f - z_i \quad (98)$$

Thus, the selective momentum direction denoted by $\vec{P} = (P_x, P_y, P_z)$ is

$$\begin{aligned} P_x &= \frac{px}{\sqrt{px^2 + py^2 + pz^2}}, \\ P_y &= \frac{py}{\sqrt{px^2 + py^2 + pz^2}}, \\ P_z &= \frac{pz}{\sqrt{px^2 + py^2 + pz^2}} \end{aligned} \quad (99)$$

Finally, the simulation preview through either scheme is displayed in Fig. 39.

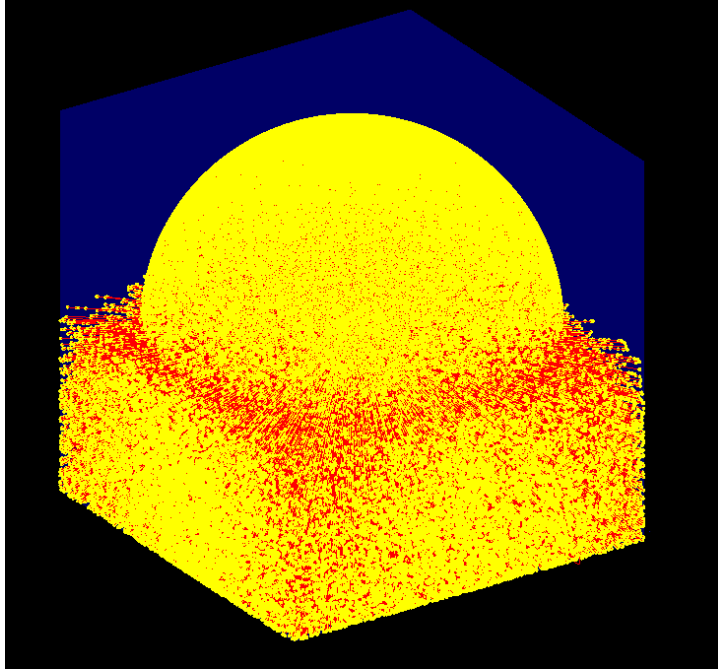


Figure 39: Hemispherical muon source in GEANT4 with radius=100 cm.

13.3 Restrictive planar focus scheme

The generated particles from any initial point on the hemispherical surface might be directed to a location randomly selected on a pseudo plane that restricts the momentum direction, which also leads to the minimization of the particle escape. Thus, the particle locations in cm on a restrictive plane of $2L \times 2D$ cm² situated at $y=0$ are supposed to have the spatial coordinates such that

$$\begin{aligned}
 x_f &= -L + 2 \times L \times \text{G4UniformRand}(), \\
 y_f &= 0, \\
 z_f &= -D + 2 \times D \times \text{G4UniformRand}()
 \end{aligned}
 \tag{100}$$

Then, by constructing a vector from the generative hemispherical surface to the restrictive plane, one obtains

$$px = x_f - x_i, \quad py = y_f - y_i, \quad pz = z_f - z_i
 \tag{101}$$

Thus, the selective momentum direction, i.e. $\vec{P} = (P_x, P_y, P_z)$, is

$$\begin{aligned} P_x &= \frac{px}{\sqrt{px^2 + py^2 + pz^2}}, \\ P_y &= \frac{py}{\sqrt{px^2 + py^2 + pz^2}}, \\ P_z &= \frac{pz}{\sqrt{px^2 + py^2 + pz^2}} \end{aligned} \tag{102}$$

14 Conclusion

At the end of this PhD study, we draw the following conclusions:

* In chapter 2.6, we ameliorate the width of the deflection angle by averaging the simulation outcomes from the top detector layers and the bottom detector layers over the number of the non-absorbed/non-decayed muons. Since the average deflection angles are mostly below the current detector accuracy that is 1 mrad, we introduce the stainless steel layers to augment the average deflection angles as well as to further diminish the standard deviations;

* In chapter 4, we computationally explore the feasibility of assembling the tracked muons based on the deflection angles that are generated in the plastic scintillators. We attempt to coarsely predict the kinetic energies by using the average deflection angles and the associated standard deviations. We verify a moderate number of energy groups by using two different approaches. We demonstrate that the higher the group number is, the higher the misclassification probability is;

* In chapter 5, we investigate an alternative tomographic setup by introducing stainless steel layers into the bottom section and the top section with the aim of the uncertainty reduction in the deflection angle. Upon our GEANT4 simulations combined with two distinct forms of the misclassification probabilities, we experience that the stainless steel layers slightly yield more favorable angular values with the diminished uncertainty as opposed to our current prototype apart from the increased average deflection angles that fulfill the present detector accuracy. Within the perspective of an indirect energy classification dependent on the deflection angle, our simulation outcomes qualitatively and quantitatively indicate that the presence of stainless steel layers might be an inexpensive upgrade in the potential applications of the muon scattering tomography;

* In chapter 6, we explore the triangular correlation of angular deviation

by means of our GEANT4 simulations. Upon our simulation outcomes, we explicitly observe that the conventional scattering angle remains constant towards the position change of the target material, whereas the opposite interior angles exhibit differences due to this spatial variation, therewith hinting a beneficial property to be utilized for the image reconstruction purposes;

* In chapter 7, we show that the triangular correlation of the angular deviation holds for the multi-block material configurations. Moreover, we also imply that this triangular correlation might provide supportive information for the coarse prediction of the material order in such configurations;

* In chapter 8, the nuclear waste barrels containing a certain amount of bulky radioactive waste have been quantitatively investigated with regard to the scattering angle as well as the absorption rate by using the GEANT4 simulations for the application in muon scattering tomography. Concerning the scattering angle, we demonstrate that a waste barrel with the bulky cobalt, uranium, and plutonium might be detected by using muon tomography. According to our GEANT4 simulations, we also show that the absorption rate might act as a complementary characteristic parameter in addition to the scattering angle in the case of the mid/high density materials with the condition of the long exposure periods. As a future work, one might utilize these two characteristic parameters in order to train a classifier by aiming at identifying the content of the waste barrels as well as characterizing the performance of this classifier;

* In chapter 9, we demonstrate that the presence of uranium and plutonium in the cementitious forms is qualitatively and quantitatively traceable from the characteristic parameters, while the remaining radioactive waste/cement mixtures with the nuclear sources such as cobalt, strontium, and caesium do not show a significant variation compared to the ordinary concrete slab since the intrinsic properties of the resulting mixtures that govern the characteristic parameters are predominantly controlled by the matrix properties if the associated additives are not significantly denser along with the substantially higher Z -values;

* In chapter 10, we compute the energy difference between the hodoscope sections in the presence of the nuclear waste barrels and we show that the energy loss is a non-negligible characteristic parameter that varies in accordance with the intrinsic properties of the target volumes. For the image reconstruction codes where the kinetic energy of the incoming muons is coarsely determined by using the deflection angle, we emphasize the necessity of a correction factor that renormalizes the bottom deflection af-

ected by the corresponding VOIs. By aiming at characterizing the target volume, this correction factor might be used to provide complementary details in addition to the scattering information in the course of the image reconstruction;

* In chapter 11, we state a procedure based on the multi-group energy approximation where we favor the utilization of the binned energy values connected with the discrete probabilities by means of a probability grid. Consequently, we gain the capability to control as well as to adjust our energy spectra according to our computational goals apart from the noteworthy computation times;

* In chapter 12, by setting out our restrictive generation scheme, we optimize the particle loss by keeping an angular acceptance that is directly dependent on the VOI geometry as well as the vertical position of the restrictive plane for a tomographic system of a finite size. Upon our simulation outcomes, we show that the particle generation by means of restrictive planes is an effective strategy that is flexible towards a variety of computational objectives in GEANT4. Into the bargain, we explicitly observe that the off-target loss is a characteristic parameter that varies in an ascending order from aluminum to uranium;

* In chapter 13, we explore the possibility to use the random number generators that are already defined in the GEANT4 code. By profiting from these random number generators, we provide a number of source schemes where the first strategy is based on the Gauss distributions, whereas the latter procedure requires a coordinate transformation by utilizing the spherical variables. Finally, we obtain a hemispherical muon source where the kinetic energies of the generated muons are discretized, and the momentum directions of these generated muons are selective by means of the vector constructions. We call this source discrete oriented muon emission (DOME).

15 Discussion

We briefly outline the impact of our studies as follows. Initially, we roughly estimate the kinetic energy of incoming muons by inserting a stainless steel layer into the hodoscope sections, which increases the angular values as well as decreases the standard deviations thanks to its atomic number and density. We show that this methodology is only feasible when a metallic layer is introduced into the tomographic configuration. The number of the energy groups obtained through this strategy might be up to four due to the overlaps between the group intervals. This energy classification is expected to lead to a better image in the course of the image reconstruction process, e.g. theoretically a three-group structure is supposed to produce better images in comparison with the one-group structure. Secondly, we demonstrate the triangular correlation where the interior angles are sensitive towards the change in the vertical position as well as the material order, while the conventional scattering angle does not exhibit any significant variation. This feature might be useful for the image reconstruction codes in order to capture such spatial changes; otherwise, the regular scattering angle is not able to capture the vertical position change as well as the material order according to our GEANT4 simulations. In the next step, we show that the characteristic parameters that are the scattering angle and the absorption rate might be combined in order to discriminate the nuclear waste barrels during the non-destructive interrogations. We already demonstrate that the utilization of these two parameters is enough to characterize the nuclear waste barrels that contain a volume of bulky cobalt, uranium, or plutonium. For the homogenized nuclear waste barrels, these two parameters lead to the promising results in the case of the uranium-cement or plutonium-cement mixture. Over the nuclear waste barrels, we show that the deposited energy within the target volumes might not be negligible so that the kinetic energy of the incoming muons might be significantly different from the outgoing muons. In those cases, a correction factor might be necessary for the image reconstruction codes that are based on the deflection angle, and this correction factor is another characteristic parameter that depends on the thickness, the density, and the atomic number of the corresponding target. Furthermore, we optimize our muon sources in such a way that it can bring a number of advantages, e.g. minimization of the particle loss in the case of the restrictive plane and the full angular coverage by using the DOME source. Finally, the computational outcomes in this PhD thesis might lead to a simulation/image reconstruction framework by aiming at the characterization of the nuclear materials in diverse applications.

Appendices

Appendix A: Stepping action

The propagating muons are tracked by utilizing the following GEANT4 statements:

```
void B1SteppingAction::UserSteppingAction(const G4Step* step)
{
//G4Track
G4VPhysicalVolume* Volume = step->GetPreStepPoint()->
GetTouchableHandle()->GetVolume();
G4LogicalVolume* LogicalVolume = step->GetPreStepPoint()->
GetTouchableHandle()->GetVolume()->GetLogicalVolume();
G4Track* track = step->GetTrack();
const G4DynamicParticle* dynpar = track->GetDynamicParticle();
G4ParticleDefinition* particle = dynpar->GetDefinition();
G4double KineticEnergy = dynpar->GetKineticEnergy();
G4ThreeVector Momentum = dynpar->GetMomentum();
G4double MomenX = dynpar->GetMomentum().x();
G4double MomenY = dynpar->GetMomentum().y();
G4double MomenZ = dynpar->GetMomentum().z();
G4double MomentumMagnitude =
sqrt(pow(MomenX,2)+pow(MomenY,2)+pow(MomenZ,2));
G4StepPoint* PostPoint = step->GetPostStepPoint();
G4ThreeVector Position = PostPoint->GetPosition();
G4double PosX = PostPoint->GetPosition().x()/cm;
G4double PosY = PostPoint->GetPosition().y()/cm;
G4double PosZ = PostPoint->GetPosition().z()/cm;
G4int TrackID = track->GetTrackID();
G4String ProcessName = PostPoint->
GetProcessDefinedStep()->GetProcessName();
G4String ParticleName = particle->GetParticleName();
if (Volume->GetName() == "TopHodoscope2" ||
Volume->GetName() == "TopHodoscope3" ||
Volume->GetName() == "BottomHodoscope1" ||
Volume->GetName() == "BottomHodoscope2") {
if (ParticleName == "mu+" || ParticleName == "mu-") {
if (ProcessName == "Transportation"){
G4cout << TrackID << " " << PosX <<
" " << PosY << " " << PosZ << " " << KineticEnergy << " "
<< MomentumMagnitude << " " << Volume->GetName()
<< " " << ProcessName << G4endl;
std::ofstream MyFile;
MyFile.open("waste_mixCs.csv", std::ios::app);
MyFile << TrackID << " " << PosX
<< " " << PosY << " " << PosZ << " " << KineticEnergy << " "
<< MomentumMagnitude << " " << Volume->GetName() << " "
<< ProcessName << " " << G4endl;
MyFile.close();
std::ofstream CheckFile;
CheckFile.open("waste_mixCs.dat", std::ios::app);
CheckFile << TrackID << " " << PosX << " " << PosY << " "
<< PosZ << " " << KineticEnergy << " " <<
MomentumMagnitude << " " << Volume->GetName() <<
" " << ProcessName << G4endl;
CheckFile.close();
}
}
}
if (Volume->GetName() == "TargetMaterial1" ||
Volume->GetName() == "TargetMaterial2"
|| Volume->GetName() == "TargetMaterial3" ) {
if (ParticleName == "mu+" || ParticleName == "mu-") {
if (ProcessName == "muMinusCaptureAtRest"){
std::ofstream AbsorptionFile;
AbsorptionFile.open("Absorption_mixCs.dat", std::ios::app);
AbsorptionFile << TrackID << " " << PosX << " " << PosY << " "
<< PosZ << " " << KineticEnergy << " " <<
MomentumMagnitude << " "
<< Volume->GetName() << " " << ProcessName << G4endl;
AbsorptionFile.close();
}
}
}
}
```

Appendix B: Scattering angle

The scattering angle calculation for BC/DE is performed by using the following Python statements:

```
import sys
import math
import statistics

def calculateAngle(x,y,z):\
    tetaP1 = (x[0]*x[1]) + (y[0]*y[1]) + (z[0]*z[1])\
    tetaP2 = math.sqrt((x[0]**2)+(y[0]**2)+(z[0]**2))\
    *math.sqrt((x[1]**2)+(y[1]**2)+(z[1]**2))\
    teta = math.acos(tetaP1 / tetaP2)\
    teta = teta * 1000\
    return teta\

try:
    data_input = open("position_sensitivity.csv", "r")
except:
    raise Exception("File doesn't exist!")

try:
    data_output= open("angle.txt", "w")
except:
    data_input.close()
    raise Exception("Can't create output file!")

data_list = data_input.readlines()
data_list.pop(0)

event_num=-1
kinetic_energy=0.0
vector_counter=0
angle_value=0.0
x_value=0.0
y_value=0.0
z_value=0.0
x_vector=[0.0,0.0]
y_vector=[0.0,0.0]
z_vector=[0.0,0.0]
max_energy=0.0
last_kinetic_energy = 1.0
nonzero_kinetic_energy = True

for x in data_list:
    line_list=x.split(",")
    if line_list[0] != event_num:
        #initial line
        if event_num == -1:
            event_num = line_list[0]
            kinetic_energy = float(line_list[4])/1000
            vector_counter = 1
            x_value=float(line_list[1])
            y_value=float(line_list[2])
            z_value=float(line_list[3])
            switch = True
        #different event
        else :
            if(last_kinetic_energy > 0.0):
                nonzero_kinetic_energy = True
            else:
                nonzero_kinetic_energy = False
            if switch :
                if vector_counter == 4:
                    if nonzero_kinetic_energy:
                        data_output.write(event_num + " " + str(kinetic_energy) +
                            " " + str(angle_value) + "\n")
                    if kinetic_energy > max_energy:
                        max_energy = kinetic_energy
                event_num = line_list[0]
                kinetic_energy = float(line_list[4])/1000
                x_value=float(line_list[1])
                y_value=float(line_list[2])
                z_value=float(line_list[3])
                x_vector=[0.0,0.0]
                y_vector=[0.0,0.0]
                z_vector=[0.0,0.0]
                vector_counter = 1
                angle_value = 0.0
                switch = True
```

```

#same event
else :
    last_kinetic_energy = float(line_list[4])/1000
    vector_counter += 1
    if vector_counter == 2:
        x_vector[0] = float(line_list[1]) - x_value
        y_vector[0] = float(line_list[2]) - y_value
        z_vector[0] = float(line_list[3]) - z_value
        x_value=float(line_list[1])
        y_value=float(line_list[2])
        z_value=float(line_list[3])

    if vector_counter >= 3:
        x_vector[1] = float(line_list[1]) - x_value
        y_vector[1] = float(line_list[2]) - y_value
        z_vector[1] = float(line_list[3]) - z_value
        x_value=float(line_list[1])
        y_value=float(line_list[2])
        z_value=float(line_list[3])
    try:
        angle_value = calculateAngle(x_vector,y_vector,z_vector)
        switch = True
    except ZeroDivisionError:
        switch = False
    except:
        print("zomg exception occured!")
        switch = False

#final line
if switch:
    if vector_counter == 4:
        if (last_kinetic_energy > 0.0):
            data_output.write(event_num + " " + str(kinetic_energy) + \
                " " + str(angle_value))
        if kinetic_energy > max_energy:
            max_energy = kinetic_energy

#####Part 2 - Average
data_input.close()
data_output.close()

#Calculate average and std-dev
try:
    data_input = open("angle.txt", "r")
except:
    raise Exception("File doesn't exist!")

try:
    data_output= open("angle_average.txt", "w")
except:
    data_input.close()
    raise Exception("Can't create output file!")

input_list = data_input.readlines()
line_list.clear()
bin_list = []
for x in range(2*(int(max_energy)+2)):
    bin_list.append([])

#seperate into bins
for x in input_list:
    line_list=x.split(" ")
    energy_value = float(line_list[1])
    bin_value = 0.5 if math.modf(energy_value)[0] < 0.5 else 1
    bin_value += math.modf(energy_value)[1]
    bin_index = int(bin_value * 2)
    output_value = float(line_list[2])
    bin_list[bin_index].append(output_value)

#print output in new format
for x in range(len(bin_list)):
    if not bin_list[x]:
        continue
    gev_num = float(0.5/2+(x-1)*0.5)
    occurance = len(bin_list[x])
    average_output = statistics.mean(bin_list[x])
    if occurance > 1:
        std_dev_output = statistics.stdev(bin_list[x])
    else:
        std_dev_output = 0
    max_gev = 8.5
    min_gev = 0.0

```

```
if gev_num > min_gev :
    if gev_num < max_gev:
        data_output.write(str(gev_num) + " " + str(occurance) + \
            " " + str(average_output) + " " + str(std_dev_output) + "\n")

data_input.close()
data_output.close()
```


Appendix D: Generation via Gaussian distributions

```

#include "B1PrimaryGeneratorAction.hh"
#include "G4LogicalVolumeStore.hh"
#include "G4LogicalVolume.hh"
#include "G4Box.hh"
#include "G4RunManager.hh"
#include "G4ParticleGun.hh"
#include "G4ParticleTable.hh"
#include "G4ParticleDefinition.hh"
#include "G4SystemOfUnits.hh"
#include "Randomize.hh"
#include <iostream>
using namespace std;

B1PrimaryGeneratorAction::B1PrimaryGeneratorAction()
: G4VUserPrimaryGeneratorAction(),
  fParticleGun(0)
// fEnvelopeBox(0)
{
  G4int n_particle = 1;
  fParticleGun = new G4ParticleGun(n_particle);

  // default particle kinematic
  G4ParticleTable* particleTable = G4ParticleTable::GetParticleTable();
  G4String particleName;
  G4ParticleDefinition* particle
    = particleTable->FindParticle(particleName="mu-");
  fParticleGun->SetParticleDefinition(particle);
}

B1PrimaryGeneratorAction::~~B1PrimaryGeneratorAction()
{
  delete fParticleGun;
}

//80-bin Discrete CRY Energy Spectrum
void B1PrimaryGeneratorAction::GeneratePrimaries(G4Event* anEvent)
{
  //Discrete probabilities
  double A[] = {0.0, 0.01253639, 0.02574546, 0.02802035, 0.02706636, 0.03528534, 0.02826496,
0.03157946, 0.03078447, 0.02777574, 0.02546415, 0.03150608, 0.02815489,
0.02580661, 0.02364179, 0.02170935, 0.02152589, 0.02348279, 0.02134243,
0.0196913, 0.02036398, 0.01841931, 0.01718402, 0.01700056, 0.01624226,
0.01539835, 0.01536166, 0.01471344, 0.01422421, 0.01412637, 0.01284215,
0.01260977, 0.01213278, 0.0129033, 0.01248746, 0.01196155, 0.01064064,
0.01057949, 0.0096255, 0.0103838, 0.00928304, 0.00879382, 0.00884274,
0.00793767, 0.00786429, 0.00769306, 0.00709376, 0.00736283, 0.0071916,
0.00721607, 0.00692253, 0.00643331, 0.00678799, 0.00673907, 0.00618869,
0.00634769, 0.00665346, 0.00650669, 0.00561385, 0.00589516, 0.00589516,
0.00578508, 0.00557716, 0.00550378, 0.00434187, 0.0043541, 0.00408503,
0.00364472, 0.00399941, 0.00388934, 0.00396272, 0.00431741, 0.00368142,
0.00363249, 0.00362026, 0.00410949, 0.00336342, 0.00358357, 0.00362026,
0.00348573, 0.0035958};
  //Discrete energies
  double B[] = {0.0, 100, 200, 300, 400, 500, 600, 700, 800, 900, 1000,
1100, 1200, 1300, 1400, 1500, 1600, 1700, 1800, 1900, 2000,
2100, 2200, 2300, 2400, 2500, 2600, 2700, 2800, 2900, 3000,
3100, 3200, 3300, 3400, 3500, 3600, 3700, 3800, 3900, 4000,
4100, 4200, 4300, 4400, 4500, 4600, 4700, 4800, 4900, 5000,
5100, 5200, 5300, 5400, 5500, 5600, 5700, 5800, 5900, 6000,
6100, 6200, 6300, 6400, 6500, 6600, 6700, 6800, 6900, 7000,
7100, 7200, 7300, 7400, 7500, 7600, 7700, 7800, 7900, 8000};
  G4int SizeEnergy=sizeof(B)/sizeof(B[0]);
  G4int SizeProbability=sizeof(A)/sizeof(A[0]);

  G4double Grid[sizeof(B)/sizeof(B[0])];
  double sum=0;
  for(int x=0; x < 81; x++){
    sum=sum+A[x];
    Grid[x]=sum;
    std::ofstream GridFile;
    GridFile.open("Probability_grid.txt", std::ios::app);
    GridFile << Grid[x] << G4endl;
    GridFile.close();
  }
  G4double radius=100*cm; //radius of sphere
  for (int n_particle = 1; n_particle < 100000; n_particle++){
    G4double x0=G4RandGauss::shoot();
    std::ofstream GaussFile;
    GaussFile.open("Gauss_x.txt", std::ios::app); //in mm
    GaussFile << x0 << G4endl;
  }
}

```

```

GaussFile.close();
//Centrally focused semi-spherical source via Gauss distributions
G4double y0=G4RandGauss::shoot();
G4double z0=G4RandGauss::shoot();
G4double n0=sqrt(pow(x0,2)+pow(y0,2)+pow(z0,2));
//Coordinates on sphere
x0 = radius*(x0/n0);
y0 = radius*abs(y0/n0);
z0 = radius*(z0/n0);
std::ofstream SphereFile;
SphereFile.open("coordinates_on_sphere.txt", std::ios::app); //in mm
SphereFile << x0 << " " << y0 << " " << z0 << " " << G4endl;
SphereFile.close();
fParticleGun->SetParticlePosition(G4ThreeVector(x0,y0,z0));
//Aimed at origin
G4double x1=0;
G4double y1=0;
G4double z1=0;
G4double mx = x1-x0;
G4double my = y1-y0;
G4double mz = z1-z0;
G4double mn = sqrt(pow(mx,2)+pow(my,2)+pow(mz,2));
mx = mx/mn;
my = my/mn;
mz = mz/mn;
fParticleGun->SetParticleMomentumDirection(G4ThreeVector(mx,my,mz));
G4double Energy=0; //Just for initialization
G4double pseudo=G4UniformRand();
for (int i=0; i < 81; i++){
if(pseudo > Grid[i] && pseudo <= Grid[i+1]){
Energy=B[i+1];
std::ofstream EnergyFile;
EnergyFile.open("Energy.txt", std::ios::app);
EnergyFile << Energy << G4endl;
EnergyFile.close();
}
}
fParticleGun->SetParticleEnergy(Energy);
fParticleGun->GeneratePrimaryVertex(anEvent);
}
}

```

Appendix E: Generation by means of coordinate transformation

```

#include "B1PrimaryGeneratorAction.hh"
#include "G4LogicalVolumeStore.hh"
#include "G4LogicalVolume.hh"
#include "G4Box.hh"
#include "G4RunManager.hh"
#include "G4ParticleGun.hh"
#include "G4ParticleTable.hh"
#include "G4ParticleDefinition.hh"
#include "G4SystemOfUnits.hh"
#include "Randomize.hh"
#include <iostream>
using namespace std;

B1PrimaryGeneratorAction::B1PrimaryGeneratorAction()
: G4VUserPrimaryGeneratorAction(),
  fParticleGun(0)
// fEnvelopeBox(0)
{
  G4int n_particle = 1;
  fParticleGun = new G4ParticleGun(n_particle);

  // default particle kinematic
  G4ParticleTable* particleTable = G4ParticleTable::GetParticleTable();
  G4String particleName;
  G4ParticleDefinition* particle
    = particleTable->FindParticle(particleName="mu-");
  fParticleGun->SetParticleDefinition(particle);
}

B1PrimaryGeneratorAction::~~B1PrimaryGeneratorAction()
{
  delete fParticleGun;
}

//80-bin Discrete CRY Energy Spectrum
void B1PrimaryGeneratorAction::GeneratePrimaries(G4Event* anEvent)
{
  //Discrete probabilities
  double A[] = {0.0, 0.01253639, 0.02574546, 0.02802035, 0.02706636, 0.03528534,
0.02826496, 0.03157946, 0.03078447, 0.02777574, 0.02546415, 0.03150608,
0.02815489, 0.02580661, 0.02364179, 0.02170935, 0.02152589, 0.02348279,
0.02134243, 0.0196913, 0.02036398, 0.01841931, 0.01718402, 0.01700056,
0.01624226, 0.01539835, 0.01536166, 0.01471344, 0.01422421, 0.01412637,
0.01284215, 0.01260977, 0.01213278, 0.0129033, 0.01248746, 0.01196155,
0.01064064, 0.01057949, 0.0096255, 0.0103838, 0.00928304, 0.00879382,
0.00884274, 0.00793767, 0.00786429, 0.00769306, 0.00709376, 0.00736283,
0.0071916, 0.00721607, 0.00692253, 0.00643331, 0.00678799, 0.00673907,
0.00618869, 0.00634769, 0.00665346, 0.00650669, 0.00561385, 0.00589516,
0.00589516, 0.00578508, 0.00557716, 0.00550378, 0.00434187, 0.0043541,
0.00408503, 0.00364472, 0.00399941, 0.00388934, 0.00396272, 0.00431741,
0.00368142, 0.00363249, 0.00362026, 0.00410949, 0.00336342, 0.00358357,
0.00362026, 0.00348573, 0.0035958};
  //Discrete energies
  double B[] = {0.0, 100, 200, 300, 400, 500, 600, 700, 800, 900, 1000,
1100, 1200, 1300, 1400, 1500, 1600, 1700, 1800, 1900, 2000,
2100, 2200, 2300, 2400, 2500, 2600, 2700, 2800, 2900, 3000,
3100, 3200, 3300, 3400, 3500, 3600, 3700, 3800, 3900, 4000,
4100, 4200, 4300, 4400, 4500, 4600, 4700, 4800, 4900, 5000,
5100, 5200, 5300, 5400, 5500, 5600, 5700, 5800, 5900, 6000,
6100, 6200, 6300, 6400, 6500, 6600, 6700, 6800, 6900, 7000,
7100, 7200, 7300, 7400, 7500, 7600, 7700, 7800, 7900, 8000};
  G4int SizeEnergy=sizeof(B)/sizeof(B[0]);
  G4int SizeProbability=sizeof(A)/sizeof(A[0]);

  G4double Grid[sizeof(B)/sizeof(B[0])];
  double sum=0;
  for(int x=0; x < 81; x++){
    sum=sum+A[x];
    Grid[x]=sum;
    std::ofstream GridFile;
    GridFile.open("Probability_grid.txt", std::ios::app);
    GridFile << Grid[x] << G4endl;
    GridFile.close();
  }
  G4double radius=100*cm; //radius of sphere
  for (int n_particle = 1; n_particle < 100000; n_particle++){
  //Centrally focused semi-spherical source via coordinate transformation
  G4double rand1=G4UniformRand();
  G4double rand2=G4UniformRand();
  G4double theta=acos(2*rand1-1);

```

```

G4double phi=2*3.14159265359*rand2;
//Coordinates on sphere
G4double x0=radius*sin(theta)*cos(phi);
G4double y0=radius*abs(cos(theta));
G4double z0=radius*sin(theta)*sin(phi);
std::ofstream SphereFile;
SphereFile.open("coordinates_on_sphere.dat", std::ios::app); //in mm
SphereFile << x0 << " " << y0 << " " << z0 << G4endl;
SphereFile.close();
fParticleGun->SetParticlePosition(G4ThreeVector(x0,y0,z0));
//Aimed at origin
G4double x1=0;
G4double y1=0;
G4double z1=0;
G4double mx = x1-x0;
G4double my = y1-y0;
G4double mz = z1-z0;
G4double mn = sqrt(pow(mx,2)+pow(my,2)+pow(mz,2));
mx = mx/mn;
my = my/mn;
mz = mz/mn;
fParticleGun->SetParticleMomentumDirection(G4ThreeVector(mx,my,mz));
G4double Energy=0; //Just for initialization
G4double pseudo=G4UniformRand();
for (int i=0; i < 81; i++){
if(pseudo > Grid[i] && pseudo <= Grid[i+1]){
Energy=B[i+1];
std::ofstream EnergyFile;
EnergyFile.open("Energy.txt", std::ios::app);
EnergyFile << Energy << G4endl;
EnergyFile.close();
}
}
fParticleGun->SetParticleEnergy(Energy);
fParticleGun->GeneratePrimaryVertex(anEvent);
}
}

```

References

- [1] S. Agostinelli, et al., GEANT4 - a simulation toolkit, *Nuclear instruments and methods in physics research section A: Accelerators, Spectrometers, Detectors and Associated Equipment* 506 (3) (2003) 250–303.
- [2] GEANT4 Collaboration, *Physics reference manual*, Version: GEANT4 10.7 (2020).
- [3] A. Bogdanov, H. Burkhardt, V. Ivanchenko, S. Kelner, R. Kokoulin, M. Maire, A. Rybin, L. Urban, GEANT4 simulation of production and interaction of muons, *IEEE Transactions on nuclear science* 53 (2) (2006) 513–519.
- [4] L. Bonechi, R. D’Alessandro, A. Giammanco, Atmospheric muons as an imaging tool, *Reviews in Physics* 5 (2020) 100038.
- [5] K. N. Borozdin, G. E. Hogan, C. Morris, W. C. Priedhorsky, A. Saunders, L. J. Schultz, M. E. Teasdale, Radiographic imaging with cosmic-ray muons, *Nature* 422 (6929) (2003) 277–277.
- [6] E. T. Rand, O. Kamaev, A. Valente, A. Bhullar, Nonparametric dense-object detection algorithm for applications of cosmic-ray muon tomography, *Physical Review Applied* 14 (6) (2020) 064032.
- [7] V. Anghel, J. Armitage, F. Baig, K. Boniface, K. Boudjemline, J. Bueno, E. Charles, P. Drouin, A. Erlandson, G. Gallant, et al., A plastic scintillator-based muon tomography system with an integrated muon spectrometer, *Nuclear Instruments and Methods in Physics Research Section A: Accelerators, Spectrometers, Detectors and Associated Equipment* 798 (2015) 12–23.
- [8] P. Checchia, M. Benettoni, G. Bettella, E. Conti, L. Cossutta, M. Furlan, F. Gonella, J. Klinger, F. Montecassiano, G. Nebbia, et al., INFN muon tomography demonstrator: past and recent results with an eye to near-future activities, *Philosophical Transactions of the Royal Society A* 377 (2137) (2019) 20180065.
- [9] P. Checchia, Review of possible applications of cosmic muon tomography, *J. Instrum.* 11 (12) (2016) C12072. doi:10.1088/1748-0221/11/12/c12072.
URL <https://doi.org/10.1088/1748-0221/11/12/c12072>
- [10] S. Procureur, Muon imaging: Principles, technologies and applications, *Nucl. Instr. Meth. A* 878 (2018) 169.

- [11] C. H. Lee, et al., Characteristics of plastic scintillators fabricated by a polymerization reaction, *Nucl. Eng. Technol.* 49 (3) (2017) 592.
- [12] C. Thomay, et al., Passive 3D imaging of nuclear waste containers with muon scattering tomography, *J. Instrum.* 11 (03) (2016) P03008.
- [13] L. Frazão, et al., High-resolution imaging of nuclear waste containers with muon scattering tomography, *J. Instrum.* 14 (08) (2019) P08005.
- [14] A. Georgadze, M. Kiisk, M. Mart, E. Avots, G. Anbarjafari, Method and apparatus for detection and/or identification of materials and of articles using charged particles, US Patent App. 16/977,293 (Jan. 7 2021).
- [15] S. Pesente, et al., First results on material identification and imaging with a large-volume muon tomography prototype, *Nucl. Instr. Meth. A* 604 (3) (2009) 738.
- [16] L. J. Schultz, Cosmic ray muon radiography, Ph.D. thesis, Portland State University (2003).
- [17] M. Bandieramonte, et al., Automated object recognition and visualization techniques for muon tomography data analysis, in: 2013 IEEE Int. Symp. Technol. Homel. Secur. (HST), 2013, p. 517.
- [18] B. Yu, et al., Preliminary analysis of imaging performance in cosmic-ray muon radiography, in: 2013 IEEE Nucl. Sci. Symp. Med. Imaging Conf. (NSS/MIC), 2013, p. 1.
- [19] Z. Liu, et al., Muon tracing and image reconstruction algorithms for cosmic ray muon computed tomography, *IEEE Trans. Image Process.* 28 (1) (2018) 426.
- [20] G. Yang, et al., Novel muon imaging techniques, *Philos. Trans. R. Soc. A* 377 (2137) (2019) 20180062.
- [21] W. Zeng, et al., Principle study of image reconstruction algorithms in muon tomography, *J. Instrum.* 15 (02) (2020) T02005.
- [22] Z. Liu, et al., Muon-computed tomography using POCA trajectory for imaging spent nuclear fuel in dry storage casks, *Nucl. Sci. Eng.*, (2021).
- [23] Classification of Radioactive Waste, no. GSG-1 in General Safety Guides, INTERNATIONAL ATOMIC ENERGY AGENCY, Vienna, 2009.

- [24] Disposal of Radioactive Waste, no. SSR-5 in Specific Safety Requirements, INTERNATIONAL ATOMIC ENERGY AGENCY, Vienna, 2011.
- [25] M.-S. Yim, Addressing key challenges in nuclear waste management, in: Nuclear Waste Management, Springer, 2022, pp. 217–256.
- [26] Strategy and Methodology for Radioactive Waste Characterization, no. 1537 in TECDOC Series, INTERNATIONAL ATOMIC ENERGY AGENCY, Vienna, 2007.
- [27] D. Mahon, A. Clarkson, D. Hamilton, M. Hoek, D. Ireland, J. Johnstone, R. Kaiser, T. Keri, S. Lumsden, B. McKinnon, et al., A prototype scintillating-fibre tracker for the cosmic-ray muon tomography of legacy nuclear waste containers, Nuclear Instruments and Methods in Physics Research Section A: Accelerators, Spectrometers, Detectors and Associated Equipment 732 (2013) 408–411.
- [28] A. Clarkson, D. J. Hamilton, M. Hoek, D. G. Ireland, J. Johnstone, R. Kaiser, T. Keri, S. Lumsden, D. F. Mahon, B. McKinnon, et al., GEANT4 simulation of a scintillating-fibre tracker for the cosmic-ray muon tomography of legacy nuclear waste containers, Nuclear Instruments and Methods in Physics Research Section A: Accelerators, Spectrometers, Detectors and Associated Equipment 746 (2014) 64–73.
- [29] A. Clarkson, D. G. Ireland, R. Al Jebali, R. Kaiser, S. Lumsden, D. Mahon, D. Mountford, M. Ryan, C. Shearer, G. Yang, Characterising encapsulated nuclear waste using cosmic-ray Muon Tomography (MT), in: 2015 4th international conference on Advancements in Nuclear Instrumentation Measurement Methods and their Applications (ANIMMA), IEEE, 2015, pp. 1–7.
- [30] A. I. Topuz, M. Kiisk, A. Giammanco, On discrimination of nuclear waste barrels subject to in-drum mixing by muon scattering tomography: A characterization study based on GEANT4 simulations, in: American Chemical Society Spring 2022, ACS, 2022. doi: 10.1021/scimeetings.2c00098.
- [31] C. Hagmann, D. Lange, D. Wright, Cosmic-ray shower generator (CRY) for Monte Carlo transport codes, in: 2007 IEEE Nuclear Science Symposium Conference Record, Vol. 2, IEEE, pp. 1143–1146.
- [32] D. Heck, J. Knapp, J. Capdevielle, G. Schatz, T. Thouw, et al., CORSIKA: A Monte Carlo code to simulate extensive air showers, Report fzka 6019 (11) (1998).

- [33] P. Biallass, T. Hebbeker, Parametrization of the cosmic muon flux for the generator CMSCGEN, arXiv preprint arXiv:0907.5514 (2009).
- [34] D. E. Cullen, Application of the Probability Table Method to Multi-group Calculations of Neutron Transport, *Nuclear Science and Engineering* 55 (4) (1974) 387–400.
- [35] M. Nakagawa, T. Mori, MORSE-DD, A Monte Carlo code using multi-group double differential form cross sections, Tech. Rep. JAERI-M 84-126, Japan Atomic Energy Research Inst. (1984).
- [36] M. Rivard, A discretized approach to determining TG-43 brachytherapy dosimetry parameters: case study using Monte Carlo calculations for the MED3633 103Pd source, *Applied Radiation and Isotopes* 55 (6) (2001) 775–782.
- [37] E. Boman, J. Tervo, M. Vauhkonen, Modelling the transport of ionizing radiation using the finite element method, *Physics in Medicine & Biology* 50 (2) (2004) 265.
- [38] J. K. Shultis, R. E. Faw, An MCNP primer, Tech. rep., Manhattan, Kansas State University (2011).
- [39] S. Haino, T. Sanuki, K. Abe, K. Anraku, Y. Asaoka, H. Fuke, M. Imori, A. Itasaki, T. Maeno, Y. Makida, et al., Measurements of primary and atmospheric cosmic-ray spectra with the BESS-TeV spectrometer, *Physics Letters B* 594 (1-2) (2004) 35–46.
- [40] T. Goorley, M. James, T. Booth, F. Brown, J. Bull, L. Cox, J. Durkee, J. Elson, M. Fensin, R. Forster, et al., Initial MCNP6 release overview, *Nuclear technology* 180 (3) (2012) 298–315.
- [41] B. O. Yáñez, A. A. Aguilar-Arevalo, A method to measure the integral vertical intensity and angular distribution of atmospheric muons with a stationary plastic scintillator bar detector, *Nuclear Instruments and Methods in Physics Research Section A: Accelerators, Spectrometers, Detectors and Associated Equipment* 987 (2021) 164870.
- [42] R. Forster, T. Godfrey, MCNP - a general Monte Carlo code for neutron and photon transport, in: *Monte Carlo Methods and Applications in Neutronics, Photonics and Statistical Physics*, Springer, 1985, pp. 33–55.
- [43] D. E. Groom, S. Klein, Passage of particles through matter, *The European Physical Journal C-Particles and Fields* 15 (1) (2000) 163–173.

- [44] S. Kelner, R. Kokoulin, A. Petrukhin, Bremsstrahlung from muons scattered by atomic electrons, *Physics of Atomic Nuclei* 60 (4) (1997) 576–583.
- [45] L. Urbán, A model for multiple scattering in GEANT4, Budapest, Hungary (2006).
- [46] H. Lewis, Multiple scattering in an infinite medium, *Physical review* 78 (5) (1950) 526.
- [47] G. Wentzel, Zwei bemerkungen über die zerstreueung korpuskularer strahlen als beugungserscheinung, *Zeitschrift für Physik* 40 (8) (1926) 590–593.
- [48] F. Salvat, J. M. Fernández-Varea, J. Sempau, PENELOPE-2006: A code system for Monte Carlo simulation of electron and photon transport, in: *Workshop proceedings, Vol. 4, Nuclear Energy Agency, 2006*, p. 7.
- [49] L. Van Hove, Correlations in space and time and Born approximation scattering in systems of interacting particles, *Physical Review* 95 (1) (1954) 249.
- [50] H. A. Bethe, Moliere’s theory of multiple scattering, *Physical review* 89 (6) (1953) 1256.
- [51] A. Butkevich, R. Kokoulin, G. Matushko, S. Mikheyev, Comments on multiple scattering of high-energy muons in thick layers, *Nuclear Instruments and Methods in Physics Research Section A: Accelerators, Spectrometers, Detectors and Associated Equipment* 488 (1-2) (2002) 282–294.
- [52] J. Apostolakis, M. Asai, A. Bogdanov, H. Burkhardt, G. Cosmo, S. Elles, G. Folger, V. Grichine, P. Gumplinger, A. Heikkinen, et al., Geometry and physics of the GEANT4 toolkit for high and medium energy applications, *Radiation Physics and Chemistry* 78 (10) (2009) 859–873.
- [53] V. Ivanchenko, O. Kadri, M. Maire, L. Urban, GEANT4 models for simulation of multiple scattering, in: *Journal of Physics: Conference Series, Vol. 219, 2010*, p. 032045.
- [54] A. Bagulya, J. Brown, H. Burkhardt, V. Grichine, S. Guatelli, S. Incerati, V. N. Ivanchenko, O. Kadri, M. Karamitros, M. Maire, et al., Recent progress of GEANT4 electromagnetic physics for LHC and other applications, in: *Journal of Physics: Conference Series, Vol. 898, IOP Publishing, 2017*, p. 042032.

- [55] J. Allison, K. Amako, J. Apostolakis, P. Arce, M. Asai, T. Aso, E. Bagli, A. Bagulya, S. Banerjee, G. Barrand, et al., Recent developments in GEANT4, Nuclear instruments and methods in physics research section A: Accelerators, Spectrometers, Detectors and Associated Equipment 835 (2016) 186–225.
- [56] G. Moliere, Theorie der streuung schneller geladener teilchen ii mehrfach-und vielfachstreuung, Zeitschrift für Naturforschung A 3 (2) (1948) 78–97.
- [57] S. Goudsmit, J. Saunderson, Multiple scattering of electrons, Physical review 57 (1) (1940) 24.
- [58] J. Fernández-Varea, R. Mayol, J. Baró, F. Salvat, On the theory and simulation of multiple elastic scattering of electrons, Nuclear Instruments and Methods in Physics Research Section B: Beam Interactions with Materials and Atoms 73 (4) (1993) 447–473.
- [59] I. Kawrakow, A. F. Bielajew, On the condensed history technique for electron transport, Nuclear Instruments and Methods in Physics Research Section B: Beam Interactions with Materials and Atoms 142 (3) (1998) 253–280.
- [60] V. L. Highland, Some practical remarks on multiple scattering, Nuclear Instruments and Methods 129 (2) (1975) 497–499.
- [61] G. R. Lynch, O. I. Dahl, Approximations to multiple Coulomb scattering, Nuclear Instruments and Methods in Physics Research Section B: Beam Interactions with Materials and Atoms 58 (1) (1991) 6–10.
- [62] Y.-S. Tsai, Pair production and bremsstrahlung of charged leptons, Reviews of Modern Physics 46 (4) (1974) 815.
- [63] S. R. Kelner, R. P. Kokoulin, A. A. Petrukhin, About cross section for high-energy muon bremsstrahlung, Tech. rep. (1995).
- [64] Y. M. Andreev, E. Bugaev, Muon bremsstrahlung on heavy atoms, Physical Review D 55 (3) (1997) 1233.
- [65] R. P. Kokoulin, A. A. Petrukhin, Analysis of the cross-section of direct pair production by fast muons, in: International Cosmic Ray Conference, Vol. 4, 1970, p. 277.
- [66] R. P. Kokoulin, A. A. Petrukhin, Influence of the nuclear form factor on the cross section of electron pair production by high energy muons, in: pp 2436-45 of 12th International Conference on Cosmic Rays. Vol. 6. Hobart, Australia International Union of Pure and Applied Physics (1971)., Inst. of Engineering-Physics, Moscow, 1971.

- [67] S. R. Kelner, Pair production in collisions between muons and atomic electrons, *Physics of Atomic Nuclei* 61 (3) (1998) 448–456.
- [68] Y. Kuno, Y. Okada, Muon decay and physics beyond the standard model, *Reviews of Modern Physics* 73 (1) (2001) 151.
- [69] E. Sudarshan, R. E. Marshak, Origin of the Universal V-A theory, in: *AIP Conference Proceedings*, Vol. 300, American Institute of Physics, 1994, pp. 110–124.
- [70] H. Burkhardt, V. Grichine, P. Gumplinger, V. Ivanchenko, R. Kokoulin, M. Maire, L. Urban, GEANT4 standard electromagnetic package for HEP applications, in: *IEEE Symposium Conference Record Nuclear Science 2004.*, Vol. 3, IEEE, 2004, pp. 1907–1910.
- [71] H. Burkhardt, V. Grichine, V. Ivanchenko, P. Gumplinger, R. Kokoulin, M. Maire, L. Urban, GEANT4 "standard" electromagnetic physics package, in: *Monte Carlo 2005 Topical Meeting*, 2005, pp. 1833–1843.
- [72] G. Anbarjafari, A. Anier, E. Avots, A. Georgadze, A. Hektor, M. Kiisk, M. Kutateladze, T. Lepp, M. Mägi, V. Pastsuk, et al., Atmospheric ray tomography for low-z materials: implementing new methods on a proof-of-concept tomograph, *arXiv preprint arXiv:2102.12542* (2021).
- [73] M. Benettoni, G. Bettella, G. Bonomi, G. Calvagno, P. Calvini, P. Checchia, G. Cortelazzo, L. Cossutta, A. Donzella, M. Furlan, et al., Noise reduction in muon tomography for detecting high density objects, *Journal of Instrumentation* 8 (12) (2013) P12007.
- [74] E. Marton, et al., Muons scanner to detect radioactive sources hidden in scrap metal containers (MU-STEEL), *Final Report* (2014).
- [75] T. Carlisle, J. Cobb, D. Neuffer, Multiple Scattering Measurements in the MICE Experiment, *Tech. rep.*, Fermi National Accelerator Lab. (FNAL), Batavia, IL (United States) (2012).
- [76] J. C. Nugent, Multiple Coulomb scattering in the MICE experiment, *Ph.D. thesis*, University of Glasgow (2017).
- [77] D. Poulson, J. Bacon, M. Durham, E. Guardincerri, C. Morris, H. R. Trelue, Application of muon tomography to fuel cask monitoring, *Philosophical Transactions of the Royal Society A* 377 (2137) (2019) 20180052.

- [78] L. J. Schultz, G. S. Blanpied, K. N. Borozdin, A. M. Fraser, N. W. Hengartner, A. V. Klimenko, C. L. Morris, C. Orum, M. J. Sossong, Statistical reconstruction for cosmic ray muon tomography, *IEEE transactions on Image Processing* 16 (8) (2007) 1985–1993.
- [79] J. Burns, C. Steer, M. Stapleton, S. Quillin, J. Boakes, C. Eldridge, C. Grove, G. Chapman, A. Lohstroh, Portable muon scattering tomography detectors for security imaging applications, in: 2016 IEEE Nuclear Science Symposium, Medical Imaging Conference and Room-Temperature Semiconductor Detector Workshop (NSS/MIC/RTSD), IEEE, 2016, pp. 1–5.
- [80] C. Jewett, V. Anghel, G. Jonkmans, M. Thompson, Simulations of the use of cosmic-rays to image nuclear waste and verify the contents of spent fuel containers-11341, in: WM2011 Conference (Phoenix, AZ), 2011.
- [81] A. I. Topuz, M. Kiisk, A. Giammanco, M. Magi, Unveiling Triangular Correlation of Angular Deviation in Muon Scattering Tomography by Means of GEANT4 Simulations, *Journal for Advanced Instrumentation in Science* 2022 (1) (2022).
- [82] D. E. Groom, N. V. Mokhov, S. I. Striganov, Muon stopping power and range tables 10 MeV–100 TeV, *Atomic Data and Nuclear Data Tables* 78 (2) (2001) 183–356.
- [83] Z. Luo, X. Wang, Z. Zeng, Y. Wang, M. Zeng, J. Cheng, H. Yi, Energy measurement and application on material discrimination in muon tomography, in: 2015 IEEE Nuclear Science Symposium and Medical Imaging Conference (NSS/MIC), IEEE, 2016, pp. 1–4.
- [84] P. Zyla, et al., Review of Particle Physics, *PTEP* 2020 (8) (2020) 083C01. doi:10.1093/ptep/ptaa104.
- [85] A. I. Topuz, M. Kiisk, A. Giammanco, M. Mägi, On muon energy group structure based on deflection angle for application in muon scattering tomography: A Monte Carlo study through GEANT4 simulations, *RAP Conference Proceedings*, 2021, pp. 27–31. doi:10.37392/RapProc.2021.06.
- [86] A. I. Topuz, M. Kiisk, A. Giammanco, M. Mägi, Effect of passive metallic layers on muon energy estimation by means of deflection angle for muon scattering tomography: a comparative study based on GEANT4 simulations, *Journal of Instrumentation* 17 (02) (2022) C02008.

- [87] A. I. Topuz, M. Kiisk, A. Giammanco, Non-destructive interrogation of nuclear waste barrels through muon tomography: A Monte Carlo study based on dual-parameter analysis via GEANT4 simulations, arXiv preprint arXiv:2106.14302 (2021).
- [88] Adam, W and Bergauer, T and Dragicevic, M and Friedl, M and Frühwirth, R and Häsnel, S and Hrubec, J and Krammer, M and Oberegger, M and Pernicka, M and others, Performance studies of the CMS Strip Tracker before installation, *Journal of Instrumentation* 4 (06) (2009) P06009.
- [89] M. Hohlmann, P. Ford, K. Gnanvo, J. Helsby, D. Pena, R. Hoch, D. Mitra, GEANT4 Simulation of a Cosmic Ray Muon Tomography System With Micro-Pattern Gas Detectors for the Detection of High-Z Materials, *IEEE Transactions on Nuclear Science* 56 (3) (2009) 1356–1363.
- [90] D. Pagano, G. Bonomi, A. Donzella, A. Zenoni, G. Zumerle, N. Zurlo, EcoMug: an Efficient COsmic MUon Generator for cosmic-ray muon applications, *Nuclear Instruments and Methods in Physics Research Section A: Accelerators, Spectrometers, Detectors and Associated Equipment* 1014 (2021) 165732.
- [91] A. I. Topuz, M. Kiisk, A. Giammanco, Particle generation through restrictive planes in GEANT4 simulations for potential applications of cosmic ray muon tomography, arXiv preprint arXiv:2201.07068 (2022).
- [92] A. I. Topuz, M. Kiisk, Towards energy discretization for muon scattering tomography in GEANT4 simulations: A discrete probabilistic approach, arXiv preprint arXiv:2201.08804 (2022).
- [93] G. Marsaglia, Choosing a point from the surface of a sphere, *The Annals of Mathematical Statistics* 43 (2) (1972) 645–646.
- [94] Y. Tashiro, On methods for generating uniform random points on the surface of a sphere, *Annals of the Institute of Statistical Mathematics* 29 (1) (1977) 295–300.
- [95] E. W. Weisstein, "Disk point picking." From MathWorld-A Wolfram Web Resource, <http://mathworld.wolfram.com/> (2011).
- [96] Frazão, Leonor and Velthuis, Jaap and Thomay, Christian and Steer, Chris, Discrimination of high-Z materials in concrete-filled containers using muon scattering tomography, *Journal of Instrumentation* 11 (07) (2016) P07020.

Publications

Topuz, Ahmet Ilker; Kiisk, Madis; Giammanco, Andrea (2022). Non-destructive interrogation of nuclear waste barrels through muon tomography: A Monte Carlo study based on dual-parameter analysis via GEANT4 simulations. *Journal of Instrumentation*.

DOI: 10.1088/1748-0221/17/12/P12005.

Topuz, Ahmet Ilker; Kiisk, Madis; Giammanco, Andrea; Magi, Mart (2022). Effect of passive metallic layers on muon energy estimation by means of deflection angle for muon scattering tomography: a comparative study based on GEANT4 simulations. *Journal of Instrumentation*. DOI: 10.1088/1748-0221/17/02/C02008.

Topuz, Ahmet Ilker; Kiisk, Madis; Giammanco, Andrea (2022). DOME: Discrete Oriented Muon Emission in GEANT4 Simulations. *Instruments*. DOI: 10.3390/instruments6030042.

Topuz, Ahmet Ilker; Kiisk, Madis; Giammanco, Andrea; Magi, Mart (2022). Unveiling triangular correlation of angular deviation in muon scattering tomography by means of GEANT4 simulations. *Journal of Advanced Instrumentation in Science*. DOI: 10.31526/jais.2022.

Topuz, Ahmet Ilker; Kiisk, Madis; Giammanco, Andrea (2022). On discrimination of nuclear waste barrels subject to in-drum mixing by muon scattering tomography: A characterization study based on GEANT4 simulations. *American Chemical Society (ACS)*. DOI: 10.1021/scimeetings.2c00098.

Topuz, Ahmet Ilker; Kiisk, Madis; Giammanco, Andrea, Magi, Mart (2021). On muon energy group structure based on deflection angle for application in muon scattering tomography: A Monte Carlo study through GEANT4 simulations. *RAP Conference Proceedings*. *RAP proceedings*, 27-31. DOI: 10.37392/RapProc.2021.06.

Topuz, Ahmet Ilker; Kiisk, Madis; Giammanco, Andrea; Magi, Mart (2022). Investigation of deflection angle for muon energy classification in muon scattering tomography via GEANT4 simulations, *Journal of Physics: Conference Series*, DOI:10.1088/1742-6596/2374/1/012185.

Topuz, Ahmet Ilker; Kiisk, Madis; Giammanco, Andrea (2023). Particle generation through energy discretization and restrictive planes in GEANT4 simulations for potential applications of cosmic ray muon tomography, *Journal of Physics: Conference Series*, DOI:10.1088/1742-6596/2438/1/012150.

Posters

A. I. Topuz, M. Kiisk, A. Giammanco, On discrimination of nuclear waste barrels subject to in-drum mixing by muon scattering tomography: A characterization study based on GEANT4 simulations, ACS Spring 2022, March 21, 2022.

A. I. Topuz, M. Kiisk, A. Giammanco, A Biased Hemispherical Muon Source Based on Gauss Distribution in GEANT4 Simulations, Open Readings 2022, March 18, 2022.

A. I. Topuz, M. Kiisk, Towards energy discretization for muon scattering tomography in GEANT4 simulations: A discrete probabilistic approach, ACAT21, November 29 - December 3, 2021.

A. I. Topuz, M. Kiisk, A. Giammanco, Particle generation through restrictive planes in GEANT4 simulations for potential applications of cosmic ray muon tomography, ACAT21, November 29 - December 3, 2021.

A. I. Topuz, M. Kiisk, A. Giammanco, M. Magi, Unveiling triangular correlation of angular deviation in muon scattering tomography by means of GEANT4 simulations, Muography2021, November 24 – November 26, 2021 .

A. I. Topuz, M. Kiisk, A. Giammanco, M. Magi, Analysis of deflection angle for muon energy categorization in muon scattering tomography by means of GEANT4 simulations, 22nd International Workshop on Imaging Detectors (iWoRiD) 2021, June 27- July 1, 2021.

A. I. Topuz, M. Kiisk, A. Giammanco, M. Magi, Investigation of deflection angle for muon energy classification in muon scattering tomography via GEANT4 simulations, International Conference on Technology and Instrumentation in Particle Physics (TIPP 2021), May 24-29, 2021.

A. I. Topuz, M. Kiisk, A. Giammanco, Non-destructive interrogation of nuclear waste barrels through muon tomography: A Monte Carlo study based on dual-parameter analysis via GEANT4 simulations, SORMA WEST 2021, May 17-28, 2021.

Curriculum vitae

Personal information

Date of birth: 14.07.1982

Place of birth: Istanbul, Turkey

Nationality: Turkish

Civil status: Single

email: aitopuz@protonmail.com

ahmet.ilker.topuz@ut.ee

ORCID number: 0000-0002-1397-8839

Summary

Computational aspects of muon tomography and radiation sources:

- * Radiation Physics: Particle transport and radiation source definition/setup;
- * Computational Methods: Monte Carlo simulations, probabilistic approaches, and statistical/deterministic numerical methods.

Professional

10/2022 - 01/2024 Junior research fellow in physics - University of Tartu

11/2021 - 04/2022 Modelling software engineer - SilentBorder/University of Tartu

02/2016 - 07/2020 Editorial staff - VGSworld

09/2011 - 01/2015 Researcher - M2i

Education

2020 - 2023 University of Tartu

PhD student in Physics

Dissertation: Quantitative and qualitative investigations for muon scattering tomography via GEANT4 simulations: A computational study

2019 Canakkale 18 Mart University

Pedagogical formation in Physics

2010 Istanbul Technical University

Master of Science in Nuclear Energy

Dissertation: Cubic nodal expansion method for the radial solution of the neutron diffusion equation in cylindrical geometry

2006 Isik University
Bachelor of Science in Physics

2001 Lycée Saint-Benoît d'Istanbul
High School

Skills

Language: Turkish, English, French

Computer: Linux, L^AT_EX, FORTRAN, C, Python, QtiPlot, PGF/TikZ, GEANT4

Elulookirjeldus

Isiklik informatsioon

Sünniaeg: 14.07.1982

Sünnikoht: Istanbul, Turkey

Rahvus: Türgi

Tsiviilstaatus: Vallaline

email: aitopuz@protonmail.com

ahmet.ilker.topuz@ut.ee

ORCID number: 0000-0002-1397-8839

Kokkuvõte

Müiontomograafia ja kiirgusallikate arvutuslikud aspektid:

- * Kiirgusfüüsika: osakeste transport ja kiirgusallika määratlus/seadistus;
- * Arvutusmeetodid: Monte Carlo simulatsioonid, tõenäosuslikud lähenemisviisid ja statistilised/deterministlikud numbrilised meetodid.

Professionaalne

10/2022 - 01/2024 Junior research fellow in physics - University of Tartu

11/2021 - 04/2022 Modelling software engineer - SilentBorder/University of Tartu

02/2016 - 07/2020 Editorial staff - VGSworld

09/2011 - 01/2015 Researcher - M2i

Haridust

2020 - 2023 University of Tartu

PhD student in Physics

Dissertation: Quantitative and qualitative investigations for muon scattering tomography via GEANT4 simulations: A computational study

2019 Canakkale 18 Mart University

Pedagogical formation in Physics

2010 Istanbul Technical University

Master of Science in Nuclear Energy

Dissertation: Cubic nodal expansion method for the radial solution of the neutron diffusion equation in cylindrical geometry

2006 Isik University
Bachelor of Science in Physics

2001 Lycée Saint-Benoît d'Istanbul
High School

Oskusi

Keel: Türgi, Inglise, Prantsuse

Arvuti: Linux, L^AT_EX, FORTRAN, C, Python, QtiPlot, PGF/TikZ, GEANT4

DISSERTATIONES PHYSICAE UNIVERSITATIS TARTUENSIS

1. **Andrus Ausmees.** XUV-induced electron emission and electron-phonon interaction in alkali halides. Tartu, 1991.
2. **Heiki Sõnajalg.** Shaping and recalling of light pulses by optical elements based on spectral hole burning. Tartu, 1991.
3. **Sergei Savihhin.** Ultrafast dynamics of F-centers and bound excitons from picosecond spectroscopy data. Tartu, 1991.
4. **Ergo Nõmmiste.** Leelishalogeniidide röntgenelektronemissioon kiirita-misel footonitega energiaga 70–140 eV. Tartu, 1991.
5. **Margus Rätsep.** Spectral gratings and their relaxation in some low-temperature impurity-doped glasses and crystals. Tartu, 1991.
6. **Tõnu Pullerits.** Primary energy transfer in photosynthesis. Model calculations. Tartu, 1991.
7. **Olev Saks.** Attoampri diapsoonis volude mõõtmise füüsikalised alused. Tartu, 1991.
8. **Andres Virro.** AlGaAsSb/GaSb heterostructure injection lasers. Tartu, 1991.
9. **Hans Korge.** Investigation of negative point discharge in pure nitrogen at atmospheric pressure. Tartu, 1992.
10. **Jüri Maksimov.** Nonlinear generation of laser VUV radiation for high-resolution spectroscopy. Tartu, 1992.
11. **Mark Aizengendler.** Photostimulated transformation of aggregate defects and spectral hole burning in a neutron-irradiated sapphire. Tartu, 1992.
12. **Hele Siimon.** Atomic layer molecular beam epitaxy of A^2B^6 compounds described on the basis of kinetic equations model. Tartu, 1992.
13. **Tõnu Reinot.** The kinetics of polariton luminescence, energy transfer and relaxation in anthracene. Tartu, 1992.
14. **Toomas Rõõm.** Paramagnetic H^{2-} and F^+ centers in CaO crystals: spectra, relaxation and recombination luminescence. Tallinn, 1993.
15. **Erko Jalviste.** Laser spectroscopy of some jet-cooled organic molecules. Tartu, 1993.
16. **Alvo Aabloo.** Studies of crystalline celluloses using potential energy calculations. Tartu, 1994.
17. **Peeter Paris.** Initiation of corona pulses. Tartu, 1994.
18. **Павел Рубин.** Локальные дефектные состояния в CuO_2 плоскостях высокотемпературных сверхпроводников. Тарту, 1994.
19. **Olavi Ollikainen.** Applications of persistent spectral hole burning in ultra-fast optical neural networks, time-resolved spectroscopy and holographic interferometry. Tartu, 1996.
20. **Ülo Mets.** Methodological aspects of fluorescence correlation spectroscopy. Tartu, 1996.
21. **Mikhail Danilkin.** Interaction of intrinsic and impurity defects in CaS:Eu luminophors. Tartu, 1997.

22. **Ирина Кудрявцева.** Создание и стабилизация дефектов в кристаллах KBr, KCl, RbCl при облучении ВУФ-радиацией. Тарту, 1997.
23. **Andres Osvet.** Photochromic properties of radiation-induced defects in diamond. Tartu, 1998.
24. **Jüri Örd.** Classical and quantum aspects of geodesic multiplication. Tartu, 1998.
25. **Priit Sarv.** High resolution solid-state NMR studies of zeolites. Tartu, 1998.
26. **Сергей Долгов.** Электронные возбуждения и дефектообразование в некоторых оксидах металлов. Тарту, 1998.
27. **Кауро Кукли.** Atomic layer deposition of artificially structured dielectric materials. Tartu, 1999.
28. **Ivo Heinmaa.** Nuclear resonance studies of local structure in $\text{RBA}_2\text{Cu}_3\text{O}_{6+x}$ compounds. Tartu, 1999.
29. **Aleksander Shelkan.** Hole states in CuO_2 planes of high temperature superconducting materials. Tartu, 1999.
30. **Dmitri Nevedrov.** Nonlinear effects in quantum lattices. Tartu, 1999.
31. **Rein Ruus.** Collapse of 3d (4f) orbitals in 2p (3d) excited configurations and its effect on the x-ray and electron spectra. Tartu, 1999.
32. **Valter Zazubovich.** Local relaxation in incommensurate and glassy solids studied by Spectral Hole Burning. Tartu, 1999.
33. **Indrek Reimand.** Picosecond dynamics of optical excitations in GaAs and other excitonic systems. Tartu, 2000.
34. **Vladimir Babin.** Spectroscopy of exciton states in some halide macro- and nanocrystals. Tartu, 2001.
35. **Toomas Plank.** Positive corona at combined DC and AC voltage. Tartu, 2001.
36. **Kristjan Leiger.** Pressure-induced effects in inhomogeneous spectra of doped solids. Tartu, 2002.
37. **Helle Kaasik.** Nonperturbative theory of multiphonon vibrational relaxation and nonradiative transitions. Tartu, 2002.
38. **Tõnu Laas.** Propagation of waves in curved spacetimes. Tartu, 2002.
39. **Rünno Lõhmus.** Application of novel hybrid methods in SPM studies of nanostructural materials. Tartu, 2002.
40. **Kaido Reivelt.** Optical implementation of propagation-invariant pulsed free-space wave fields. Tartu, 2003.
41. **Heiki Kasemägi.** The effect of nanoparticle additives on lithium-ion mobility in a polymer electrolyte. Tartu, 2003.
42. **Villu Repän.** Low current mode of negative corona. Tartu, 2004.
43. **Алексей Котлов.** Оксидионные диэлектрические кристаллы: зонная структура и электронные возбуждения. Tartu, 2004.
44. **Jaak Talts.** Continuous non-invasive blood pressure measurement: comparative and methodological studies of the differential servo-oscillometric method. Tartu, 2004.
45. **Margus Saal.** Studies of pre-big bang and braneworld cosmology. Tartu, 2004.

46. **Eduard Gerškevičš.** Dose to bone marrow and leukaemia risk in external beam radiotherapy of prostate cancer. Tartu, 2005.
47. **Sergey Shchemelyov.** Sum-frequency generation and multiphoton ionization in xenon under excitation by conical laser beams. Tartu, 2006.
48. **Valter Kiisk.** Optical investigation of metal-oxide thin films. Tartu, 2006.
49. **Jaan Aarik.** Atomic layer deposition of titanium, zirconium and hafnium dioxides: growth mechanisms and properties of thin films. Tartu, 2007.
50. **Astrid Rekker.** Colored-noise-controlled anomalous transport and phase transitions in complex systems. Tartu, 2007.
51. **Andres Punning.** Electromechanical characterization of ionic polymer-metal composite sensing actuators. Tartu, 2007.
52. **Indrek Jõgi.** Conduction mechanisms in thin atomic layer deposited films containing TiO₂. Tartu, 2007.
53. **Aleksei Krasnikov.** Luminescence and defects creation processes in lead tungstate crystals. Tartu, 2007.
54. **Küllike Rägo.** Superconducting properties of MgB₂ in a scenario with intra- and interband pairing channels. Tartu, 2008.
55. **Els Heinsalu.** Normal and anomalously slow diffusion under external fields. Tartu, 2008.
56. **Kuno Kooser.** Soft x-ray induced radiative and nonradiative core-hole decay processes in thin films and solids. Tartu, 2008.
57. **Vadim Boltrushko.** Theory of vibronic transitions with strong nonlinear vibronic interaction in solids. Tartu, 2008.
58. **Andi Hektor.** Neutrino Physics beyond the Standard Model. Tartu, 2008.
59. **Raavo Josepson.** Photoinduced field-assisted electron emission into gases. Tartu, 2008.
60. **Martti Pärs.** Study of spontaneous and photoinduced processes in molecular solids using high-resolution optical spectroscopy. Tartu, 2008.
61. **Kristjan Kannike.** Implications of neutrino masses. Tartu, 2008.
62. **Vigen Issahhanjan.** Hole and interstitial centres in radiation-resistant MgO single crystals. Tartu, 2008.
63. **Veera Krasnenko.** Computational modeling of fluorescent proteins. Tartu, 2008.
64. **Mait Müntel.** Detection of doubly charged higgs boson in the CMS detector. Tartu, 2008.
65. **Kalle Kepler.** Optimisation of patient doses and image quality in diagnostic radiology. Tartu, 2009.
66. **Jüri Raud.** Study of negative glow and positive column regions of capillary HF discharge. Tartu, 2009.
67. **Sven Lange.** Spectroscopic and phase-stabilisation properties of pure and rare-earth ions activated ZrO₂ and HfO₂. Tartu, 2010.
68. **Aarne Kasikov.** Optical characterization of inhomogeneous thin films. Tartu, 2010.
69. **Heli Valtna-Lukner.** Superluminally propagating localized optical pulses. Tartu, 2010.

70. **Artjom Vargunin.** Stochastic and deterministic features of ordering in the systems with a phase transition. Tartu, 2010.
71. **Hannes Liivat.** Probing new physics in e^+e^- annihilations into heavy particles via spin orientation effects. Tartu, 2010.
72. **Tanel Mullari.** On the second order relativistic deviation equation and its applications. Tartu, 2010.
73. **Aleksandr Lissovski.** Pulsed high-pressure discharge in argon: spectroscopic diagnostics, modeling and development. Tartu, 2010.
74. **Aile Tamm.** Atomic layer deposition of high-permittivity insulators from cyclopentadienyl-based precursors. Tartu, 2010.
75. **Janek Uin.** Electrical separation for generating standard aerosols in a wide particle size range. Tartu, 2011.
76. **Svetlana Ganina.** Hajusandmetega ülesanded kui üks võimalus füüsikaõppe efektiivsuse tõstmiseks. Tartu, 2011
77. **Joel Kuusk.** Measurement of top-of-canopy spectral reflectance of forests for developing vegetation radiative transfer models. Tartu, 2011.
78. **Raul Rammula.** Atomic layer deposition of HfO_2 – nucleation, growth and structure development of thin films. Tartu, 2011.
79. **Сергей Наконечный.** Исследование электронно-дырочных и интерстициал-вакансионных процессов в монокристаллах MgO и LiF методами термоактивационной спектроскопии. Тарту, 2011.
80. **Niina Voropajeva.** Elementary excitations near the boundary of a strongly correlated crystal. Tartu, 2011.
81. **Martin Timusk.** Development and characterization of hybrid electro-optical materials. Tartu, 2012, 106 p.
82. **Merle Lust.** Assessment of dose components to Estonian population. Tartu, 2012, 84 p.
83. **Karl Kruusamäe.** Deformation-dependent electrode impedance of ionic electromechanically active polymers. Tartu, 2012, 128 p.
84. **Liis Rebane.** Measurement of the $W \rightarrow \tau\nu$ cross section and a search for a doubly charged Higgs boson decaying to τ -leptons with the CMS detector. Tartu, 2012, 156 p.
85. **Jevgeni Šablonin.** Processes of structural defect creation in pure and doped MgO and NaCl single crystals under condition of low or super high density of electronic excitations. Tartu, 2013, 145 p.
86. **Riho Vendt.** Combined method for establishment and dissemination of the international temperature scale. Tartu, 2013, 108 p.
87. **Peeter Piksarv.** Spatiotemporal characterization of diffractive and non-diffractive light pulses. Tartu, 2013, 156 p.
88. **Anna Šugai.** Creation of structural defects under superhigh-dense irradiation of wide-gap metal oxides. Tartu, 2013, 108 p.
89. **Ivar Kuusik.** Soft X-ray spectroscopy of insulators. Tartu, 2013, 113 p.
90. **Viktor Vabson.** Measurement uncertainty in Estonian Standard Laboratory for Mass. Tartu, 2013, 134 p.

91. **Kaupo Voormansik.** X-band synthetic aperture radar applications for environmental monitoring. Tartu, 2014, 117 p.
92. **Deivid Pugal.** hp-FEM model of IPMC deformation. Tartu, 2014, 143 p.
93. **Siim Pikker.** Modification in the emission and spectral shape of photo-stable fluorophores by nanometallic structures. Tartu, 2014, 98 p.
94. **Mihkel Pajusalu.** Localized Photosynthetic Excitons. Tartu, 2014, 183 p.
95. **Taavi Vaikjärv.** Consideration of non-adiabaticity of the Pseudo-Jahn-Teller effect: contribution of phonons. Tartu, 2014, 129 p.
96. **Martin Vilbaste.** Uncertainty sources and analysis methods in realizing SI units of air humidity in Estonia. Tartu, 2014, 111 p.
97. **Mihkel Rähn.** Experimental nanophotonics: single-photon sources- and nanofiber-related studies. Tartu, 2015, 107 p.
98. **Raul Laasner.** Excited state dynamics under high excitation densities in tungstates. Tartu, 2015, 125 p.
99. **Andris Slavinskis.** EST Cube-1 attitude determination. Tartu, 2015, 104 p.
100. **Karlis Zalite.** Radar Remote Sensing for Monitoring Forest Floods and Agricultural Grasslands. Tartu, 2016, 124 p.
101. **Kaarel Piip.** Development of LIBS for *in-situ* study of ITER relevant materials. Tartu, 2016, 93 p.
102. **Kadri Isakar.** ^{210}Pb in Estonian air: long term study of activity concentrations and origin of radioactive lead. Tartu, 2016, 107 p.
103. **Artur Tamm.** High entropy alloys: study of structural properties and irradiation response. Tartu, 2016, 115 p.
104. **Rasmus Talviste.** Atmospheric-pressure He plasma jet: effect of dielectric tube diameter. Tartu, 2016, 107 p.
105. **Andres Tiko.** Measurement of single top quark properties with the CMS detector. Tartu, 2016, 161 p.
106. **Aire Olesk.** Hemiboreal Forest Mapping with Interferometric Synthetic Aperture Radar. Tartu, 2016, 121 p.
107. **Fred Valk.** Nitrogen emission spectrum as a measure of electric field strength in low-temperature gas discharges. Tartu, 2016, 149 p.
108. **Manoop Chenchiliyan.** Nano-structural Constraints for the Picosecond Excitation Energy Migration and Trapping in Photosynthetic Membranes of Bacteria. Tartu, 2016, 115p.
109. **Lauri Kaldamäe.** Fermion mass and spin polarisation effects in top quark pair production and the decay of the higgs boson. Tartu, 2017, 104 p.
110. **Marek Oja.** Investigation of nano-size α - and transition alumina by means of VUV and cathodoluminescence spectroscopy. Tartu, 2017, 89 p.
111. **Viktoriia Levushkina.** Energy transfer processes in the solid solutions of complex oxides. Tartu, 2017, 101 p.
112. **Mikk Antsov.** Tribomechanical properties of individual 1D nanostructures: experimental measurements supported by finite element method simulations. Tartu, 2017, 101 p.
113. **Hardi Veermäe.** Dark matter with long range vector-mediated interactions. Tartu, 2017, 137 p.

114. **Aris Auzans.** Development of computational model for nuclear energy systems analysis: natural resources optimisation and radiological impact minimization. Tartu, 2018, 138 p.
115. **Aleksandr Gurev.** Coherent fluctuating nephelometry application in laboratory practice. Tartu, 2018, 150 p.
116. **Ardi Loot.** Enhanced spontaneous parametric downconversion in plasmonic and dielectric structures. Tartu, 2018, 164 p.
117. **Andreas Valdmann.** Generation and characterization of accelerating light pulses. Tartu, 2019, 85 p.
118. **Mikk Vahtrus.** Structure-dependent mechanical properties of individual one-dimensional metal-oxide nanostructures. Tartu, 2019, 110 p.
119. **Ott Vilson.** Transformation properties and invariants in scalar-tensor theories of gravity. Tartu, 2019, 183 p.
120. **Indrek Sünter.** Design and characterisation of subsystems and software for ESTCube-1 nanosatellite. Tartu, 2019, 195 p.
121. **Marko Eltermann.** Analysis of samarium doped TiO₂ optical and multi-response oxygen sensing capabilities. Tartu, 2019, 113 p.
122. **Kalev Erme.** The effect of catalysts in plasma oxidation of nitrogen oxides. Tartu, 2019, 114 p.
123. **Sergey Koshkarev.** A phenomenological feasibility study of the possible impact of the intrinsic heavy quark (charm) mechanism on the production of doubly heavy mesons and baryons. Tartu, 2020, 134 p.
124. **Kristi Uudeberg.** Optical Water Type Guided Approach to Estimate Water Quality in Inland and Coastal Waters. Tartu, 2020, 222 p.
125. **Daniel Blixt.** Hamiltonian analysis of covariant teleparallel theories of gravity. Tartu, 2021, 142 p.
126. **Ulbossyn Ualikhanova.** Gravity theories based on torsion: theoretical and observational constraints. Tartu, 2021, 154 p.
127. **Iaroslav Iakubivskiy.** Nanospacecraft for Technology Demonstration and Science Missions. Tartu, 2021, 177 p.
128. **Heido Trofimov.** Polluted clouds at air pollution hot spots help to better understand anthropogenic impacts on Earth's climate. Tartu, 2022, 96 p.
129. **Ott Rebane.** *In situ* non-contact sensing of microbiological contamination by fluorescence spectroscopy. Tartu, 2022, 157 p.
130. **Juhan Saaring.** Ultrafast Relaxation Processes in Ternary Hexafluorides Studied under Synchrotron Radiation Excitation. Tartu, 2022, 106 p.